UNIVERSITÀ
DEGLI STUDI
DI PADOVA

Università degli studi di Padova

Dipartimento di Fisica e Astronomia "'Galileo Galilei"

Corso di Dottorato in Astronomia

Ciclo XXXIV

The Ingot Wavefront Sensor: Dealing with extended sources in Astronomy

Dottorando:
Simone Di Filippo

Coordinatore: Prof. Giovanni Carraro
Supervisore: Prof. Roberto Ragazzoni
Co-Supervisore: Dr. Davide Greggio

to my grandparents
and to you, Giulia

Abstract

Adaptive Optics aims to improve the performance of an optical system such as a telescope, providing at least in principle diffraction-limited imaging. This result is obtained, measuring the wavefront aberration imposed by the earth atmosphere using of suitably bright reference star and compensating for these aberrations through a deformable mirror. In a classical adaptive optic, such reference must be located close to the scientific target, within the so-called Isoplanatic Angle. This requirement reduces dramatically the fraction of the sky that can be efficiently corrected with this technique. A possible solution to this problem is to create an artificial reference in the sky, the so-called Sodium Laser Guide Star (LGS). Unlikely, The Sodium LGS is not a point-like source in the sky, as is valid for the natural guide stars, but more an elongated object in a 3D volume, when launched from the side of a large (or extremely large) telescope. The Sodium LGS nature gave birth to the idea of a new pupil plane wavefront sensor that can be deployed in a similar 3D manner, that can cope with the natural elongation of the LGS. This new device is called Ingot Wavefront Sensor.

In this work, we propose a full description of the Ingot Wavefront Sensor, which has been designed taking into account the characteristics of the European-Extremely Large Telescope (ELT). We performed the optical design, and, both simulations and laboratory tests to investigate which are the performances of the Ingot Wavefront Sensor.

Riassunto

L'ottica Adattiva ha l'obiettivo di migliorare le prestazioni di un sistema ottico quale un telescopio, cercando di raggiungere, almeno in principio, il limite di diffrazione dello strumento. Questo risultato viene si ottiene misurando le aberrazioni che un fronte d'onda che proviene da un oggetto astronomico subisce quando attraversa gli strati turbolenti dell'atmosfera. Un sistema di ottica adattiva per funzionare ha bisogno di un oggetto di riferimento in cielo, da utilizzare per acquisire quali siano le condizioni turbolente in atmosfera, e compensando poi con una correzione complementare al fronde d'onda aberrato tramite uno specchio deformabile. In un sistema di Ottica Adattiva classico, la stella guida deve trovare all'interno di un certo angolo solido, noto come "Angolo Isoplanatico", insieme all'oggetto scientifico che si vuole osservare. Questa richiesta, come e' facile immaginare limita notevolmente la porzione di cielo che si possa osservare. Per ovviare a questo inconveniente e' possibile usare come riferimento in cielo, quelle che sono te come Stelle Guida Laser (LGS). Questo strumento, rende possibile attraverso un lanciatore laser di riprodurre in cielo, all'interno dell'angolo isoplanatico una stella di riferimento. Sfortunatamente gli LGS, non riescono a riprodurre le medesime caratteristiche di una stella naturale. Gli LGS non sono approssimabili ad un oggetto puntiforme, quale una stella naturale, ma sono anzi estesi in uno spazio tridimensionale. I classici sensori di fronte d'onda, quale ad esempio lo Shack-Hartmann possono avere delle difficolta' a sensare un oggetto esteso, perdendo quindi informazioni preziose per la ricostruzione. In questo contesto nasce l'idea di un nuovo sensore di fronte d'onda di piano di pupilla, che chiamiamo INGOT, e che almeno in prima approssimazione e' in grado di usare tutta la geometria della LGS senza perdite di segnale e informazioni. In questo lavoro, riportiamo una descrizione completa del sensore di fronte d'onda INGOT, che e' stato progettato tenendo in riferimento le caratteristiche dello ELT. Abbiamo sviluppato il disegno ottico del sensore, in due varianti, e testato l'INGOT presso un banco ottico gia' esistente in grado di riprodurro in sistema di ottica adattiva quasi reale, ed in aggiunta progettato un banco di prova presso l'Osservatorio Astronomico dove poter testare in autonomia le prestazioni di questo nuovo sensore di fronte d'onda.

Introduction

Adaptive Optics aims to improve the performance of optical systems, such as telescopes, providing at least in principle diffraction-limited imaging. This result is obtained by measuring the wavefront aberration imposed by the Earth's atmosphere using a suitably bright reference star and compensating for these aberrations through a deformable mirror. In a classical adaptive optic, this reference must be located close to the scientific target, within the so-called Isoplanatic Angle. This requirement reduces dramatically the fraction of the sky that can be efficiently corrected employing this technique. A possible solution to this problem is to create an artificial reference in the sky, the so-called Sodium Laser Guide Star (LGS). This facility gives to the telescope the capability to enlarge the sky coverage, creating an artificial reference star, to compensate for the absence of a sufficiently bright star for wavefront sensing. However, LGSs are not point-like sources, but rather elongated objects in three-dimensional space. This is due to the intrinsic nature of the sodium layer, which is located at about 90 km altitude in the atmosphere and extended for approximately 20 km. This layer not only has a specific thickness, but also a particular vertical density distribution, both varying spatially and temporally. The Ingot Wavefront Sensor (I-WFS), has been designed to cope with this typical elongation of the LGS and is presented as a novel pupil-plane wavefront sensor in the framework of the Extremely Large Telescope (ELT) project. The LGS produces significant elongation on many of the Shack-Hartmann wavefront sensor (SH-WFS) spots, especially for large telescopes. The effect is even more significant for the ELT instruments that use SH-WFSs for the wavefront sensing and benefit from LGSs fired from launching telescopes placed at the side of the primary mirror. In my PhD thesis I will focus on the optical design, assembly, integration and verification of the I-WFS. The first chapter describes the atmospheric turbulence characteristics and the Adaptive Optics components. The second chapter is mainly dedicated to define what is a Laser Guide Star facility, analyzing in detail which are their benefits and their disadvantages. Afterwards in chapter 3, a series of scientific cases obtained using the adaptive optics and in particular the LGS facilites are reported. Chapter 4 presents the optical design of the I-WFS, detailing the two different configurations that were tested and emphasizing how the I-WFS characterized the LGSs in each layout. The last two chapters present and discuss the obtained results. Chapter 5 focuses on two tests that were performed on the LOOPS bench (hosted at the Observatory of Marseille) in a quasi-real adaptive loop scenario, while chapter 6 shows the development of a test bench dedicated to the I-WFS and assembled at the INAF laboratory of Padova. In this framework, we developed the optical design, performed several simulations and built a fully automatized alignment procedure. At the end of the chapter, we also present a sensitivity analysis of the I-WFS when known aberrations are applied. Conclusions close the last chapter of this thesis, in which we summarize the results obtained, looking towards future improvements and projects.

Contents

Chapter 1

Adaptive Optics

1.1 Diffraction Limit and Airy Disk

The resolution of an optical system can be limited by many factors, such as imperfections in lenses or misalignment. In any case, there is a limit to the resolution which is due to diffraction, that is called *Diffraction Limit*. An optical system limited only by diffraction is known as *diffraction limited*. For telescopes with circular apertures, the *diffraction limited* image of a point source is the size of the **Airy Pattern**.

In optics, the Airy pattern describes the best focused spots of the light that a lens with a circular aperture can make (limited only by diffraction). As we know, when a beam of light is partially blocked by an obstacle, some light is scattered around that object, and we can see light and dark bands following the edge of the shadow. This effect is called *diffraction*. In order to solve our specific case, it is useful to consider the *Fraunhofer diffraction equation* Eq. (1.1), which is a simplified version of the *Kirchhoff's diffraction formula*, and it can be used to describe the light diffracted when both source and viewing plane are at infinity with respect to diffracting aperture [1].

$$U(p,q) = \int\int_{aperture} G(\alpha,\beta)\, e^{-\frac{2\pi}{\lambda}(p\alpha+q\beta)} d\alpha d\beta, \tag{1.1}$$

where integration is extended over the plane (α, β) of the aperture, and $G(\alpha, \beta)$ define the pupil function, λ is the wavelength, and p & q are the viewing plane coordinates. Eq.1.1, is essentially the Fourier transform of an aperture.

Considering diffraction produced by a single slit of thickness (D), we know that:

$$sin\theta = m\frac{\lambda}{D} \tag{1.2}$$

where λ is the wavelength, and m is the order of diffraction. Figure 1.12 shows Fraunhofer's law result for the slit.

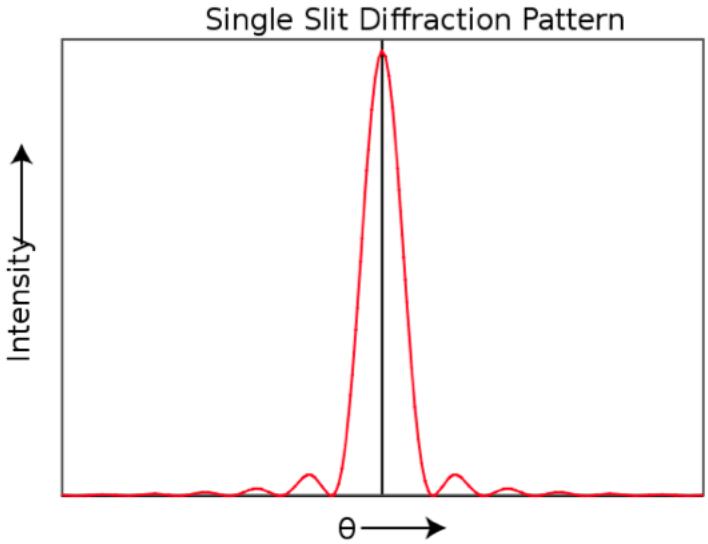

Figure 1.1: *Airy Pattern*

For a circular aperture, the intensity of the so-called *Airy Pattern*, is given by the squared modulus of the Fourier transform of the circular aperture:

$$I(\theta) = I_0 \left(\frac{2J_1(kR\sin\theta)}{kR\sin\theta} \right)^2 = I_0 \left(\frac{2J_1(x)}{x} \right)^2 \tag{1.3}$$

where I_0 is the maximum intensity of the pattern of Airy disk center, J_1 is the **Bessel function** of order one, R is aperture radius, $k = 2\pi/\lambda$ is the wavenumber and θ is the angle of observation.

The zeros of the Bessel function $J_1(x)$ are at:

$$x = kR\sin(\theta) \sim 0; 3.8317; 10.1735; 13.3237... \tag{1.4}$$

which means that the first dark ring in diffraction pattern occurs for $kR\sin(\theta) = 3.8317$ then:

$$\sin\theta = \frac{3.83}{kR} = \frac{3.83\lambda}{2\pi R} = 1.22\frac{\lambda}{D} \tag{1.5}$$

This approximately determines the angular resolution of the telescope.

Let us consider an example. So far we only consider an aperture and a screen without taking into account lens or mirrors, as shown in Fig. (1.2).

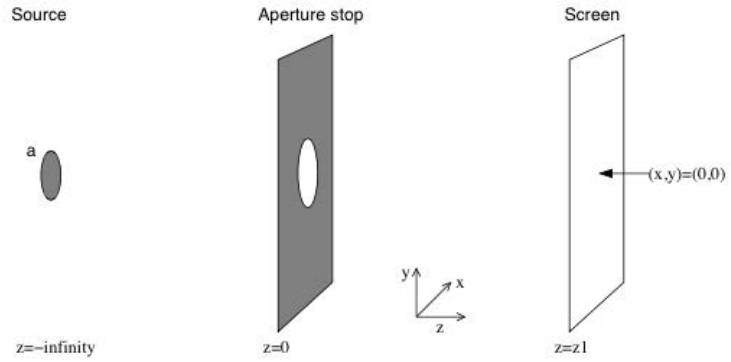

Figure 1.2

For this reason, the radiation on the screen is not really an image of the sky unless we put the screen at a very large distance, (large F-number). Let us introduce now a lens positioned in the *aperture stop*, (Figure 1.3) .

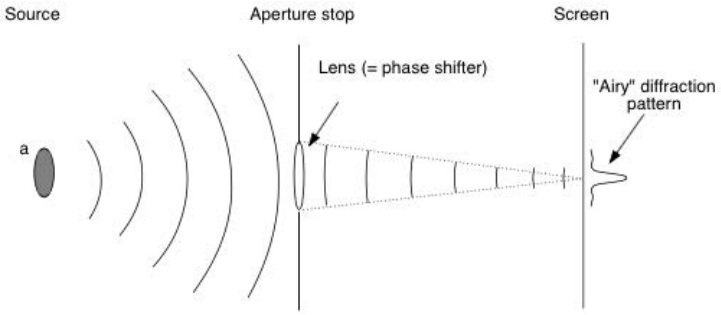

Figure 1.3

If we include a lens in the pupil plane the phases will be shifted such that the wave converges at distance $z = f$ (focal length). We then find that the wave does not converge to a *delta function* but instead to an Airy Pattern. This is exactly the *Point Spread Function* (PSF) of the telescope due only to diffraction. As we can see from Eq.1.5, the larger the aperture, the narrower is the PSF. In general, the PSF degrades the spatial resolution of an image. Let us express the measured intensity on the image plane $I_{obs}(x, y)$ in terms of the real image $I(x, y)$, which should be obtained having an infinite spatial resolution:

$$I_{obs}(x, y) = \int_{-\infty}^{\infty} \int_{-\infty}^{\infty} I(x', y')\, PSF(x - x', y - y')\, dx' dy' \tag{1.6}$$

where PSF in normalised to unity. This equation is the *convolution* of the original image I(x',y') with the PSF.

Hence, we can say that the PSF is exactly the Airy pattern only for an ideal telescope, without any kind of aberration. For real optical systems, the PSF in never an Airy pattern, and this is due to the presence of different kind of aberration (geometrical and chromatic) and of the turbulence. Considering a reflecting telescope, as an example, we do not have just a circular aperture. Instead, we usually have a secondary mirror hanging in the middle of the aperture. Then the PSF, being the

absolute value squared of the Fourier transform of the aperture, will be a distorted Airy pattern. In real life, for telescopes of diameter greater than approximately 10cm, the main contribution to the PSF is usually given by the turbulence in the Earth's atmosphere, producing different effects to light propagation. Turbulence in the Earth's atmosphere is a very complex phenomenon and it is one of the major obstacles for detecting objects during ground-based observations.

1.2 The Earth's Atmosphere

Absorption in the atmosphere imposer limitations on the possibility of observing celestial objects through the whole electromagnetic spectrum, as shown in Figure 1.4.

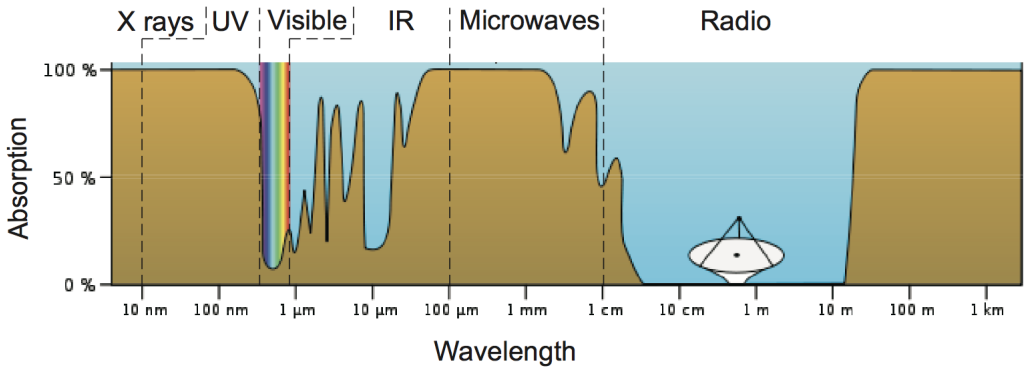

Figure 1.4: *Terrestrial atmosphere transmissivity as a function of wavelength*

It is clear that at short wavelengths $(100 - 300nm)$, the atmosphere is opaque, so the radiation cannot reach the ground. Opacity is caused by the presence of O_2 and N_2 between $(100 - 200)\,nm$, and O_3 between $(200 - 300)\,nm$.
In addition, there are some wavebands called *windows*, in which the Earth's atmosphere is quite transparent; these regions are situated in the Visible and in the Radio domains, and in some Infrared regions, where they are separated by molecular absorption bands.

As said before, the second effect produced by the atmosphere on the electromagnetic radiation coming from on-sky sources is the distortion of the wavefronts. This is caused by turbulence due to random variations of the refractive index n, between sea-level and the first 25 km. The atmosphere is an optically inhomogeneous and dynamic system, since it is constituted by turbulent regions characterized by variable pressure, temperature and density.

From a purely geometrical point of view, we can characterize refraction of a ray passing through a discontinuity surface between two media with different refractive index, n_1 and n_2 by the so called *Snell's law*:

$$n_1 \sin\theta_1 = n_2 \sin\theta_2 \tag{1.7}$$

where n_1 and n_2 are the absolute refractive indices in the media and θ_1 and θ_2, are the angles between the ray propagation direction and the normal to the separating surface. It can be useful to reminder that refractive index in vacuum condition is

$n_v = 1$ at sea level, and the air one is close to $v_{air} = 1.0003$. A more rigorous definition of refractive index, is given by the *Cauchy-Lorentz law*:

$$n \simeq 1 - \frac{77.6 \cdot 10^{-6}}{T}\left(1 + 7.52 \cdot 10^{-3}\lambda^{-2}\right)\left(P + 1810\frac{P_{H_2O}}{T}\right) \tag{1.8}$$

where P $[mbar]$ is the pressure of the air, P_{H_2O} the water vapor pressure, T$[Kelvin]$ the temperature and λ the wavelength. Assuming the vapor pressure as negligible, the previous relation can be approximated to the so called *Gladston's law*:

$$n \simeq 1 - 77.6 \cdot 10^{-6}\frac{P}{T} \tag{1.9}$$

1.2.1 The Kolmogorov's turbulence model

In order to understand how turbulence is generated in the atmosphere, and to quantify its effect on the propagation of light, it is useful to introduce the *Kolmogorov Turbulence Model* [2]. In the following, we will discuss the theory, analyzing each parameter useful for a statistical description of the atmospheric turbulence.

The properties of fluid flows are determined by the *Reynolds number*:

$$Re = \frac{V_0 \cdot L_0}{k_\nu} \tag{1.10}$$

where V_0 is the fluid velocity, L_0 is the characteristic length scale, and k_ν the kinematic viscosity of the fluid. A typical value in air is $k_\nu \simeq 1.5 \cdot 10^{-5}\ m^2 s^{-1}$, so that atmospheric flows with wind speeds of a few ms^{-1} and length scales of several meters to kilometers have a Reynolds Number of $R_e \geq 10^6$. Since the typical value of Re_{cr} is about 2000, the Reynolds parameter of the Earth's atmosphere is always several orders of magnitude above the critical value, corresponding to a clearly turbulent regime

As an example, we can consider the stirring of milk in a cup of coffee: the large motions tend to break up into ever-smaller scale motions and this is exactly what happens in the atmosphere. This down-scaling is known as a *turbulent cascade*, in which fluid becomes turbulent as the Reynolds Number reaches the critical value of $(3 \cdot 10^3)$. Dissipation is not important for the large eddies L_0, but kinetic energy of the turbulent motion is dissipated in small eddies with typical size l_0. These characteristic scales are known as *outer* (L_0) and *inner scale* (l_0) of the turbulence. Typical values for the Earth's atmosphere are $L_0 = 25cm$, while $l_0 = 1cm$. For this $(L_0 - l_0)$ range, called the *Inertial Range* there is a universal description of the turbulence power spectrum, graphically represented in Fig. 1.5.

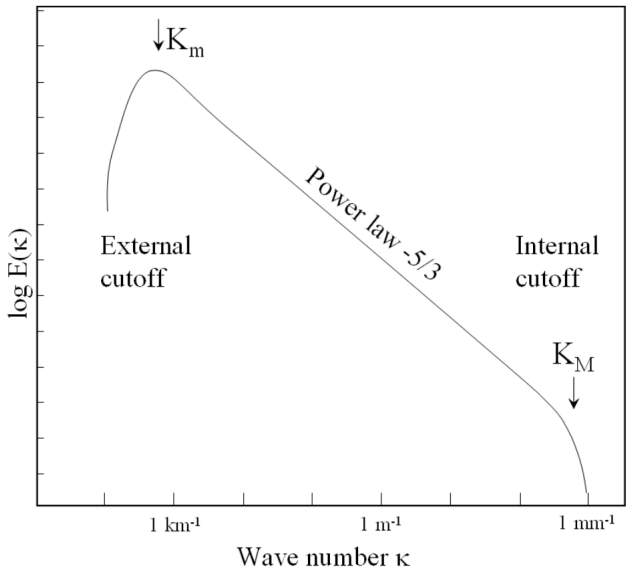

Figure 1.5: *Power spectrum of the energy associated with the vortices in turbulent regime. Where* $K_m = 2\pi/L_0$ *and* $K_M = 2\pi/l_0$.

In addition to L_0 and l_0, there are two other relevant parameters that determine the spectrum of Kolmogorov turbulence, the rate of energy per unit mass $\epsilon \left[m^2 Kg^{-3}\right]$ and the kinematic viscosity $\nu \left[m^2 s^{-1}\right]$. Considering turbulence an homogeneous and isotropic process, the structure function of the turbulent velocity field can be written as:

$$\begin{aligned} D_v\left(R_1, R_2\right) &= \left\langle \left| v\left(R_1\right) - v\left(R_2\right) \right|^2 \right\rangle \\ &= \alpha \cdot f\left(\left|R_1 - R_2\right|/\beta\right) \end{aligned} \tag{1.11}$$

where f is some unspecified dimensionless function of a dimensionless argument.The dimensions of α must be a velocity squared, and those of β a length, since α and β depend only on ϵ and ν it follows:

$$\alpha = \nu^{1/2}\epsilon^{1/2} \quad and \quad \beta = \nu^{3/4}\epsilon^{-1/4} \tag{1.12}$$

As presented before, the structure function must be independent of ν in the *inertial range*, because dissipation plays a role only outside of this range. This is possible only if f has the following form:

$$f = k\left(\left|R_1 - R_2\right|\right)^{2/3} \tag{1.13}$$

with a dimensionless numerical constant k. Combining Eq. 1.13 and Eq. 1.11, the Structure Function becomes:

$$D_v\left(R_1, R_2\right) = \alpha k \cdot \left(\left|R_1 - R_2\right|/\beta\right)^{2/3} = C_v^2 \cdot \left|R_1 - R_2\right|^{2/3} \tag{1.14}$$

where $C_v^2 = \alpha \cdot k/\beta^{2/3} = k \cdot \epsilon^{2/3}$. This result gives a universal description of the turbulence spectrum, depending only on one parameter C_v^2, which describes the turbulence strength.

1.2.2 Wavefront distortion by the atmosphere

Wavefronts are best described by a complex number Ψ, called the *Wave Complex Amplitude*, defined as:

$$\Psi = A \cdot \exp(i\varphi) \tag{1.15}$$

where A is the amplitude and φ the phase of the field fluctuation. The surface where φ assumes the same values is known as *Wave Front Surface*. Light coming from an object at infinite distance can be approximated by a plane wavefront. When this wavefront passes through the atmosphere the speed of the light will vary as the inverse of the refractive index. The result of this process is that the wavefront reaching the ground is no longer flat but corrugated. The phase delay is given by the integration of the refractive index over the light path (z):

$$\delta = \int n(z)dz \tag{1.16}$$

where $n(z)$ is the refractive index. Hence the wave-front phase variation is given by:

$$\varphi = k \cdot \int n(z)dz \tag{1.17}$$

where $k = 2\pi/\lambda$ is the wave-number. Let's consider the difference between the phase $\varphi(\boldsymbol{x})$ at point $\boldsymbol{x}$ on the telescope pupil and the phase $\varphi(\boldsymbol{x} + \boldsymbol{\varsigma})$ at some nearby place, at distance $|\boldsymbol{\varsigma}|$.

The *Variance* is the structure function of the phase, [3]:

$$D_\varphi(\boldsymbol{\varsigma}) = \left\langle |\varphi(\boldsymbol{x}) - \varphi(\boldsymbol{x} + \boldsymbol{\varsigma})|^2 \right\rangle \tag{1.18}$$

Combining Eq. 1.17 and Eq. 1.18 after some mathematical manipulation, it is possible to obtain the phase structure function in terms of the refractive index structure function integrated over the whole atmosphere. Introducing the Zenith angle (γ), Eq.1.18, can be expressed as:

$$D_\varphi(\boldsymbol{\varsigma}) = 2.91k^2 (\cos\gamma)^{-1} \int C_N^2(h)\, dh\, \boldsymbol{\varsigma}^{5/3} \tag{1.19}$$

where the quantity $(\cos\gamma)^{-1}$ is known as *air mass*, and C_N^2 depends on temperature and pressure as:

$$C_N^2 \simeq \left(\frac{80 \cdot 10^{-6} P}{T^2}\right)^2 C_T^2 \tag{1.20}$$

where C_T^2 is the structure function of temperature.
Eq. 1.19 is frequently found in literature in a different form:

$$D_\varphi(\boldsymbol{\varsigma}) = 6.88 \left(\frac{\boldsymbol{\varsigma}}{r_0}\right)^{5/3} \tag{1.21}$$

where:

$$r_0 = \left[0.423k^2 \left(\cos\gamma\right)^{-1} \int C_N^2 \left(h\right) dh\right]^{-3/5} \tag{1.22}$$

is known as **Fried Parameter** [4], to be described in the following section.

1.2.3 Seeing parameters

In order to understand how the atmosphere produces degradation effects on wavefronts, it is useful to define some key parameters:

- The **Fried Parameter**.

  The resolution of Seeing-Limited images obtained through the atmosphere with turbulence characterised by a Fried parameter r_0 is the same as the resolution of diffraction-limited images taken with a telescope of diameter r_0.

  Observations with telescopes much larger than r_0 are seeing-limited, while observations with telescopes much smaller than r_0 are diffraction-limited. It is possible to show that the mean-squared phase variation over the aperture of diameter r_0 is about 1 rad^2 [1]. According to Eq. 1.22, and considering $k = 2\pi/\lambda$, r_0 increases as the 6/5 power of wavelength, and decreases as the -3/5 power of the air mass:

  $$r_0 \propto \left(\lambda^{-2}\right)^{-3/5} = \lambda^{6/5} \tag{1.23}$$

  Hence, it is much easier to achieve diffraction-limited performance when observing at longer wavelengths. Typical value for r_0 at a site with favorable atmospheric conditions at 500 nm are (10 -20) cm, corresponding to PSF sizes laying in the 0.5" to 1" range. At a good site, such as Cerro Paranal (Chile), on a very good night, r_0 is typically of the order of 20 cm at $\lambda = 500$ nm, which corresponds to an image FWHM of 0,6". It must noted that, at any given site r_0 varies dramatically from day to night, and also whit in the same night.

- One more parameter that is fundamental for what concern the distortions due to the atmosphere is the **Isoplanatic Angle** (θ_0).

  Light from different sources (i.e. two different stars) separated by a certain angle θ on the sky passes thought different sections of atmosphere. Therefore, their wavefronts will have different phase variations. In order to proper use Adaptive Optics (AO), it is fundamental that the guide star is close enough to the source observed. The angle within which there is still coherence between the wavefront coming from the guide star and the source is called the isoplanatic angle. This is the field that can be corrected by the Adaptive Optics. A possible way to calculate (θ_0) is to trace back the rays of two stars separated by an angle θ from the telescope pupil. Their separation r(d) at distance d from the observer is $\theta \cdot d$. At the zenith angle z, the distance along the ray is

[1] to be more precise, $\sigma_\phi^2 = 1.03\ rad^2$

linked to the height h of the atmosphere by:

$$d = (h \sec z) \tag{1.24}$$

Putting previous relation in

$$\left\langle \left| \varphi(0) - \varphi(r) \right|^2 \right\rangle = D_\varphi(r) = 2.914\ k^2\ \sec z\ \delta h\ C_N^2\ r^{5/3} \tag{1.25}$$

Integrating over the height h:

$$\begin{aligned} \langle \sigma_\varphi^2 \rangle &= 2.914\ k^2 (\sec z) \int dh\ C_N^2(h) (\theta h \sec z)^{5/3} \\ &= \left(\frac{\theta}{\theta_0} \right)^{5/3} \end{aligned} \tag{1.26}$$

and having introduced the *isoplanatic angle* θ_0, for which the variance of the phase is 1 rad^2:

$$\theta_0 = \left[2.914\ k^2 (\sec z)^{8/3} \int dh\ C_N^2(h) h^{5/3} \right]^{-3/5} \tag{1.27}$$

By comparing Eq. (1.22) and Eq. (1.27), it is possible to write θ_0 as a function of z, r_0 and h as follows:

$$\theta_0 = 0.314 (\cos z) \frac{r_0}{H} \tag{1.28}$$

where H is the *mean effective turbulence height*:

$$H = \left(\frac{\int dh\ C_N^2(h) h^{5/3}}{\int dh\ C_N^2(h)} \right)^{3/5} \tag{1.29}$$

Considering the mean effective turbulence height of 5 km in V band, we obtain a value for the isoplanatic angle θ_0 of the order of 1.3."

- The third parameter which concerns the variations in time is called the **Greenwood Time Delay**. Let us consider Eq. 1.14, which describes the spatial distribution of wavefront distortions. It is useful to consider the equation of temporal changes of the turbulence pattern. A convenient approximation, called the *Taylor Hypothesis*, assumes that time scale for these changes is much longer than the time it takes the wind to blow the turbulence across the telescope aperture. According to this hypothesis, the variations produced by a single layer can be expressed by a *frozen* pattern transported across the aperture by the wind in that layer. Hence, the temporal behavior can be characterized by a time constant:

$$\tau_0 \propto \left(\frac{r_0}{v} \right) \propto \lambda^{6/5} \tag{1.30}$$

where v is the wind speed in the considered layer. The inverse of τ_0 corresponds to the *Greenwood frequency* as $f_G = \tau_0^{-1} = v/r_0$. Typical values for wind speeds and Fried Parameter are 20 m/s and 20 cm, giving $\tau_0 \simeq 10^{-2}\ s$. Note that τ_0 has the same relation with wavelength as r_0, i.e. $\tau_0 \propto \lambda^{6/5}$.

Assuming the Taylor Hypothesis, we can convert the Spatial Structure Function (Eq. 1.21) into a Temporal Structure Function:

$$D_\tau = 6.88 \left(\frac{t}{\tau_0} \right)^{5/3} \tag{1.31}$$

allowing an estimation of the time delay τ_0 as:

$$\tau_0 = (6.88)^{-3/5} \frac{r_0}{v} = 0.31 \frac{r_0}{v} \tag{1.32}$$

The parameter τ_0 defines how fast an Adaptive Optics system should work to properly correct the atmospheric turbulence. For observations with exposure time $t \gg \tau_0$, the aberrations are averaged by the atmospheric random process. On the other hand, short exposures of $t \ll \tau_0$ correspond to *fixed* (frozen) atmospheric aberrations. This delay τ_0 is known as *Greenwood time delay.*

- A fourth parameter that becomes increasingly important for large telescopes, such as the 30/40 m class Extremely Large Telescopes (ELTs), is the outer scale L_0, which is typically a few tens of meters although it can be larger. A wavefront propagated through the atmosphere does not de-correlate any further on spatial scales greater than L_0. Thus, for the ELTs, L_0 may become as important as r_0, θ_0, and τ_0 for deciding which AO science programmes can be observed on a given night. For this reason, it is convenient to consider the Von Karman's power spectrum (1948) which takes this parameter into account, defining a law of the refractive index fluctuations as:

$$\Phi_n \left(\bar{k} \right) = 0.033 C_n^2 \cdot \frac{e^{-\left(k^2 / k_{in}^2 \right)}}{\left(k^2 + k_{out}^2 \right)^{11/6}} \tag{1.33}$$

where $k_{in} = 2\pi / l_0$ and $k_{out} = 2\pi / L_0$ describes the spatial frequencies connected to the inner and outer scales.

1.2.4 Strehl Ratio

The Strehl Ratio (SR) is defined as the ratio between the peak intensity of a measured (PSF) and the peak intensity of a perfect, diffraction-limited PSF. It is used to measure the quality of the wavefront after propagation through turbulence layers, and also as a quality test for AO systems. Its form can be derived considering a circular aperture, with an aberration function $\varphi(\rho, \theta)$, expressed in polar coordinates (ρ, θ). The Strehl Ratio is given by:

$$SR = \frac{1}{\pi^2} \left| \int_0^1 \int_0^{2\pi} d\rho \; d\theta \; \rho \; e^{ik\varphi(\rho,\theta)} \right|^2 \tag{1.34}$$

where $0 \leq SR \leq 1$. Obviously, the highest value is SR = 1, which occurs when the wavefront is flat. If the *root mean square* phase error $\sigma_\phi = k\sigma_\varphi$ is smaller than ≈ 2 rad, the SR can be approximated by the so called *Marechal approximation*:

$$SR = e^{-\sigma_\phi^2} \tag{1.35}$$

$$\sigma_\phi^2 = 1.03 \left(\frac{d_0}{r_0}\right)^{5/3} \tag{1.36}$$

Equations 1.35 and 1.36 demonstrate that the Strehl Ratio is $SR = 0.36$ for images obtained with a uncorrected telescope of diameter $d_0 = r_0$; for $d_0 \geq r_0$ SR decreases with increasing telescope diameter.

1.3 Single-Conjugated Adaptive Optics

The aim of Adaptive Optics is to correct the aberrations introduced by the atmosphere on a wavefront by means of one or more optical correctors inserted into the optical path before the scientific camera. The schematic AO system shown in Fig.1.6, measures the optical path variations using a wavefront sensor (WFS), which measure in real time the optical aberrations to be corrected with a deformable mirror (DM).

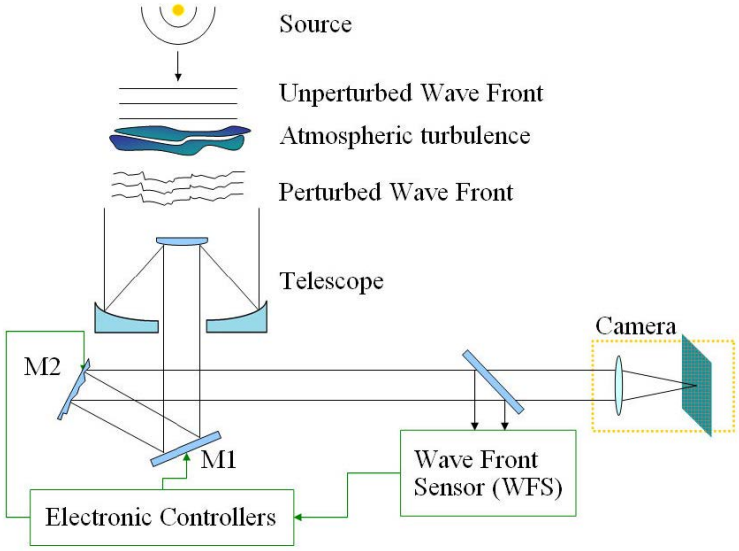

Figure 1.6: *Scheme of a telescope equipped with a classic AO system.*

The simplest AO system configuration is the so called Single-Conjugated Adaptive Optics (SCAO), that is composed of 4 main elements described in the following:

- **Wavefront Sensor**
- **Wavefront Reconstructor**
- **Deformable Mirror**
- **Reference**

1.3.1 Wavefront Sensor

The goal of the Wavefront Sensor (WFS) is to look at a reference point-like source (usually a star) inside the astronomical target isoplanatic patch and reconstruct the distortions the wavefront has been subjected to before reaching the sensor itself. WFSs are usually composed of an optical system sensitive to phase variations, and

a high quantum efficiency detector with low read-out noise. The main types of WFS usually used are:

- Quad Cell Wavefront sensor
- Shack-Hartmann Wavefront sensor
- Curvature Wavefront sensor
- Pyramid Wavefront sensor

1.3.1.1 Quad Cell Wavefront sensor

The Quad Cell sensor is the simplest type of sensor and it is used to evaluate the tip-tilt of the wavefront, splitting the incoming light into four beams. This sensor is placed in the telescope's focal plane and its center is located where the diffraction limited PSF should focus without aberrations. The quad cell sensor can easily measure the spot movements, which are directly proportional to the first derivative of the incoming wavefront shape. The structure of a Quad-cell sensor is shown in the left panel of Fig. 1.7, where the shift of the spot along two directions, can be quantified as:

$$S_x = \frac{(B+D)-(A+C)}{A+B+C+D} \tag{1.37}$$

$$S_y = \frac{(A+B)-(C-D)}{A+B+C+D} \tag{1.38}$$

where A,B,C,D are the intensities (i.e. number of photons per exposure time) detected in each quadrant shown in Fig. 1.7. For small shifts of the spot, S_x and S_y are proportional to the average wavefront first derivative, computed along two orthogonal directions.

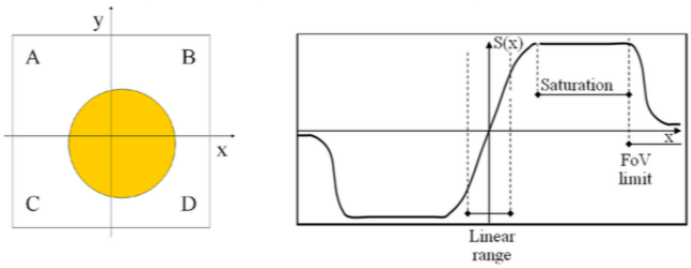

Figure 1.7: *Left panel: Quad Cell WFS. Right panel: S_x signal as a function of the spot shift along x axis.*

The useful operating range to determine tip-tilt is the one where S_x and S_y increase linearly. This happens when the light of the spot hits all the four quadrants of the WFS. Let us consider a situation where all the light coming from the star reaches only the B and D quadrants. This means that the S_x signal would reach its saturation value, so no more shift to the right can produce any variation in the signal itself. It is easy to understand that the linear range is strongly correlated to the spot dimensions: the smaller the spot, the more sensitive the sensor, but the

smaller the linear range, because the S_x and S_y slopes (right panel of Fig. 1.7) are inversely proportional to the spot diameter.

1.3.1.2 Shack-Hartmann Wavefront sensor

The Shack-Hartmann WFS, while to the Quad-Cell WFS, can detect not only low order aberrations, but also the higher orders. Its working principle is based on an approach similar to the *Hartmann test*, in which a mask populated by a certain number of circular sub-apertures is positioned over the telescope aperture. In this context, every hole samples a small area of the whole aperture, and once the pupil is re-imaged by the collimator, many small fixed pupils, each corresponding to one of the holes on the mask will appear. This test presents disadvantages, as a WFS, mostly in case the of measurements of the reference wavefront. First of all, in the case of fainter stars as reference, when the mask is used, the system loses a significant amount of light. This requires the use of only very bright stars, considerably reducing the system sky coverage. It also block the telescope aperture for science photons.

This problem has been solved in the Shack-Hartmann (SH) WFS [**2040-8986-14-9-095704**], in which the mask, is replaced with by a lenslet array positioned in a pupil plane inside the optical path, as shown in Fig. 1.8.

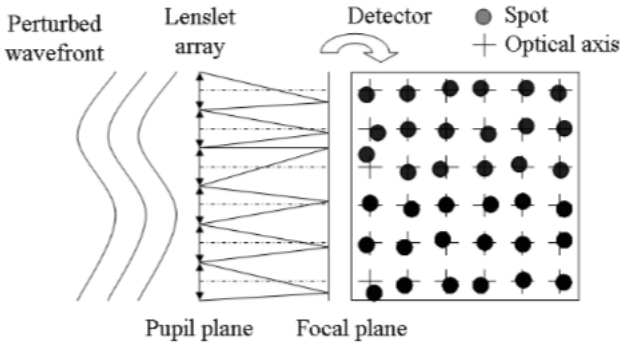

Figure 1.8: *Shack-Hartmann WFS scheme*

In this configuration, where the pupil is not masked, the WFS is illuminated with all the flux collected by the telescope aperture. As many Quad-Cell WFSs as the total number of spots (linked to the lenslets number in the array) are positioned in the focal plane. If the wavefront is totally flat (no deformation present), the barycenter of each spot will be focused on the optical axis of the corresponding lens. Instead, if the wavefront is aberrated, then each spot will move on the focal plane by a quantity proportional to the average wavefront slope over that sub-aperture. The number of sub-apertures, should be high enough to properly sample the wavefront. A reasonable limit is given by the Fried Parameter:

$$N = \frac{D}{r_0} \tag{1.39}$$

where N is the number of lenslets across the pupil diameter, and D is the telescope diameter.

The SH WFS is able to measure the first derivative of the wavefront as follows:

$$\frac{\partial W}{\partial x} \propto \frac{1}{2}\left(\frac{\lambda}{d}\right)\frac{(A+C)-(B+D)}{A+B+C+D} \tag{1.40}$$

$$\frac{\partial W}{\partial y} \propto \frac{1}{2}\left(\frac{\lambda}{d}\right)\frac{(A+C)-(C+D)}{A+B+C+D} \tag{1.41}$$

where d is the lens diameter. According to the error theory, in the absence of other sources of noise, the uncertainty on the measurement of the spot position depends on the number of incoming photons and is dominated by the Poisson noise. Considering M photons reaching the telescope entrance pupil during an exposure time, and the lenslet array (NxN), each sub-aperture collects $\bar{n} = M/N^2$ photons. The number of photons collected by the optical system is inside the range $M \pm \sqrt{M}$, and its propagated error in term of Quad-Cell signals results:

$$S_x = \frac{1}{2}\left(\frac{\lambda}{d}\right)\frac{\left(\frac{M}{2} \pm \frac{\sqrt{M}}{2}\right)-\left(\frac{M}{2} \pm \frac{\sqrt{M}}{2}\right)}{M \pm \sqrt{M}} = \pm\frac{1}{2}\left(\frac{\lambda}{d}\right)\frac{\sqrt{M}}{M \pm \sqrt{M}} \approx \frac{1}{2}\left(\frac{\lambda}{d}\right)\frac{1}{\sqrt{M}} \tag{1.42}$$

In the end, the SH WFS are able to retrieve both the low and high order aberrations of the wavefront, but there are several technical difficulties. The lenslet array is composed of several optical surfaces, that must be produced within quite tight specifications, concerning the surface accuracy of the optical power. In addition, the conjunctions between the lenses should be very small. Otherwise, the wider the gap, the higher the amount of light which is lost and diffused because of diffraction.

1.3.1.3 Curvature WFS

The Curvature WFS, designed by Roddier [3], is quite different to the other WFSs. Its peculiarity is connected to the ability of detecting second derivatives of the wavefront. In its simplest realization, it is composed of two different detectors, one before the focal plane of the telescope and one after. In this configuration, they can detect the light distribution both on the *intrafocal* $I_i(x)$ and extra *extra focal* $I_e(x)$ plane. Considering the geometric approximation, a positive curvature wavefront produces an intra-focal image, while a negative curvature wavefront translates into just the opposite effect. Figure 1.9 shown its design.

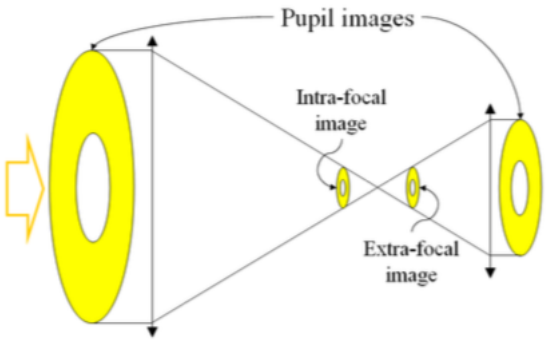

Figure 1.9: *Curvature WFS scheme*

The normalized difference between the intensities of the intra-focal and extra-focal images is proportional to the Laplacian of the wavefront:

$$\frac{I_i(r) - I_e(r)}{I_i(r) + I_e(r)} \propto \nabla^2 W \tag{1.43}$$

where W is the wavefront and ∇^2 the Laplacian, corresponding to the divergence of the gradient of the field to which is applied. Similarly to the SH technique, the use of a lenslet array splitting the pupil into sub-pupils allows a measure meant of the curvature over smaller areas of the wavefront collected by the telescope, permitting in this way the computation the high order aberrations with a spatial sampling which is depending on the number of lenses of the lenslet array.

1.3.1.4 Pyramid Wavefront Sensor

The pyramid wavefront sensor was invented by Ragazzoni [5] and it is composed of a pyramid prism placed in the focal plane of the telescope (see Fig. 1.10). The light coming from the reference star is focused on the vertex of the pyramid. The prism will then split the light into 4 beams, which will produce 4 different images of the telescope pupil. The intensity of each image, is proportional to the number of photons reaching each pyramid face. The distance of the pupil centres depends on the collimator focal length and on the vertex angle of the pyramid, as follows:

$$d_{centers} = \beta (n - 1) f_{ob} \tag{1.44}$$

where β is the pyramid vertex angle, n is the refractive index and f_{ob} is the objective focal length.

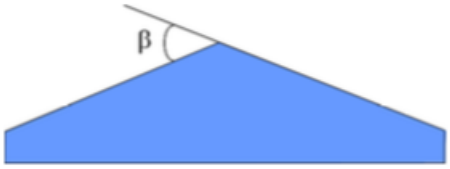

Figure 1.10: *Pyramid vertex angle scheme*

When tip-tilt needs to be calculated, it is possible to refer at the Quad Cell Wavefront Sensor. However, in this situation, the 4 cells are represented by the 4 images of the pupils. According to this approach, the fluxes A, B, C, and D in Equations 1.37 and 1.38 correspond to the integrated fluxes over the whole aperture of the 4 pupil images. On the contrary, for the high order aberrations, the wavefront needs to be divided. However, unlike the Shack-Hartmann sensor, by using the pyramid sensor, it is not necessary to include other optical components. In fact, the sub-apertures can be taken directly from the 4 pupils images on the detector. The measurement of the wavefront inclination on the sub-aperture can be derived in the same way of the Quad Cell sensor. However, in this case, the fluxes have to be measured on the same pupil portion from the 4 images (See right side of Figure 1.11). In order to reconstruct high orders aberrations of the wavefront, this operation needs to be repeated for all the sub-apertures.

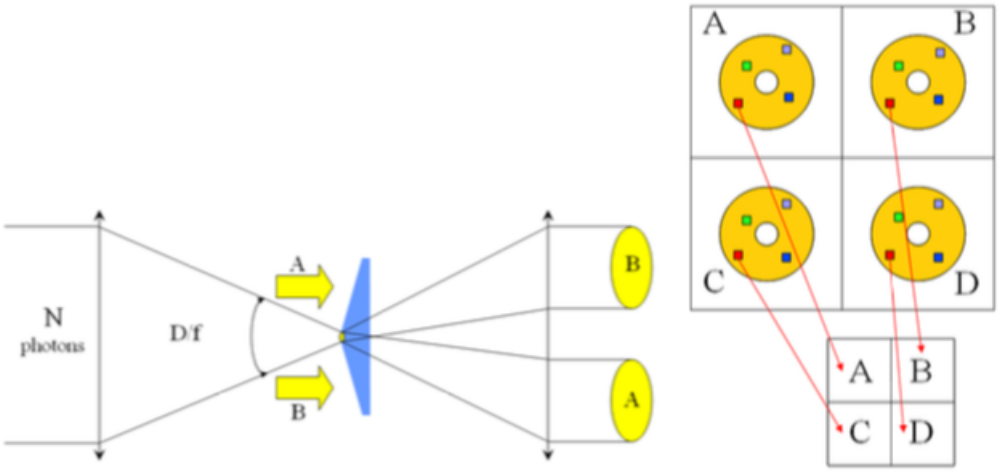

Figure 1.11: *Four pupil re-imaging in the pyramid WFS and tip-tilt computation for the overall aperture*

As opposed to the Shack-Hartmann sensor, the pyramid really allows variations in the spatial sampling by changing the CCD binning. The maximum sampling corresponds to a sub-aperture of 1 pixel. As in the SH-WFS, it is not recommended to use more than D/r_0 pixels over the pupil diameter to avoid oversampling with a waste of light per sub-aperture. Another advantage of using the pyramid sensor is the higher sensitivity when operated in closed loop. In fact, when the AO system starts to correct the wavefront, the spot produced by the reference star on the pyramid vertex gets smaller reaching, in the ideal case, the telescope diffraction limit. Because of the reduced area occupied by the light on the pyramid sensor, the signal-to-noise ratio and the sensitivity increase (similarly to the Quad Cell sensor). Considering a 10 meter telescope, this increase allows to use reference objects with a magnitude up to 1-2 mag higher than the magnitude limit considered for other WFS [6]. However, reducing the light spot area on the pyramid does reduce the linear regime and the pyramid sensor becomes unstable for rapid variations of the turbulence. In this case, the light spot will be focused on only one pyramid face, leading to a saturated signal similar to the Quad Cell Sensor case. To solve this issue, it has been proposed to apply a modulation, meaning that the spot is forced to move around the pyramid vertex with frequency higher than the CCD read frequency [7]. In this way, photons will reach each of the 4 faces of the pyramid producing a situation similar to the case where the spot on the pyramid is bigger. Clearly, low sensitivity corresponds to greater dynamic range, which allow us to correct the higher aberrations avoiding signal saturation. On the other hand, with higher sensitivity, dynamic range will be limited. It is clear that applying strong modulation at the very beginning of the closed loop operations may be convenient because of the high aberrations of the wavefront.

1.3.2 Wavefront reconstruction

Wavefront reconstruction consists in calculating an appropriate correction vector $\boldsymbol{v}$ (containing the voltages to be sent to the Deformable Mirror) from the WFS measurements vector $\boldsymbol{s}$ (containing, as an example, all the slopes obtained by a SH-WFS). Assuming that the system working in closed loop, wavefront reconstruction

is described by the linear system:

$$D \cdot \boldsymbol{v} = \boldsymbol{s} + \boldsymbol{n} \tag{1.45}$$

where $\boldsymbol{n}$ represents the measurements noise and D is the so-called interaction matrix between DM and WFS. In order to solve for $\boldsymbol{v}$, it is easier to consider R, which is the inverse matrix of D, or more precisely is the *Moore-Penrose pseudo inverse*. Unfortunately, this approach leads to a non-optimal propagation of noise. To avoid this it is more convenient to use a modal decomposition [8]:

$$W(x,y) = a_0 Y_0(x,y) + a_1 Y_1(x,y) + ... = \sum_{i=0}^{N} a_i Y_i(x,y) \tag{1.46}$$

where x and y are the spatial coordinates on the pupil, Y_i are the terms and a_i the linear combination coefficients. One of the most common decompositions used in optics is the Zernike decomposition, where the terms are polynomials (Z_n^m), each one describing a single known optical aberration [9].

1.4 Zernike Modal Base

Zernike polynomials have the advantage of being mathematically well defined and the low order terms are related to classical optical aberrations of circularly symmetric systems. Considering a circular aperture without obstructions, it is possible to define the Zernike polynomials, using polar coordinates (ρ, θ), as:

$$Z_n^m(r,\theta) = N_n^m \cdot R_n^m(\rho) \begin{cases} \cos(m\theta) & m \geq 0 \\ \sin(m\theta) & m < 0 \end{cases} \tag{1.47}$$

They form a set of orthogonal polynomials and the modes are defined as:

$$N_n^m = \sqrt{\frac{2(+1)}{1+\delta_m}} \quad and \quad \delta_m = \begin{cases} 1 & m \neq n \\ 0 & m = n \end{cases} \tag{1.48}$$

$$R_n^m = \sum_{s=0}^{(n-m)/2} \frac{(-1)^s (n-s)!}{s!\left[(n+m)/2 - s\right]!\left[(n-m)/2 - s\right]!} \rho^{n-2s} \tag{1.49}$$

The index n is called *radial degree*, while m is the *azimuthal frequency*.

Table ?? shows the first 15 Zernike modes $Z_n^m(\rho, \theta)$, where j is an usual ordering number.

Zernike's modes are orthogonal over a circle with unit radius, expressing Z as function of vector $\boldsymbol{r}(r, \alpha)$:

$$\int W(\boldsymbol{r}) Z_j(\boldsymbol{r}) Z_k(\boldsymbol{r}) d\boldsymbol{r} = \delta_{jk} \tag{1.50}$$

where δ_{jk} is the Kronecker's Delta which is equal to one if $j = k$, and equal to zero

n	m=0	m=1	m=2	m=3	m=4
0	Z_1=1 (piston)				
1		Z_2=$2\rho\cos\theta$ Z_3=$2\rho\sin\theta$ (tilt-tip)			
2	$Z_4 = \sqrt{3}\left(2\rho^2-1\right)$ (defocus)		$Z_5 = \sqrt{6}\rho^2\sin 2\theta$ $Z_6 = \sqrt{6}\rho^2\cos 2\theta$ (astigmatism)		
3		$Z_7 = \sqrt{8}\left(3\rho^3-2\rho\right)\sin\theta$ $Z_8 = \sqrt{8}\left(3\rho^3-2\rho\right)\cos\theta$ (coma)		$Z_9 = \sqrt{8}\rho^3\sin 3\theta$ $Z_{10} = \sqrt{8}\rho^3\cos 3\theta$ (trefoil)	
4	$Z_{11} = \sqrt{5}\left(\rho^4-6\rho^2+1\right)$ (spherical)		$Z_{12} = \sqrt{10}\left(10\rho^4-3\rho^2\right)\cos 2\theta$ $Z_{13} = \sqrt{10}\left(10\rho^4-3\rho^2\right)\sin 2\theta$ (astigmatism)		$Z_{14} = \sqrt{10}\rho^4 t\cos 4\theta$ $Z_{15} = \sqrt{10}\rho^4 t\cos 4\theta$ (ashtray)

Table 1.1: *Zernike polynomials Z_j for j=1 to 15. n radial order and m azimuthal order. The modes are ordered such as j correspond to the symmetric modes given by* $(\cos m\theta)$ *and odd j to antisymmetric modes given by* $(\sin m\theta)$.

if $j \neq k$. The function $W(\boldsymbol{r})$ is defined as:

$$\int W(\boldsymbol{r})d\boldsymbol{r} = \begin{cases} 1/\pi & (r \geq 1) \\ 0 & (r < 1) \end{cases} \tag{1.51}$$

The polynomial expansion of the arbitrary wave-front $\varphi(\boldsymbol{r})$ over a circular aperture of unit radius is:

$$\varphi(\boldsymbol{r}) = \sum_{j=1}^{\infty} a_j Z_j(\boldsymbol{r}) \tag{1.52}$$

where the coefficients a_j are given by

$$a_j = \int_{aperture} W(\boldsymbol{r})\, Z_j(\boldsymbol{r})\, \varphi(\boldsymbol{r})\, dr \tag{1.53}$$

Since the turbulence coefficients a_j are random, is reasonable to apply a statistical approach. Their covariance is given by:

$$\langle a_j a_k \rangle = \left\langle \int W(\boldsymbol{r}) Z_j(\boldsymbol{r}) \varphi(\boldsymbol{r}) d\boldsymbol{r} \int W(\boldsymbol{r'}) Z_j(\boldsymbol{r'}) \varphi(\boldsymbol{r'}) d\boldsymbol{r'} \right\rangle \tag{1.54}$$

and rewritten as a double integral:

$$\langle a_j a_k \rangle = \int\int W(\boldsymbol{r}) Z_j(\boldsymbol{r}) W(\boldsymbol{r'}) Z_k(\boldsymbol{r'}) \left\langle \varphi(\boldsymbol{r})\varphi(\boldsymbol{r'}) \right\rangle dr dr' \tag{1.55}$$

and then applying the substitution $\boldsymbol{r} = (\boldsymbol{r'} + \boldsymbol{\rho})$

$$\langle a_j a_k \rangle = \int \langle \varphi(\boldsymbol{r})\varphi(\boldsymbol{r}+\boldsymbol{\rho}) \rangle \int W(\boldsymbol{r}) Z_j(\boldsymbol{r}) W(\boldsymbol{r}+\boldsymbol{\rho}) Z_k(\boldsymbol{r}+\boldsymbol{\rho}) dr d\rho \tag{1.56}$$

Assuming covariance $\langle \varphi(\boldsymbol{r})\varphi(\boldsymbol{r}+\boldsymbol{\rho}) \rangle$ as a stationary function of ρ, it is possible to consider its *Fourier transform* as power spectrum $\Phi(k)$ of the random wave-front phase $\varphi(\boldsymbol{r})$. The second integral is a convolution between $W(\boldsymbol{r})$ and $Z(\boldsymbol{r})$.

Applying the Fourier transform, this term appears to be the product of the single Fourier transforms of the two convolution factors. If $P_j(\boldsymbol{k})$ is the Fourier transform of $W(\boldsymbol{r})Z_j(\boldsymbol{r})$, Equation 1.56 can be written as:

$$\langle a_j a_k \rangle = \int \Phi(\boldsymbol{k}) P_j(\boldsymbol{k}) P_k(\boldsymbol{k}) dk \tag{1.57}$$

The power spectrum of wave-front phase can be written following Roddier, 1981 [3]:

$$\Phi(\boldsymbol{k}) = 7.2 \cdot 10^{-3} \left(D/r_0\right)^{5/3} |\boldsymbol{k}|^{-11/3} \tag{1.58}$$

obtained from its structure function. $P_j(\boldsymbol{k})$ functions are given by Noll, 1976 [9] having the form:

$$P_n^m\left(f, \alpha\right) = \sqrt{n+1}\ \frac{J_{n+1}\left(2\pi k\right)}{\pi k} \tag{1.59}$$

where f and α are the modulus and argument of $\boldsymbol{k}$, and J_n is a Bessel function of n order. We refer to Noll, 1976 [9] for further details on the analysis of the $P_j(\boldsymbol{k})$ functions. Combining Eq. 1.58 and Eq. 1.57, the covariance can be written as:

$$\langle a_j a_k \rangle = c_{jk} \left(D/r_0\right)^{5/3} \tag{1.60}$$

Coefficients c_{jk} are functions of the radial degrees and their values were published firstly by Wang & Marley [10], and Roddier [11].

The mean square wave-front phase fluctuation can be defined as:

$$\sigma^2 = \left\langle \int W(\boldsymbol{r}) \varphi^2(\boldsymbol{r}) dr \right\rangle \tag{1.61}$$

and taking Eq. 1.50 into account:

$$\sigma^2 = \sum_j \langle a_j^2 \rangle \tag{1.62}$$

By neglecting the piston term ($j = 1$) and taking into account Eq. 1.60, it is possible to define σ^2 as:

$$\sigma^2 = \sum_{j=2}^{\infty} c_{jj} \left(D/r_0\right)^{5/3} \tag{1.63}$$

where r_0 is the Fried parameter. One of the advantages of performing the modal expansion of the phase is now clear: if the degrees of freedom of correction are made to coincide with the orthonormal modes of the phase decomposition of Eq. 1.52, AO is capable to correct the first N modes of the expansion. Then the residual mean square phase over the aperture, can be written as:

$$\sigma_{res}^2 = \sigma^2 - \sum_{j=1}^{N} \langle a_j^2 \rangle \tag{1.64}$$

The previous relation can be also factorized in terms of $\left(D/r_0\right)^{5/3}$, following Eq.

1.63 in the form:

$$\sigma^2 = \sum_{j=2}^{\infty} c_{jj} \left(D/r_0\right)^{5/3} = \Delta_N \left(\frac{D}{r_0}\right)^{5/3} \tag{1.65}$$

By correcting an increasing number of Zernike modes, the seeing disk shape can be modified. This peak appears to be dominant when the corrected modes increase until the seeing halo disappears, due to perfect correction.

For a better comprehension, Figure 1.12 shows the shapes of 21 correction terms of Zernike modes.

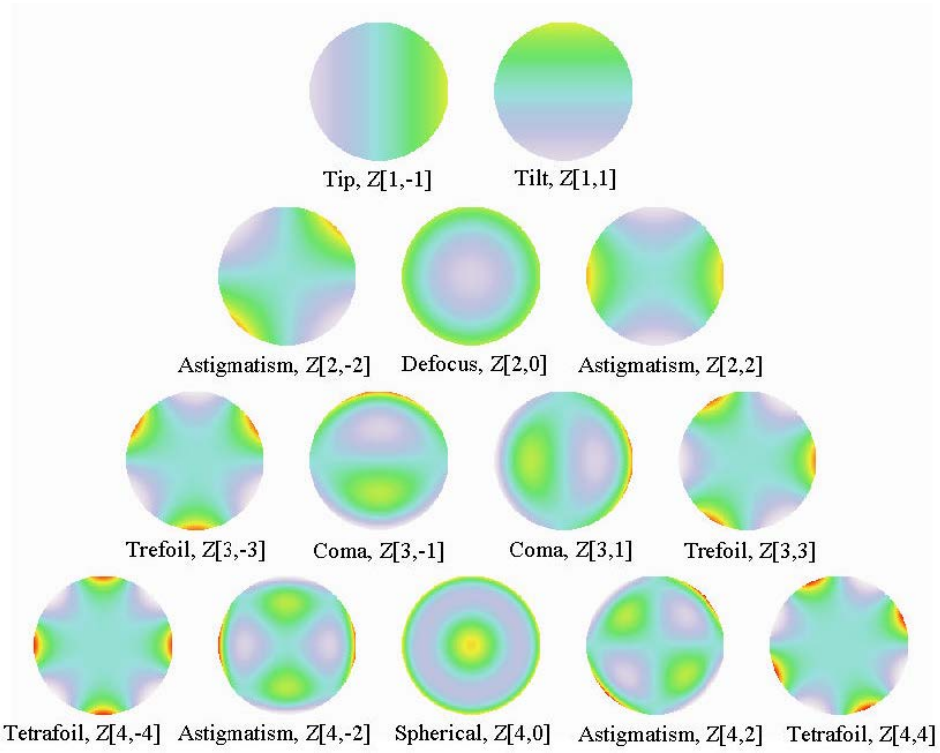

Figure 1.12: *Graphical representation of the main aberrations described by Zernike polynomials*

1.4.1 Karhunen-Loeve expansion

The Zernike's polynomials expansion, impose a upper limit to the number of modes that can be used for the correction, leaving the wavefront errors residuals high due to the un-corrected modes. This error can be minimized using a different base for the correction, like the Karhunen-Loeve polynomials base that allow to minimize the residual according to the number of correct modes. The terms K_k, of this expansion are computed starting from the Zernike polynomials:

$$K_k\left(\frac{\rho}{R'}, \theta\right) = \sum_j u_{jk} Z_j \left(\frac{\rho}{R'}, \theta\right) \tag{1.66}$$

where u_{jk} are the terms fo the transformation matrix, R' is the radius of the pupil.

1.4.2 Deformable Mirrors

The first development of deformable mirrors (DM) arose from a TV projection system in the early 1950's. In order to apply this technique to AO systems, the Eidophor mirror was used to shape the wave-front with local tilts. For the first time in 1953, Babcock suggested to use this kind of mirror in his proposal for adaptive optics system technology which became available and mature a few years later.

The goal of a DM is to correct the optical path differences caused by the atmosphere. The DM mirror usually consists of an array of actuators which are connected to a thin optical surface. This surface can be deformed by pushing and pulling using a certain number of actuators. The most important parameters of a DM are stroke, response time and number of actuators. The response time should comply with the requirements set by τ_0, the stroke is related to the power of the turbulence to be removed and the number of actuators scales with r_0 and the aperture diameter. To be more precise, the minimum number of actuators must be at least equal to:

$$N_0 = 0.27\,(D/r_0)^2 \tag{1.67}$$

since r_0 increases as $\lambda^{6/5}$, the required number of actuators decreases as $\lambda^{-12/5}$. This is one of the reasons why AOs is easier to be performed at longer wavelengths. With the technology available today, the densest DMs have some thousands of actuators. For example, the Extremely Large Telescope (ELT) is expected to have a Deformable Mirror with 80x80 actuators over the diameter. The physically largest DMs are the so called *adaptive/deformable mirrors* (DSM), which are used instead of static secondary mirror of the telescope. They provide AO correction while maintaining high transmission and low thermal emissivity.

Actuators are typically separated by a few craned attached to an optical shell, about 1m in diameter but only 1-2 mm thick. Another advantage of the DSMs is that they are in the main telescope optical train, and thus every instrument installed can benefit from their correction. Due to this feature and to their excellent on-sky performance, they are widely used in several telescopes, such as the Large Binocular Telescope (LBT) and the Very Large Telescope (VLT).

1.4.3 Reference Stars

In order to obtain reasonable correction performance, AO systems need sufficiently bright guide stars, (the magnitude of which depends essentially on the number of subapertures and on the WFS sensitivity), within θ_0 from the astronomical target. These constraints typically translate into very limited sky coverage, also depending on the level of correction required by the different science cases. Sky coverage changes dramatically in different sky areas. It reaches a minimum level, at the Galactic poles of the order of (0.1% in V-band and 0.5% in K-band) and a maximum level at the Galactic plane, of the order of (1% in V-band and 4% in K-band). A possible solution to this problem is to create an artificial reference in the sky, the so called *Laser Guide Star*.

The first LGS concept came from the US Military, in a classified program, where they used a laser beacon to create artificial sources (Beckers [12]). A few years later the concept was proposed in the astronomical context by Foy & Labeyrie, 1985 [13]. At the moment, there are two common approaches to create reference sources with lasers in the sky: *Rayleigh LGS* and *Sodium LGS*. The first uses a laser beam sent in

the lower part of the atmosphere at ($\sim 20\ km$). The back-diffused light emitted due to Rayleigh scattering is collected by the telescope and used as a reference source, with a strong limitation in terms of atmosphere computation, due to the fact that this techniques is able to sense only the lower part of the sky. While the Sodium LGS, key component of this work, uses a monochromatic laser beam that emits at ($\lambda = 589\ nm$) to excite using resonance fluorescence, the Sodium atoms that are concentrated in the atmospheric Sodium layer of $\sim 13km$ of thickness at about 90 km height [14]. A detailed discussion of the Sodium LGS, appears in chapter 3.

Chapter 2

Astrophysical Applications of Adaptive Optics

2.1 The Galactic Center

The Galactic Center provides an ideal laboratory to study the physical processes occurring in the nucleus of our Galaxy and around its central supermassive black hole. Its study can be directly applied to the nuclei of other galaxies. One effective way to study the GC is to observe the stellar population in the region and AO is playing a fundamental role in this framework. Because of the obscuration due to the presence of dust in this region and of the difficulties to find bright guide stars at visible wavelenghts, AO would be a relevant improvement. Currently, NaCo (short for NAOS-CONICA) on the VLT is the only camera with a an infrared WFS [15]. These kinds of targets can also be observed at Keck II, being equipped with a LGS facility.

In the H-band on 8-10m class telescopes, ∼40 mas resolution can be achieved, allowing to trace the stellar distribution to scales below 0.04pc. By using $150 - 300\mu as$ astrometry, it has been demonstrated that the majority of the stars in the central parsec are old with randomly oriented orbits, while half of the young stars in the 10-15 region around Sgr A* are confined to a wrapped clockwise disk. This discovery has put strong constraints on the mechanism of star formation 6 Myr ago. Full 3D orbits of around 30 stars have been determined using a combination of astrometry and line-of-sight velocities, showing that Sgr A* is a supermassive black hole [16], [17]. Combined observations from Keck II and VLT allow us to measure the distance of the GC together with the mass of the central BH, for both of which the systematics associated with the distance is now the dominant error term. The current best values for these two magnitudes are 8.3 kpc and $4.3 \cdot 10^6 M_\odot$ [18]. Light curves of the near-IR flares of the accretion flow towards Sgr A* are now regularly observed. The analysis of their frequency, brightness and variation indicate that there may be two types. A power law distribution due to occasional bright flares from substructures and a lognormal distribution of faint continuous variability characterised by red noise. These data, together with tje spectral index, polarisation measurements and simultaneous multi-wavelength observations, provide constraints on the physical models of the flares emission [19].

2.2 Galactic Nuclei and Active Galaxies

2.2.1 Black Hole Mass

Measurements of Black Hole (BH) masses allow us to understand the relation between the growth of a Super Massive Black Hole (SMBH) and its host galaxy. This is done by analysing the relations between the BH mass and velocity dispersion, mass and luminosity of the stellar spheroid around it [20], [21], [22]. AO plays a fundamental role in increasing the sensitivity compared to optical longslit spectroscopy with the Hubble Space Telescope (HST). The high spatial resolution is coupled with a large collecting area and integral field spectroscopy at near-IR wavelengths. The work of Davies [23] shows that it is possible to measure BH masses in type 1 Active Galactic Nuclei (AGN) by using spatially resolved stellar kinematics. This provides a complementary tool to reverberation mapping, which is based on tracking the temporal variability of broad lines. In the case of NGC 3227, they claimed that the BHM was lower than previous measurements, being in the $7 - 20 \cdot 10^6 M_\odot$ range. The most recent measurement of this BHM of $(7.6 \pm 1.7)\, 10^6$ solar mass has been derived using the reverberation mapping technique [24] and they are consistent with this range. However, the uncertainties for measuring the BHM in quiescent or active galaxies are likely to be high because of the data quality, together with systematics and degeneracies associated with the distribution function of the stellar orbits, the existence of different stellar populations and the presence of nuclear gas masses [25]. The question of pseudo-bulges needs to be taken in account. In fact, they are formed by secular disk processes and not by mergers events, hence it is not clear whether the BH properties correlate with them in the same way as for classical bulges [26], [27]. It has been pointed out that many local galaxies have at least a pseudo-bulge component in the central regions [28], [29], and this might produce a scatter of disk galaxies in the $M_{BH-\sigma}$ plane. By using AO for measuring the M_{BH} in these galaxies, [30] claimed that the pseudo and classical bulge components need to be separated. Elliptical galaxies are a different case, Gebhardt [31] suggested that for these galaxies, the main uncertainty in the M_{BH} is linked to the treatment of the dark matter halo, an incomplete orbit library and triviality. In order to solve these issues in the case of M87, these authors combine AO integral field spectroscopy with a wider field data set and find a M_{BH} of $(6.6 \pm 0.4)\, 10^9\ M_\odot$. This result is not consistent with what one would expect from the $M_{BH} - \sigma$ relation by twice its uncertainty. This suggests that the high mass end of the relation is poorly constrained and its scatter is larger than what was expected.

2.2.2 Gas Inflow and Outflow

Local Active Galactic Nuclei (AGN) provide a fundamental tool to study the processes that drive the gas towards the central BH. The relative proximity of these objects allows us to reach a resolution of a few parsecs using AO. However, the big step is to combine AO with integral field spectroscopy, which allow us to probe the full 2D distribution and kinematics of stars, molecular gas and ionised gas. This technique applied to observations at optical or near IR wavelengths using AO has shown inward flows of gas with a relatively low rates along the circumnuclear spiral arms in different galaxies [32], [33], [34], [35]. Despite exceptions, such as the case of NGC 1068 where the gas appears to fall directly towards the AGN, this inflow is in principle sustainable for Gyr timescales [32]. This material is believed to be related

to the circumnuclear dust structures mapped in different active and inactive galaxies, implying that the gas streaming might be common but its relation with the AGN accretion is not yet clear. In fact, one might expect that such process of gas brought at tens of parsec from the central region should result in a starburst. However, the role of nuclear star formation in the AGN feeding process is still an open question. The analysis of optical [36] and infrared [37] data of stellar population synthesis shows that some AGN might appear to be associated with recent starbursts (< 100 Myr old), while the nuclear stellar spectra of other AGN are dominated by intermediate or old populations. Davies [38] and Wild [39], suggested a possible solutions to this issue. By using AO to observe scales below a tenth of a parsec, they claimed evidence of a young starburst being associated with weak AGN accretion, while the AGN feeding is more efficient after the starburst stops and the turbulent stellar feedback has ended. Schartmann [40] has shown that hydrodynamical simulations support these results. In fact, stellar ejections post-starburst might produce at 1 parsec scales a turbulent gas disk, which is consistent with observations of masers. In the case of this gas coming from the disk, the results of the simulations imply that the torus is a dynamically evolving structure, having different components responsible for the various phenomena observed. These include small scale structures seen with VLTI [41], [42], together with larger scale components [43]. Mapping the locations of different age-stellar populations using AO integral field spectroscopy [37] should provide important results on how the nuclear starburst is linked with the torus and AGN fuelling.

In the case of Seyfert galaxies, where the luminosities are moderate, the gas required to fuel them is smaller than other sources, so the question is whether the larger inflowing gas is piling up or expelled. Also in this case, AO coupled with integral field spectroscopy is showing results about AGN outflows with observations of their ionised and coronal line emission, Riffel [37]. The method employed is complementary to the longslit spectroscopy technique with HST [44]. Outflow rates are measured to be 100 or more times greater than the accretion rate onto BH, showing that AGN driven winds are entraining a significant amount of gas from the local Interstellar Medium (ISM). The complex interaction between the local ISM and the outflow has been studied with models of the outflow geometry. This analysis shows hints that the greater the amount of molecular gas in the vicinity of the AGN, the faster and narrower the outflow. These results show how AO is the fundamental technology to better understand galaxy evolution, by probing the detailed physics of outflows in local AGN.

2.2.3 Quasars and Mergers

Probing small scales in the case of Quasi-Stellar Object (QSO) sources provides an observational challenge, due to their distance and the overwhelming brightness of the AGN compared to the host galaxy. By analysing a survey of 32 nearby QSO using Gemini North and Subaru, [45] have shown that the key is to know the PSF in order to accurately subtract it and reveal the host galaxy. However, when high redshift sources are observed, the surface brightness becomes fainter and even with AO systems, the host galaxy is difficult to detect [46], [47]. A different approach can be investigated by observing nearby luminous merging systems, such as the well known case of NGS6240. This dual AGN has been observed several times with AO. These analyses have revealed numerous massive young star cluster close to the nuclei, that were not detected with HST images (Schneider [48]). The location of

the two AGN has been revealed by comparing AO images from K-band (2.1 μ m) to L-band (3.8μm) with X-ray and radio continuum data (Max [49]). Even if the AGN are highly obscured, the extinction observed in mergers is not prevalent (Engel [50]). When AO data are combined with HST images, their extinctions appears to be consistent with the Calzetti [51] reddening law. New constraints on the merger geometry are now provided by spatially resolved stellar kinematics obtained with AO [50] and have shown that the BH in the southern nucleus lies above the high mass end of $M_{BH-\sigma}$ relation (Medling [52]). Further improvement to this field will be given by increasing the performance of AO systems when using faint references, which is the case of the QSO. The Large Binocular Telescope (LBT) WFSs will be soon upgraded to SOUL, which uses detectors essentially RoN free, pushing the performance on faint targets to a quality never reached before and obtaining the same level of Strehl on targets 1-2 magnitude fainter. The SHARK-NIR and SHARK-VIS instruments that will be soon installed at LBT, are capable of performing coronagraphic imaging and low resolution spectroscopy from 0.6 to 1.7 μm wavelength. Thus they will have the possibility to study a much wider sample of AGN and QSO, allowing to reveal even the faint host galaxies of the QSO so difficult to be detected with the currently available AO systems.

2.3 The High Redshift Universe

One of the most impressive AO applications has been to spatially resolve the internal structure and kinematics of star forming galaxies at $z \sim 1.5-3$, which is the epoch of peak mass assembly. These objects have dimensions of 1-2 arcmin and the emission lines used to study the dynamical and physical properties are redshifted to the near-IR. These targets are ideal for using the AO technique, but the deep fields where such galaxies are identified are missing bright stars. Moreover, the low surface brightness means that the spatial resolution is limited to 0.1-0.2 arcsec by instrumental and observational constraints, making the use of AO challenging. Forster-Screiber [53] used AO only on 12 objects from the 63 high-redshift galaxy present in their large spectroscopic imaging survey. Also, Law [54] detected only 13 of their objects using AO, Wright [55] only 6 galaxies, Wisnioski [56] 13, and Mannucci [57] only 10. These works show that the severe selection criteria allow only 10% of high redshift galaxies to have a suitable guide star within 30-40 arcsec, and when other criteria are taken into account this fraction drops to $\sim 1\%$ [57]. AO have confirmed through kinematic studies that massive star forming galaxies at $z \sim 2$ are not necessarily evolved through mergers but can also be gas-rich disks, and thus it is now believed that about 1/3 of these galaxies are in fact disks [53]. For one object, these disks are unlike to be those of local galaxies. In fact, they are rapidly forming stars in giant star-forming clumps and they have high intrinsic velocity dispersion of 20-100 km/s Cresci [58], Law [54], Wright [55]. Recent studies suggested that these values of velocity dispersion are characteristic of normal massive high-redshift disks, linked to the high gas accretion rates through cold flows at early cosmic times, high gas fractions and global instability to star formation. AO is the key tool to separate the ~ 1 kpc sized clumps from the inner clump regions, which are blurred together in seeing-limited observations. Higher liner resolutions of ~ 100 pc can be reached with AO when applied to gravitationally lensed objects. Impressive results have been achieved by using AO together with integral field spectroscopy. In particular, studying the detailed properties of individual clumps, showing that they can drive

winds with flow rates exceeding their star formation rates (Genzel et al., 2011). This process has fundamental consequences on the lifetimes of clumps, and thus on galaxy evolution, for example whether they survive long enough to migrate inwards and build a nascent bulge (Genzel et al., 2008) or fuel the AGN (Ammons et al., 2009, Wright et al., 2010). Thanks to the use of AO combined with integral field spectroscopy, this research field is growing strongly. Even if few, the observations have improved our understanding of galaxy evolution.

Chapter 3

Laser Guide Stars

3.1 General Properties and Limitation

Generally speaking, LGS suffer from some non-negligible limitations. First of all, they are not sensitive to tip-tilt. In fact, the laser beam, during its path starting from the laser (on the ground) and then reaching the detector (on the ground, again), goes twice through the same part of atmosphere in a time interval which is shorter than the mean time scale of the variation of mean inclination introduced by the atmosphere to the wavefronts. This means a Natural Guide Star (NGS), is always needed to measure the tip-tilt. Second, due to the finite distance between the telescope and LGS, the back-scattered beam does not sample the full aperture at the height of the turbulent layers. This is known as the *cone effect or anisoplanatism* presented in Figure 3.1, and it is more severe for larger apertures and higher turbulent layers. In addition, it has been verified that the sodium layer height varies

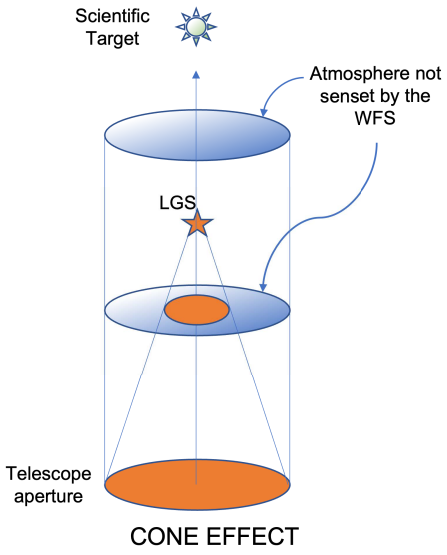

Figure 3.1: *Schematic representation of the LGS cone effect.*

seasonally and also during the same night, up to hundreds of meters or even kilometers. This causes a defocus problem, which needs to be sensed, regaining the capability of sensing defocus for the NGSs WFSs. It has also been pointed out that not only tip-tilt and defocus but orders up to Zernike mode 36 need to be sensed,

as well, transforming the simple tip-tilt-defocus WFS into a more complex one [59].

Last but not least, the sodium layer, as anticipated in section 1.4.3, is known to have a certain thickness and density distribution, both varying with time, as shown in Figure 3.2.

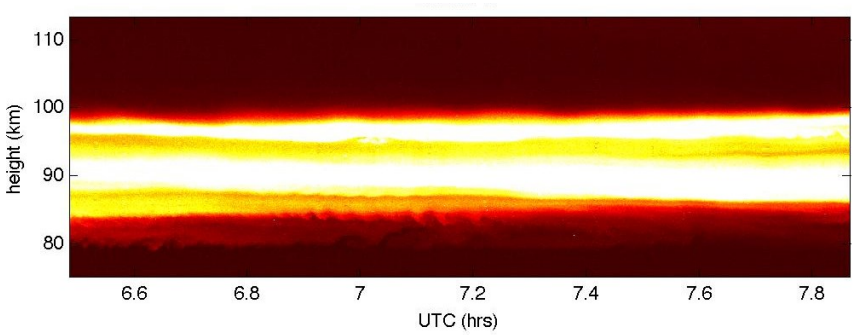

Figure 3.2: *Sodium layer density profile as function of time.*

For this reason, the LGS cannot be considered as a point-like source, but more as an object extended in a 3D volume with a given orientation in the sky. In a focal plane WFS, like the SH-WFS, the image of the LGS will be only partially in focus, since the source extension along the optical axis (Z-axis in the following) is not negligible with respect to the LGS altitude. In particular, when trying to select the best focal plane orthogonal to the chief ray, only the central part of the source will be actually in focus, while its edges will be defocused, as shown in Figure 3.3.

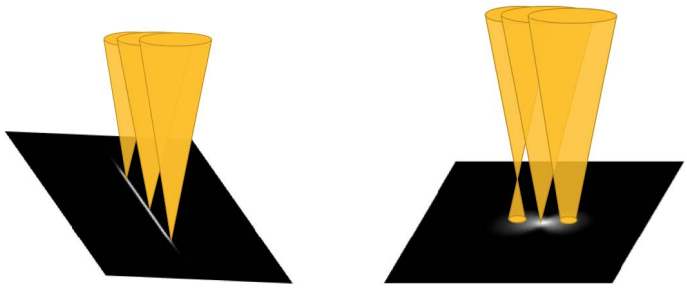

Figure 3.3: *Effect of selecting the best focal plane orthogonal to the chief ray for a LGS re-imaging system.*

3.2 Laser Guide Stars as Extended Objects

The 3-dimensional nature of the LGS provides one more issue related to the relative dimension in the sky. Considering again the SH-WFS, that for instance is the current baseline for the LGS WFS for the future ELT AO instruments [**males**]. The LGS spots appear elongated in the sub-apertures located far away in the limit of the pupil with respect to the laser launcher position. The spot elongation translates into a decrease in the sensitivity of the signal of the local wavefront first order derivative, which will then be dependent on the sub-aperture position on the pupil and on the LGS orientation. Obviously, the bigger the telescope diameter, the stronger the

effect. According to Figure 3.4, the estimation of the angular elongation dimension is given by:

$$\theta_{elong} = \beta - \alpha \tag{3.1}$$

where α and β are:

$$\alpha = \tan \frac{(X_P + X_{LLT})}{H + dH} \tag{3.2}$$

$$\beta = \tan \frac{(X_P + X_{LLT})}{H} \tag{3.3}$$

Equation 3.1, in the small angle approximation, is:

$$\theta_{elong} \sim \frac{(X_P + X_{LLT})\, dH}{H^2 + HdH} \tag{3.4}$$

where dH is the thickness of the Sodium layer, H is the mean altitude of the sodium layer and $[X_P + X_{LLT}]$ is the distance between the pupil sub-aperture and the laser launcher telescope.

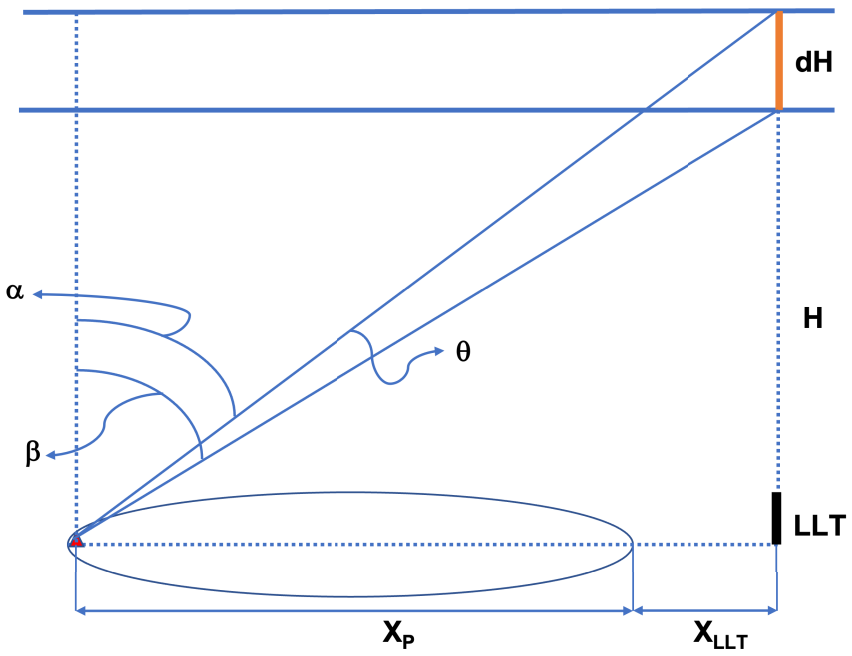

Figure 3.4: *Elongation of the LGS image at a distance $X_P + X_{LLT}$ from the launcher. dH represents the thickness of the Sodium layer, H is the mean altitude of the layer and θ is the angular elongation.*

Assuming a mean height $H \sim 90km$ and $dH \sim 10km$ in the ELT framework the spot elongation is of the order of 12 arcsec, for the furthest sub-aperture with respect to the LLT position. This is at 19m from the optical axis of the telescope. Hence, this case corresponds to an elongation ratio of around 24 between the long axis and the short axis of the spot imaged through the furthest sub-aperture from the laser launch telescope. This means that for this sub-aperture the photon noise variance is $\sim$ 600 times larger along the long axis. In other words, the small axis component of the measurement is worth several hundreds of long axis measurements in terms of SNR. Moreover, beyond a degraded SNR, the spot elongation yields a bias in the reconstructed wavefront when the spots are truncated and not properly sampled. Figure 3.5 shows an illustration of LGS spot elongation on a SH-WFS focal plane at the ELT [60].

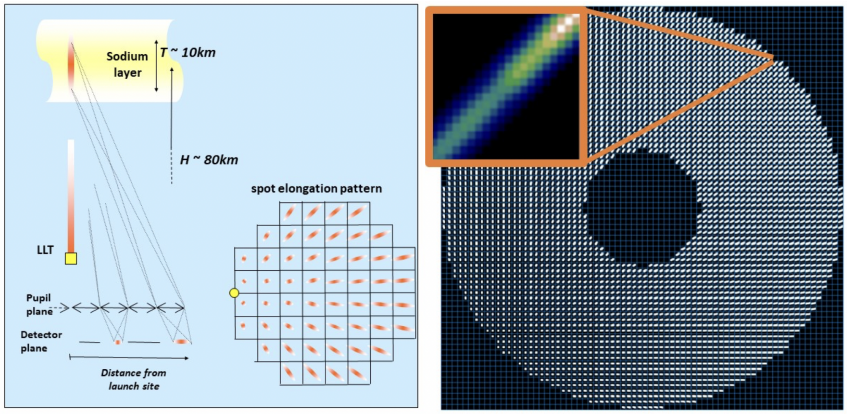

Figure 3.5: *Illustration of LGS spot elongation on a Shack-Hartmann focal plane at the ELT.*

In this framework, we propose a new pupil plane WFS, designed to cope with the issues of the LGS imposed by the natural characteristics of the sodium layer. A full description of this new device, called the Ingot Wavefront Sensor appears in Chapter 4.

Chapter 4

The Ingot Wavefront Sensor

The aim of this work is to present a new kind of pupil-plane Wavefront Sensor that can take into account the intrinsic nature of LGSs. As described in the previous chapters, sodium LGSs, despite their name, cannot be fully considered as real stars. They are placed at a finite distance, and if fired from the side of a large telescope, their characteristics change dramatically depending on the position on the entrance pupil from where the source is being observed. In this chapter we present the two possible version of the designs of the Ingot Wavefront Sensor (I-WFS).

4.1 The Ingot Wavefront Sensor - Old Fashion Design

It is well known that, even though SH-WFS for LGS in wide pupil telescopes, such as the ELT, have some issues like spot truncation or focus uncertainty, they are still a feasible and reliable method/approach. Differently, the I-WFS aims to optimize the 1:1 matching between the source and the WFS in order to sense it. The key of the concept is to make the source image really focus on the element used to discriminate the parts of the wavefront affected by different local first-derivatives, in order to increase the signal-to-noise-ratio (SNR) of the measurement, in according to the nature of the LGS, that doesn't focus in a single plane, as shown in Figure 3.3. The original concept assumes that the LGS image is divided in its actual focal plane (inclined with respect to the chief ray), namely in six parts, as shown in Figure 4.1.

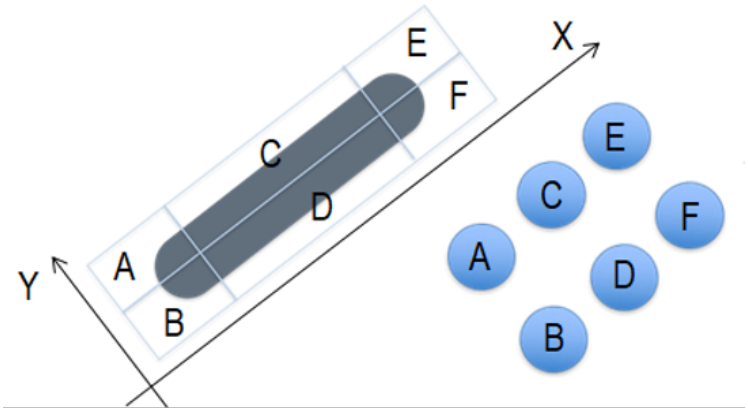

Figure 4.1: *Left: LGS sampling in its own focal plane. Right: LGS Re-imaged pupils.*

The 6 separated beams will then be re-imaged onto six corresponding pupils, similar to the P-WFS. The signals will be computed using the intensities obtained in a 6-quad-like style, as follow:

$$S_x = \frac{(E+F)-(A+B)}{A+B+E+F} \tag{4.1}$$

$$S_y = \frac{(A+C+E)-(B+D+F)}{A+B+C+D+E+F} \tag{4.2}$$

where A,B,C,D,E,F are the integrated pupils intensities. We can distinguish two different situations, depending on the origin of the light. The light on the pupils produced by the four sides areas (i.e. A,B,E and F) will provide Information on the wavefront derivative derivative along both axis. In contrast, the light on the two central faces will only contribute to the derivative signal in the direction orthogonal to the spot elongation, under the assumption that the central faces mostly carry noise for this signal. The element used to split the 6 parts of the incoming wavefront is a six-faces, partly refractive and partly reflective prism, resembling the P-WFS approach. The concept of the I-WFS, consists of a combination of refractive and reflective surfaces arranged onto a complex prismatic shape that extends in three dimensions along the locus where the reference beacon deploy in the focal volume, as shown in Figures 4.2 and 4.3.

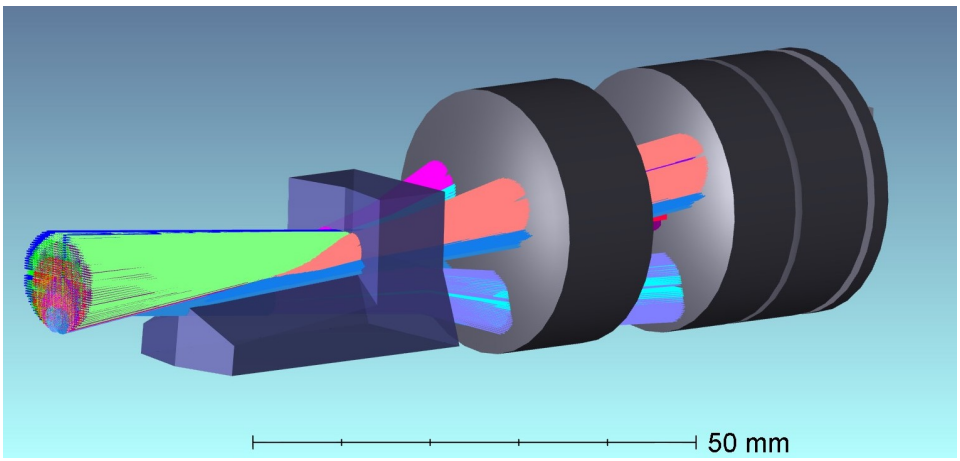

Figure 4.2: *3 dimensional optical design of the I-WFS*

While, Figure 4.4, shows the I-WFS with the LGS light coming from the lower left side. We can notice that, upon the relative position along the prism all the six faces are illuminated. In contrast with the P-WFS, and also because of the extended nature of the reference, the illumination of the six pupils with zero turbulence is not uniform and reflects the different elongation as seen from diverse sub-apertures on the pupil. In addition to general advantages, like the ability to sense somehow the differential piston in the entrance wavefront, pupil plane WFS can also allow the system to optimize the pixels occupation. To sample each sub-apertures, in fact, a SH-WFS, needs a number of pixels, which is large enough to Nyquist sample the smallest re-imaged spot, (which has an angular size comparable to the one of the SH focal spots in the equivalent NGS wavefront sensing), but also the minimum field of view needed to include the most elongated spot. Typical number of required pixels for each sub-aperture in a SH-WFS for LGS at a ELT-like telescope is of the order

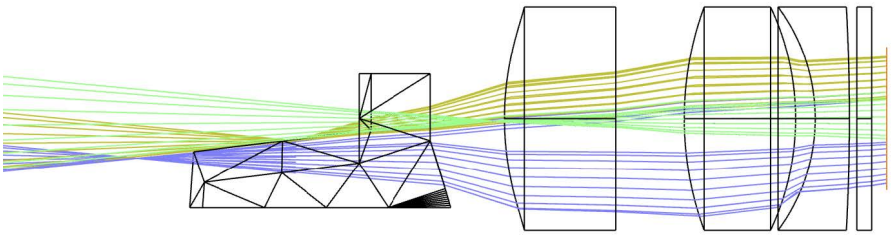

Figure 4.3: *2 dimensional optical design of the I-WFS*

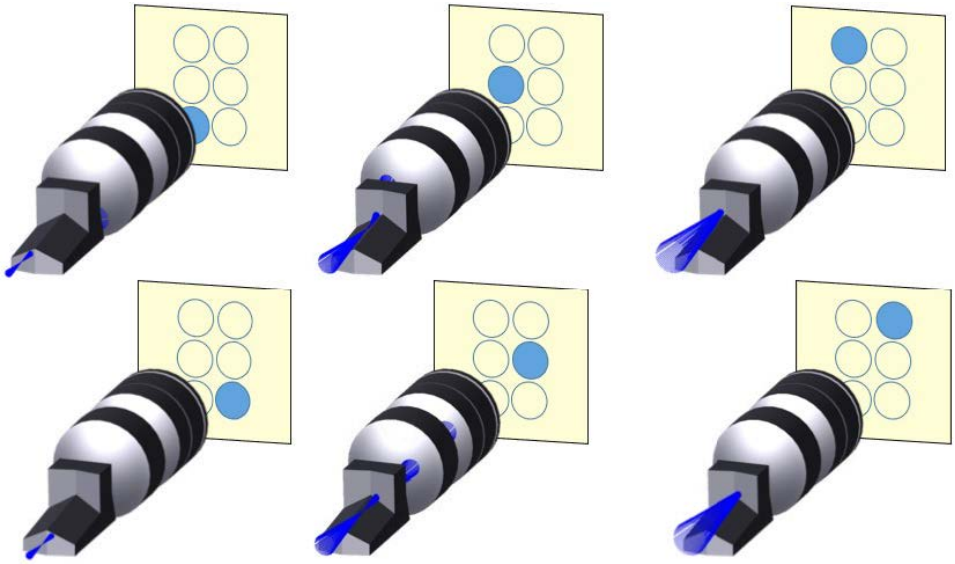

Figure 4.4: *The distribution of the light into the I-WFS*

of 10x10 pixels, while the P-WFS and the I-WFS, only require 4 and 6, respectively as shown in Figure 4.5

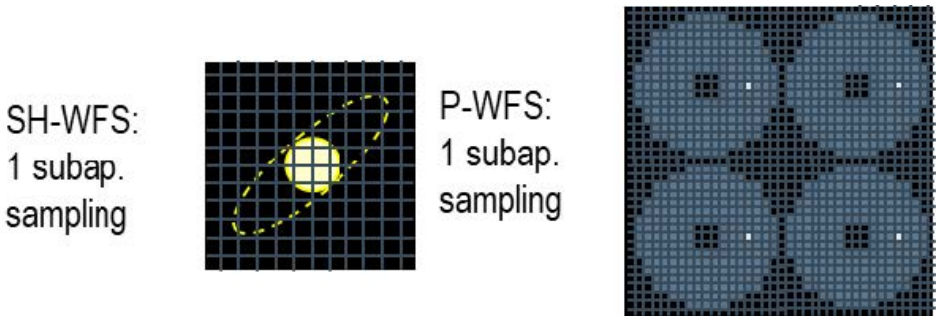

Figure 4.5: *Difference in pixels occupation for a SH-WFS (left) and a P-WFS (right), in the LGS sensing case. In the SH-WFS focal plane, re-imaged spots have different angular sizes.*

Each sub-aperture in the entrance pupil sees the LGS under a different solid angle. The sub-apertures close to the LLT identify the LGS as a point source, which mainly extends along the Z-axis (projected as a point-like source), instead, the farthest sub-apertures see the LGS as an extended object, which also lies in the X-Y plane. As we saw in the previous section, a SH-WFS produces re-imaged spots with different sizes, depending on the position of the sub-apertures that generate them. The spot elongation, for a four-quadrant-based WFS like the SH-WFS (but also the Pyramid WFS), translates into a decreased signal sensitivity to the local wavefront first order derivative, which will then be dependent on the relative sub-aperture position on the pupil and on the LGS orientation. The importance of this effect increases with the telescope pupil diameter. In the I-WFS, the sub-apertures also see the ingot prism itself under the same projection as the LGS. As an extreme case, the closest sub-aperture to the LLT will only see 4 of the 6 ingot faces, while the farthest will see all of the 6 ingot faces, as shown in Figures 4.6 and 4.7.

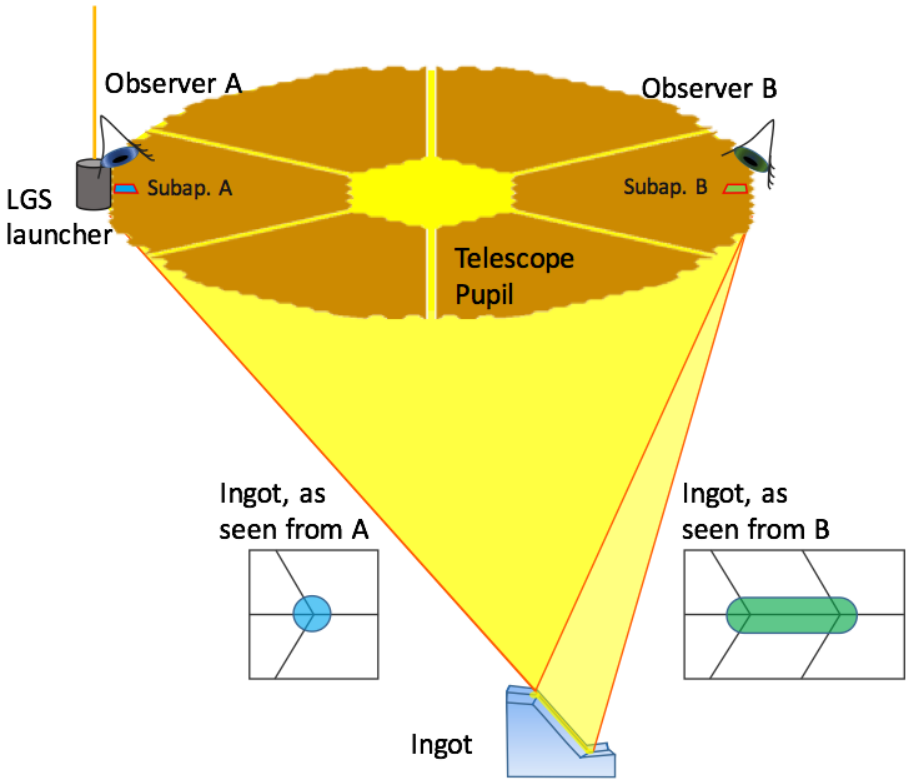

Figure 4.6: *I-WFS as seen from the sub-apertures close to the laser launcher position (A) and seen from sub-apertures far from the laser launcher position (B).*

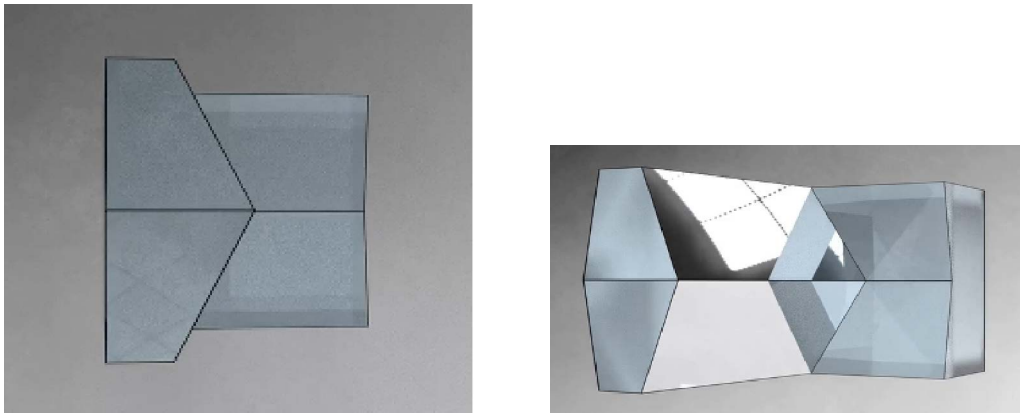

Figure 4.7: *Left: I-WFS projection as seen from the sub-aperture (A) the closer to the laser launcher position. Right: I-WFS projection as seen from the sup-aperture (B) the farthest to the laser launcher position.*

Since the design of the I-WFS is optimized to match the geometric characteristics of the LGS image, when the Sodium layer thickness changes, and thus the actual size of the source varies, the LGS image will no longer be able to match the geometry of the I-WFS prism. This variation can affect the pupils illumination in extreme cases, as shown in Figure 4.8.

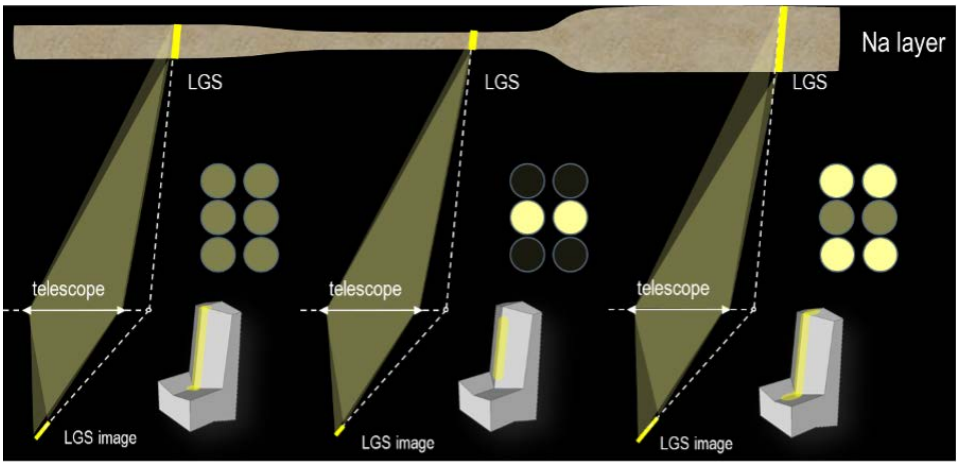

Figure 4.8: *Effect of sodium layer variation on the LGS image matching the Ingot prism*

For this reason, we considered the possibility of having more ingot prisms for a single I-WFS, to be used according to the thickness variations of the Sodium layer. To overcome this issue a possible different Ingot design, only using one of the two LGS edges to discriminate the X signal, has been investigated, and it will be described in the next section.

4.2 The Ingot Wavefront Sensor - Current Design

In order to reduce the complexity and make the I-WFS more adaptable to the sodium layer variations, an additional prism design was developed, for which the vertex of the prism is constrained to the lower edge of the Sodium layer, using the tip-tilt term, which is typically not used for LGS wavefront sensing. In according with the previous designed and to the P-WFS, the pupils are used to calculate signals proportional to

the first derivative of the wavefront. In the following equation, we define the signals S_x and S_y along the x and y directions (x denotes movements orthogonal to the elongation direction, while y denotes movements along the elongation direction), in according with Figure 4.9 as:

$$\begin{aligned} S_x &= \frac{B-C}{A+B+C} - \frac{B_{ref}-C_{ref}}{A_{ref}+B_{ref}+C_{ref}}, \\ S_y &= \frac{A}{A+B+C} - \frac{A_{ref}}{A_{ref}+B_{ref}+C_{ref}}. \end{aligned} \tag{4.3}$$

The operation is done pixel-wise such that a signal S_x and S_y is obtained for every

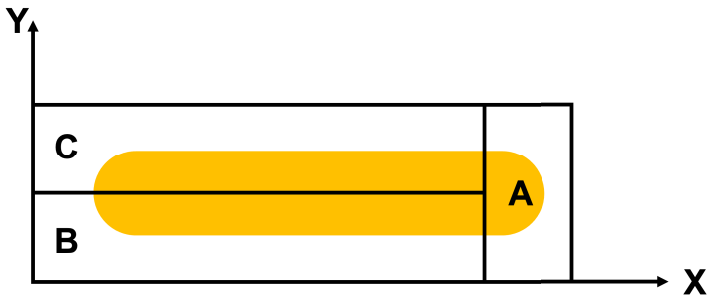

Figure 4.9

pixel. Note that we subtracted the reference signal (also called reference slope), which is the signal that we consider the zero point in our calibration.

The new design was expected to fulfill the following characteristics:

- Match the geometry of the LGS image and split the light at the level of the LGS focal plane into 3 beams, producing 3 images of the ELT entrance pupil
- Efficient light throughput
- Avoid overlapping of the output pupils

According to the ELT AO and sodium layer parameters, the LGS image tilt angle with respect to a focal plane perpendicular to the optical axis is 83.67°. Correspondingly, the angle of incidence of the LGS chief ray at the LGS focal plane is also 83.67° and, considering the cone angle of the F/5 input beam, in according to the MAORY-ELT optical design [61], the range of angles of incidence is $77.96° - 89.38°$. At such grazing incidence, a refractive solution is highly inefficient due to the high selectivity at air-glass interface. For this reason, to minimize light losses, the current design of the ingot prism foresees the use of a reflective prism rather than a refractive one. The prism is a simple reflective roof whose roof line is placed along the long axis of the LGS image to intercept only part of the LGS's light. The light reflected by the roof prism faces forms two images of the pupil, while the rest of the light reaches the re-imaging optics without touching the prism and forms a third image of the pupil. We label the transmitted pupil as A and the reflected ones as B and C, as shown in Figure 4.10. Notice that the system is able to focus the different beams on the same plane due to the telecentric nature of the incoming beam

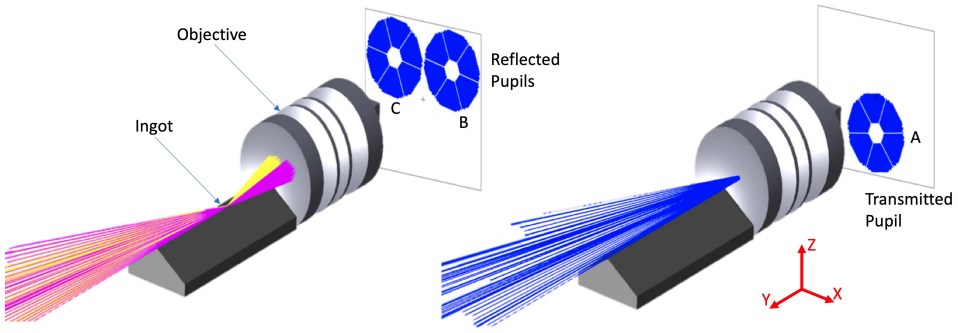

Figure 4.10: *Conceptual layout of the ingot prism. Part of the LGS is focused by the reflecting ingot roof and forms two pupils while the remaining part of the LGS is focused after the ingot and is transmitted directly to the pupil re-imaging optics forming the third pupil*

4.2.1 Roof apex angle and pupil separation

The apex angle of the prism must be such to avoid overlapping of the output pupils. In order to achieve a proper separation, the angle between the chief rays reflected by the two faces of the roof should be greater than the input F/5 cone angle (in accordance with the requirement imposed by the ELT: F/5 telecentric beam), and the same should be valid for the angle between the transmitted chief ray and the reflected ones. Defining Z the axis parallel to the telescope optical axis, X the axis parallel to the elongation direction and Y according to the right hand rule, the reflective faces are obtained by rotation of a plane perpendicular to Z by an angle θ_Y around the Y axis and by an angle $\pm\theta_x$ around the X axis, Figure 4.11. According to Figure, the rotation around the Y axis can be considered as a tilt of the whole roof to place its edge along the LGS image, while the rotation around the X axis is related to the apex angle α of the roof prism as:

$$\alpha = 180^\circ - 2\theta_X \tag{4.4}$$

Performing first the rotation around Y and then the rotation around X, it can be demonstrated that the resulting angle θ_1 between the chief rays reflected by the roof is given by:

$$\theta_1 = a\cos\left(1 - 8\cos^2(\theta_Y)\cdot\cos^2(\theta_X)\cdot\sin^2(\theta_X)\right) \tag{4.5}$$

While the angle θ_2 between the reflected chief rays and the transmitted one is:

$$\theta_2 = a\cos\left(1 - 2\cos^2(\theta_Y)\cos^2(\theta_X)\right) \tag{4.6}$$

In order to place the edge of the roof along the LGS image, the angle θ_Y should be:

$$\theta_Y = a\tan\left(\frac{F_\# \cdot D_{tel}}{LLT_{offset}}\right) = 83.67^\circ \tag{4.7}$$

The other necessary condition is to have both θ_1 and θ_2 greater that the cone angle of the input beam, in order to separate the output pupils. Imposing that the separation between the reflected pupils is equal to one sub-aperture (i.e. 1/80 of the pupil

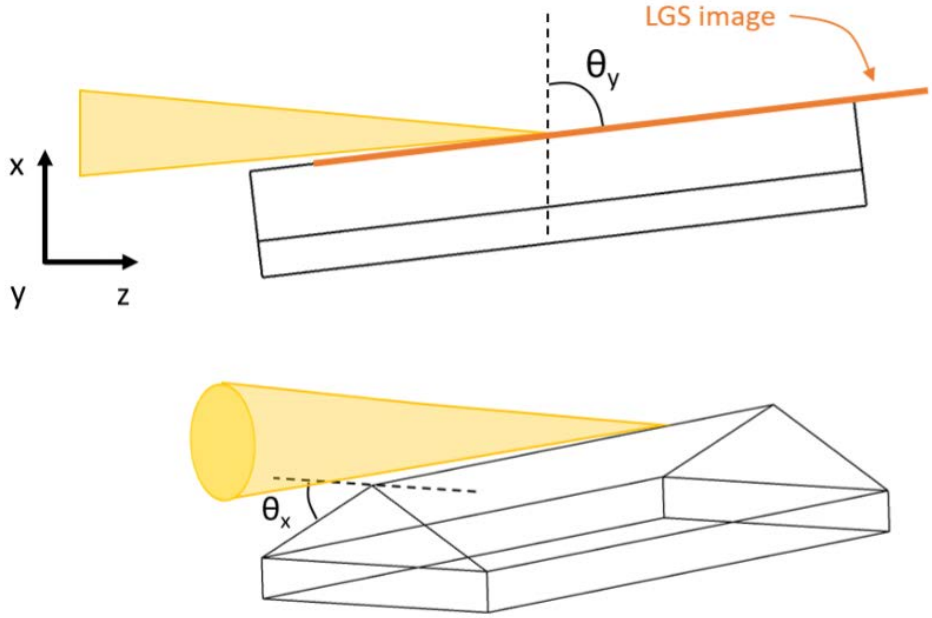

Figure 4.11: *Top: side view of the ingot with definition of axes. Bottom: perspective view of the ingot. The illuminating cone of light is shown in yellow.*

diameter) corresponds to solving the following equation for θ_X:

$$a\cos\left(1-8\cos^2\left(\theta_Y\right)\cdot\cos^2\left(\theta_X\right)\cdot\sin^2\left(\theta_X\right)\right)=2\arctan\left(\frac{1}{2F_{\#}}\frac{161}{160}\right) \tag{4.8}$$

Numerically solving the above equation gives $\theta_X \simeq 30°$. Replacing the values obtained for θ_X and θ_Y to get the angle between the reflected beams and the transmitted beam, we find:

$$\theta_2 = a\cos\left(1-2\cos^2\left(\theta_Y\right)\cos^2\left(\theta_X\right)\right)=10.96° \tag{4.9}$$

This values is slightly smaller than the corresponding F/5 cone angle (11.42°), meaning that the reflected pupils will slightly overlap with the transmitted one. Unfortunately, we saw that changing the input $F/_{\#}$ has no beneficial impact on the resulting pupil overlap, as shown in Figure 4.12. The only possible way to avoid the overlap is to add a constraint to θ_Y (i.e. tilt the roof prism with respect to the LGS image plane). Tilting the Ingot prims by 0.3° from its nominal position, coresponding to $\theta_Y = 83.17°$, is enough to remove the pupil overlap and to give a clearance of about 1 sub-aperture between the re-imaged pupils. To graphically prove what we just described, we can use a sample image of the three pupils calculated by Zemax-OpticStudio ray-tracing, as shown in Figure 4.13. The right part of the figure shows how the overlap is solved when the prism is tilted by 0.3° from the perfect LGS focus position.

To determine the correct length of the Ingot prism, we have to consider the size

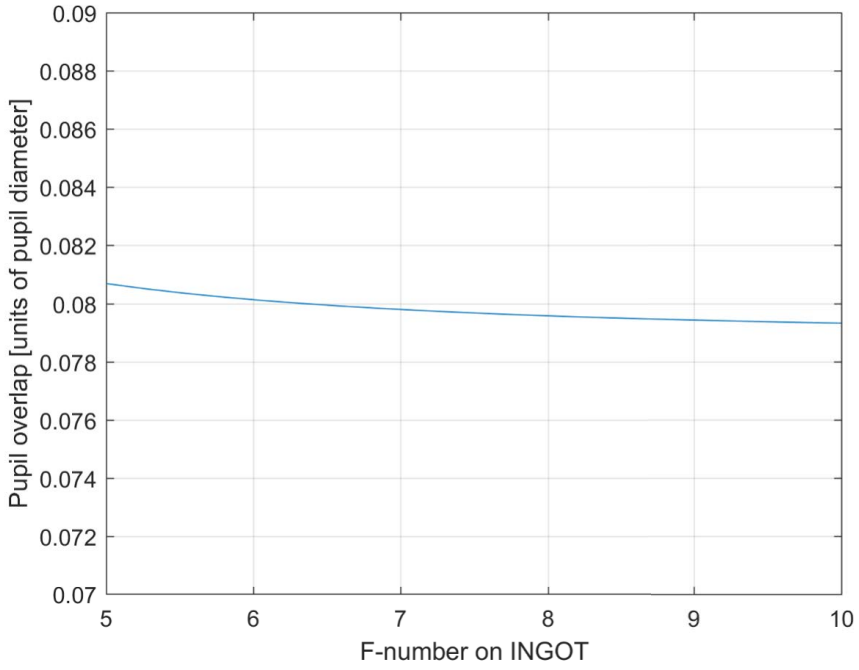

Figure 4.12: *Overlap between reflected and transmitted pupils as a function of the input* $F/_{\#}$

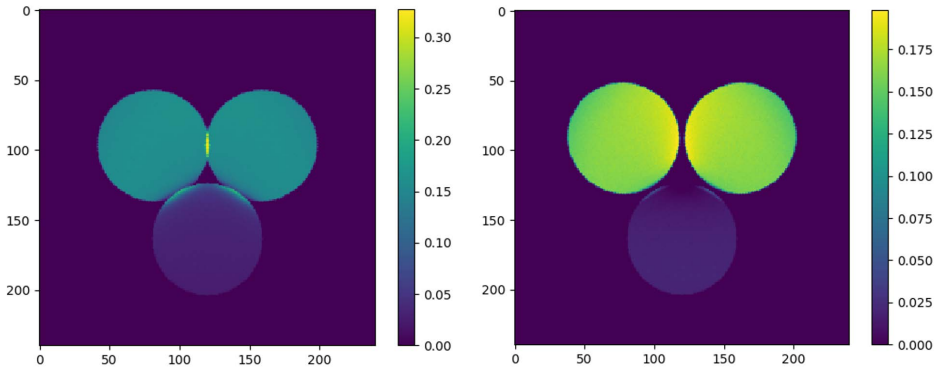

Figure 4.13: *Image of the three pupils obtained by ray-tracing through the ingot prism. Left: the ingot prism is placed on the focal plane of the LGS. Right: the prism has been tilted by* $0.3°$ *with respect to the perfect focal plane of the LGS to separate the pupil images*

of the LGS image. The longest possible LGS image length occurs when the sodium layer is thick, closer to the telescope and the telescope is pointing at the zenith angle. Assuming a maximum sodium thickness layer of 20 Km, a minimum height of 84km and zenith pointing, the corresponding maximum LGS image length will be 107 mm. The expected maximum LGS spot size is 1.5", corresponding to an image width of 1.4 mm. Thus, using a prism roof 110 mm long and 4 mm wide should be enough to accommodate the biggest LGS image.

The advantage of this design (compared to the previous one [62]) is that it adapts to thickness variations of the sodium layer (i.e., length of the LGS star) without the need to change the ingot prism. Instead, it is only necessary to have a roof prism

long enough to accommodate the maximum length of the LGS image. The ratio between the flux in the transmitted pupil and that in the reflected pupils can be adjusted by moving the prism along the direction of the edge between the reflective faces, as shown in Figure 4.14.

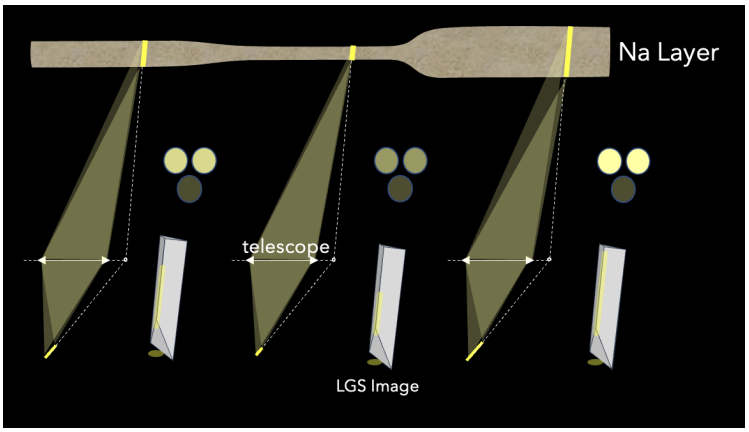

Figure 4.14: *I-WFS response to the sodium layer thickness variations*

Chapter 5

The I-WFS @ the LOOPS bench

This chapter, presents the results of a collection of tests of the I-WFS performed at the LOOPS adaptive optics facility, hosted at the Laboratoire d'Astrophysique de Marseille (LAM) [63], using a Spatial Light Modulator (SLM). This device is both able to produce a high definition phase mask that can mimic the two-dimensional behavior of severall well-known wavefront sensor, and to work as a high resolution turbulent phase screen. We performed two runs which differ in the spatial resolution of the disturbance applied. In addition, we present an End2End numerical tool of the I-WFS in order to perform the analysis of a closed-loop complete system.

5.1 The LOOPS test bench

LOOPS is an adaptive optics facility hosted at LAM focusing on the study of Fourier-filtering wavefront sensors. The LOOPS bench allows testing of the I-WFS in a quasi-real AO closed-loop context, but simulating the wavefront sensor with a 2di-mensional manner. The optical scheme of the LOOPS test bench appears in Figure 5.1:

The bench is divided into four blocks: (I) a common path, (II) a metrology path, (III) a classic PWFS path, and (IV) a Fourier-based path, as described in previous work [64]. The peculiarity of this facility is the presence of a SLM, shown in block (IV). This device is a Hamamatsu SLM (LCOS-SLM X13138) with 1024×1280 pixels (with a 12.5 μm pitch) that can produce arbitrary phase masks modifying its shape. It uses liquid crystal technology and exploits the birefringence properties of the crystals to produce software-configurable phase masks. In the case of the LOOPS facility, it is placed in a focal plane to reproduce two-dimensional phase masks of wave-front sensors acting on a focal plane. Other components of this facility, used to test the I-WFS are:

- Monochromatic point-like source (**S** in Figure 5.1) generated from a laser diode and feeding an optical fiber at a wavelength $\lambda = 660nm$
- PI piezoelectric tip-tilt mirror (**TTM** in Figure 5.1) that produces the modulation of the point-like source. It is controlled in an open-loop mode and operated at 500 Hz.
- Continuous-sheet Deformable Mirror (**DM** in Figure 5.1) from ALPAO with 69 actuators. Nine actuators fit across the diameter of the pupil

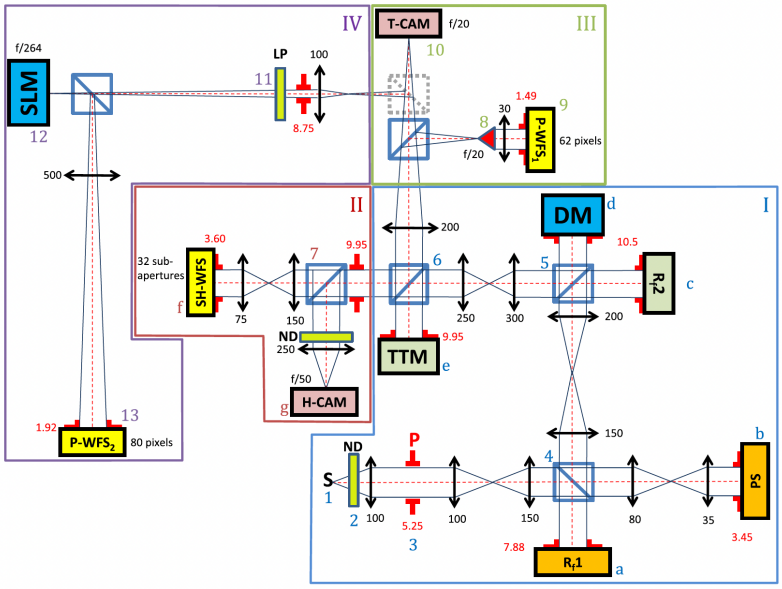

Figure 5.1: *Optical Design of the upgraded LOOPS bench facility. (I) is the common path optics, (II) a metrology path, (III) the classic P-WFS path, and (IV) the Fourier-based WFS path including a Spatial Light Modulator (SLM).*

- SH-WFS that samples the pupil diameter with 32 sub-apertures and serves as reference WF metrology system

At this point, it is fundamental to understand that the I-WFS collapses different pupil viewpoints in one single device, as shown in Figure 5.2. As seen from one single sub-aperture, the inclination of the I-WFS prism changes with the distance from the edge. The approximation of the three-dimensional geometry, cannot be reproduced in a two-dimensional system in a straightforward way. To cope with this issue, we opted for the simulation of three different phase masks, each representative of a single perspective viewpoint.

In such configuration, we found three different phase masks, which differ for their projection of the prism roof. These differences correspond in the two-dimensional picture to as many shapes, that we draw starting from the angle shown in Figure 5.3. In the following, we refer to these respectively as: **T0**, **T15**, and **T30**.

It is fundamental to understand that the I-WFS has been simulated on the bench using the SLM, reproducing a 2D version of the WFS itself. On the same time, to realized the LGS elongation on the bench, we used the fast tip-tilt mirror (TTM) to introduce an elliptical modulation to the available point source. We calculated the length of the extended source considering the ELT scenario and system parameters, taking into account the sodium layer thickness (around 20 km), identifying 3 source aspect ratios, between the minor and major axis of the source, depending on the position of the pupils from where the LGS is seen. The three aspect ratio are: 1:7 - 1:15 - 1:30.

Different portions of the pupil have correspondingly different geometry. We take into account three cases corresponding to different sub-aperture over the telescope pupil, starting with the closest to the laser launcher position (considering a single laser launcher located at the edge of the telescope), and ending with the one on the opposite edge of the pupil, considering, in addition, on in the middle as shown in Figure 5.4.

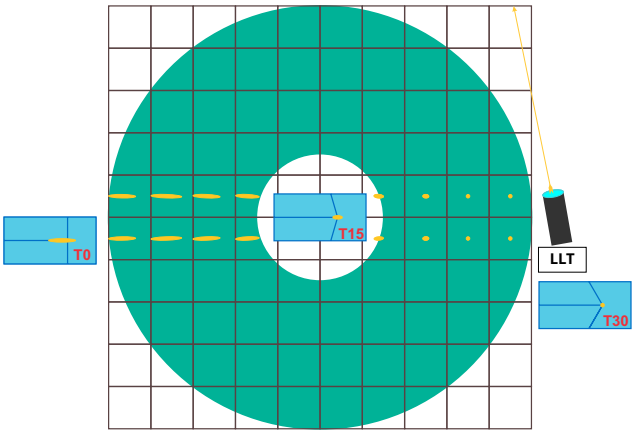

Figure 5.2: *Picture shows some of the sub-aperture of a Shack-Hartmann like WFS as illuminated by a laser, fired on the side of the primary (from the Laser Launching Telescope (LLT)). Each sub-aperture has its own perspective of the emitting sodium profile. A similar perspective effect happens also at the Ingot focal plane as depicted schematically for the sub-apertures #1, #2 and #3. The dimensions of masks, LLT and elongation are not in scale.*

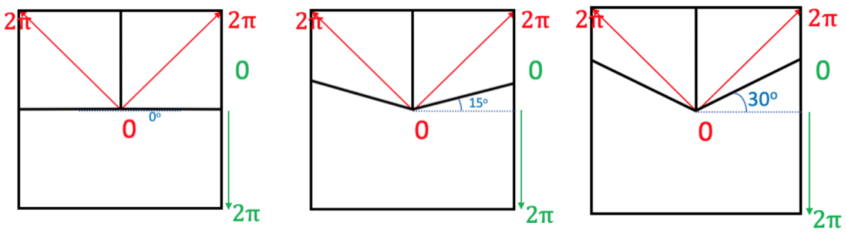

Figure 5.3: *Ingot phase masks used to reproduce the three different and extreme cases used in the test. Left: ingot seen from the farther sub-aperture with respect to the laser launcher, (**T0**). Center: ingot seen from a middle positioned sub-aperture, (**T15**). Right: ingot seen from the closest sub-aperture with respect to the laser launcher, (**T30**). See location in Figure 5.3*

The 2D phase screen approximation of the I-WFS has been tested at the LOOPS bench during two runs, with a different spatial resolution of the input turbulence. In the first run, we used the deformable mirror to apply a low resolution turbulence [65], while in the last run, we used a second SLM, positioned at an intermediate pupil plane, that is able to serve at the same time as a high-resolution deformable mirror and a turbulent phase screen generator [66], performing in parallel an End2End numerical tool of the I-WFS. A detailed discussion will be provided in the following sections.

5.2 Low resolution turbulence test

Using the optical layout shown in Figure 5.1, we tested all the combinations between the I-WFS phase masks and the source aspect ratios, as shown in table 6.2, and in addition we provided a comparison with the P-WFS phase mask. During the preliminary phase of the test, we realized that we could not reach the ratio between the major and minor axis more than 15 without bending the extended source, due to the limit of the modulation. Therefore , we decided to investigate the following

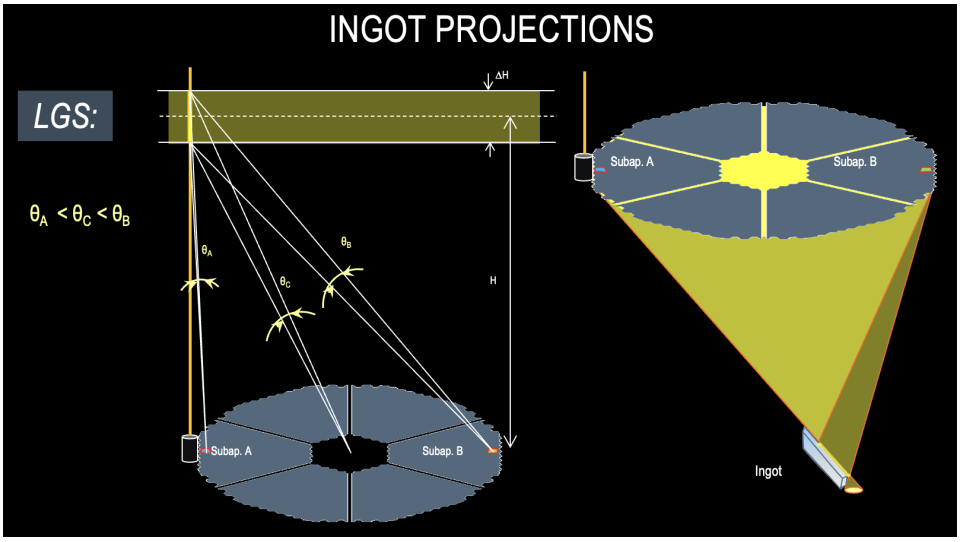

Figure 5.4: *I-WFS projection for 3 sup-aperture on the ELT telescope pupil*

source aspect ratios: 1:1, 1:7, and 1:15. In addition, we had to add a constraint to the disturbance applied, that was limited at a value of 0.4 microns.

We defined a robust alignment procedure between the source and the SLM (i.e. wavefront sensor phase mask) to be executed every time before starting the measurements. This algorithm uses the 4 faces P-WFS phase mask due to its geometrical symmetry, so that it can be used as an easy reference for the alignment. The alignment procedure steps are listed in the following:

- Using the diffraction-limited spot (without modulation) at the P-WFS phase mask, in order to equalize the flux in the 4 pupils.
- Perform the calibration procedure, generating interaction and reconstruction matrix
- Close the loop to obtain the best flat of the Deformable Mirror that must be applied before the following steps
- Center the modulation axis on the vertex of the P-WFS phase mask, minimizing:

$$abs(\sum S_x) + abs(\sum S_y) + abs(\sum S_{diag}), \tag{5.1}$$

where S_x is the signal along the X-direction, S_y is the signal along the Y-direction and S_{diag} is defined in Eq. 5.2

$$S_{diag} = abs\left(\frac{\sum(diagonal_1) - \sum(diagonal_2)}{total\,flux}\right), \tag{5.2}$$

This operation is necessary to match one of the modulation axes with the long edge of the I-WFS phase mask

- Offset the modulation along the X and Y axes, and check for the flux variation in the modulation camera (T-CAM)

- Rotate the source by $\pm 1/2°$, checking for the flux minimization using the Eq. 5.1
- Replace the P-WFS phase mask with the I-WFS phase mask, so that long axis of the Ingot matches with the modulation axis mentioned before. The P-WFS and I-WFS phase masks vertex should be identical.
- Apply an offset to the mask to obtain the correct flux ratio between the I-WFS pupils. Notice that for all the steps mentioned above, the source is not moving. All the movements are done at the level of the phase masks

Once we have defined the alignment procedure, we performed the test for all the combination of I-WFS phase masks vs the source aspect ratios. The disturbance is made combining the first 65 Zernike modes on the Deformable Mirror where the modal amplitude is fixed at $\sim$ 20nm.

Figure 5.5, shows the RMS Wavefront Error measured from the SH camera for the different combinations of the I-WFS phase masks and elongations, during the closure of the loop. Solid lines are for I-WFS closed loop data, while dashed lines are for P-WFS closed loop data comparison. Note that for all the configurations the turbulence applied is frozen in time. We also report in table 5.1 the average of

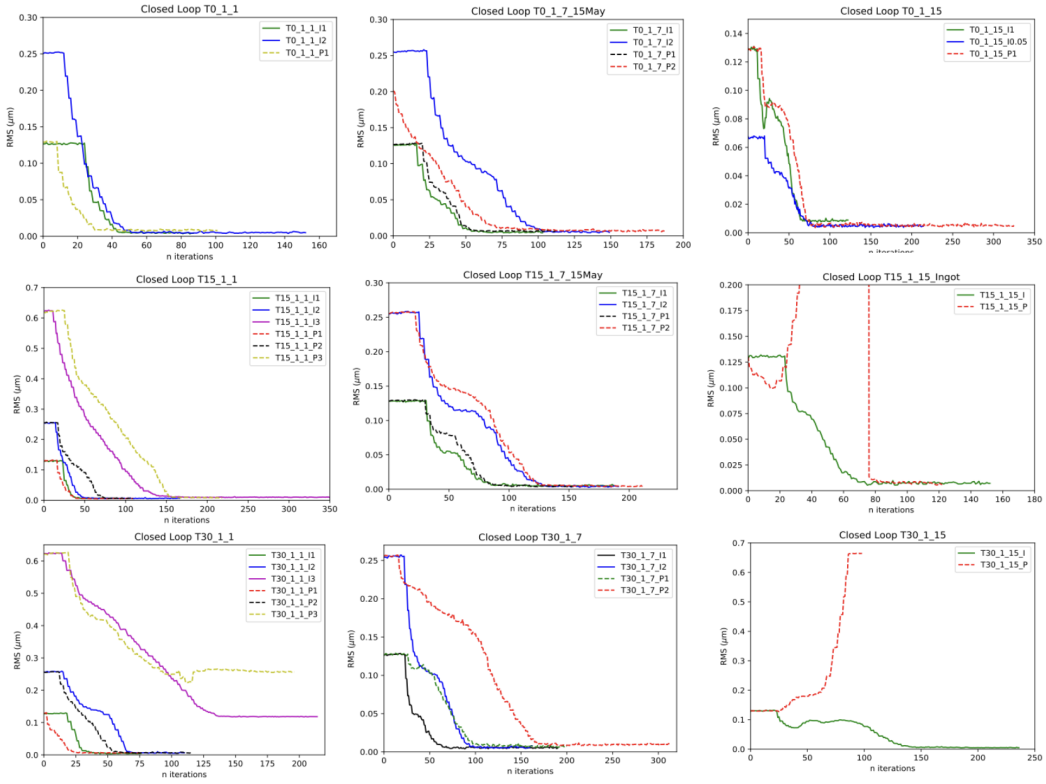

Figure 5.5: *WFE measured from the SH camera for the different combinations of the I-WFS phase masks and elongations. From top to bottom: T0, T15, and T30. From left to right: source aspect ratio 1:1, 1:7, 1:15. Solid lines are for I-WFS closed loop data, while dashed lines are for P-WFS closed loop data comparison. All the cases are for frozen turbulence.*

the WFE measured on the SH camera after closing the loop in the case of 130 nm

RMS. In addition, we indicate between () the iteration number that we consider as the limit for closing the loop. All the values are shown in nanometers.

	T0	T15	T30
1:1	4.7 (45)	6.3 (39)	4.7 (37)
1:7	5.3 (54)	5.3 (87)	5.6 (68)
1:15	8.5 (63)	7.4 (73)	5.8 (149)

Table 5.1: *Average WFE in microns, after closing the loop for the different configurations. In brackets, we indicate the first iteration after that we considered the loop closed*

The goal of these tests was to investigate the behaviour of the I-WFS in a quasi-real AO system. As a second step, we tested the closed-loop behavior of the ingot with a dynamic turbulence. Due to limited available time on the LOOPS bench, we had the opportunity to investigate only three configurations of phase masks/source aspect ratios, which are: T0/1:1, T15/1:7, and T30/1:15. The results of this analysis appear in Figure 5.6 in terms of measured WFE, and are reported in table 5.2. Note that all values are in nanometers.

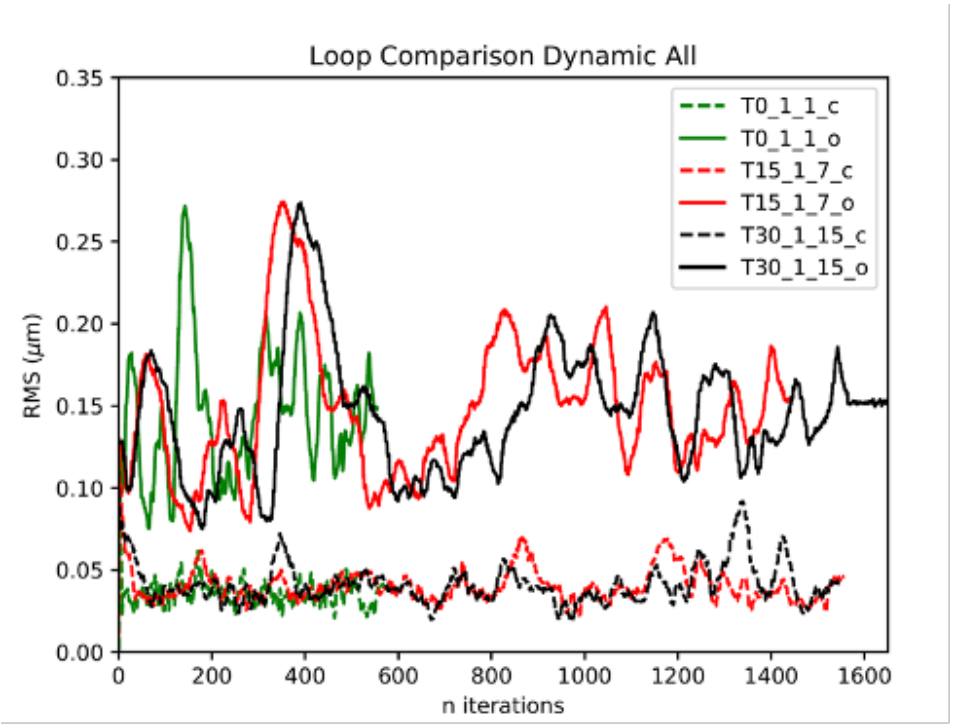

Figure 5.6: *WFE measured from the SH camera for three combinations of I-WFS phase masks and source aspect ratio. T0/1:1, T15/1:7, and T30/1:15. Solid lines are for open loop while dashed lines are for closed loop. The plots refer to the loops with dynamic disturbance, but still with a WF built with a combination of the first 65 Zernikes modes.*

T0 + 1:1	T15 + 1:7	T30 + 1:15
36 (22)	41 (34)	4.1 (63)

Table 5.2: *Average WFE after closing the loop for some configurations considering a dynamic disturbance. The values are shown in microns. In brackets we indicate the first iteration after that we considered the loop closed*

5.3 High resolution turbulence test

Between the first and second run the LOOPS bench facility was upgraded with a second SLM placed in a pupil plane, as shown in Figure 5.7. This new device is able to serve simultaneously as a high-resolution deformable mirror and a turbulent phase screen generator, with a much higher resolution with respect to the previous configuration using the deformable mirror. The spatial resolution of the input phase increased from 65 Zernike modes to the 230 Karhunen-Loeve modes used for this test.

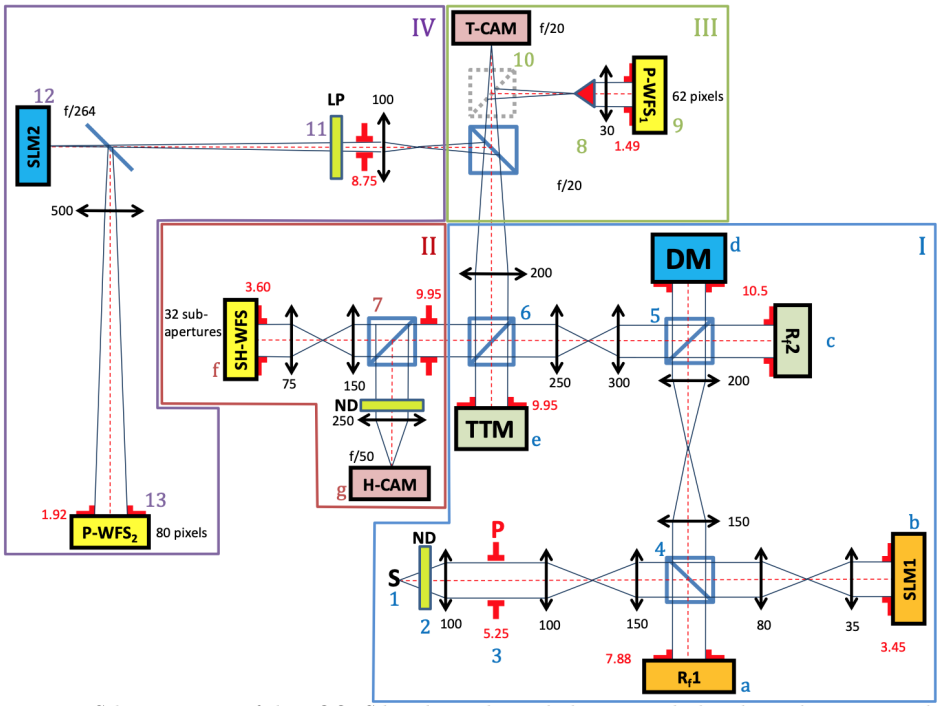

Figure 5.7: *Optical design of the upgraded LOOPS test bench*

We performed a test of the I-WFS for several combinations of source aspect ratios and wavefront sensor phase masks. The aim of this test was to investigate the behavior of Ingot phase masks in combination with the source aspect ratios. Unfortunately, due to severe instabilities of the setup we didn't manage to close the loop for all the configurations, not even for the P-WFS phase masks. We report in the following, the results from the only combination of phase mask and source aspect ratio, for which we successfully close the loop.This configuration is the 1:7 source aspect ratio with the T15 mask. We also performed a comparison with the P-WFS case by making the SLM2 produce a four-faces phase mask. The SLM1 produces a

disturbance with a resolution of 320 pixels in the pupil diameter.

Here, we report the characteristics of the input turbulence that has been created using the OOMAO [67] code:

- $r_0 = 0.9m$
- Equivalent Telescope Diameter = 8m
- Wind speed = 10 m/s
- Bandwidth = 200Hz
- Seeing = 0.15”
- Calibration and correction made with 230 KL modes
- Pupil dimension = 318x318 px
- Turbulence history, length = 1000 frames

Figure 5.8 is shows, for the same frame, the shape of the input turbulence on the left, and the corresponding correction applied by the SLM on the right.

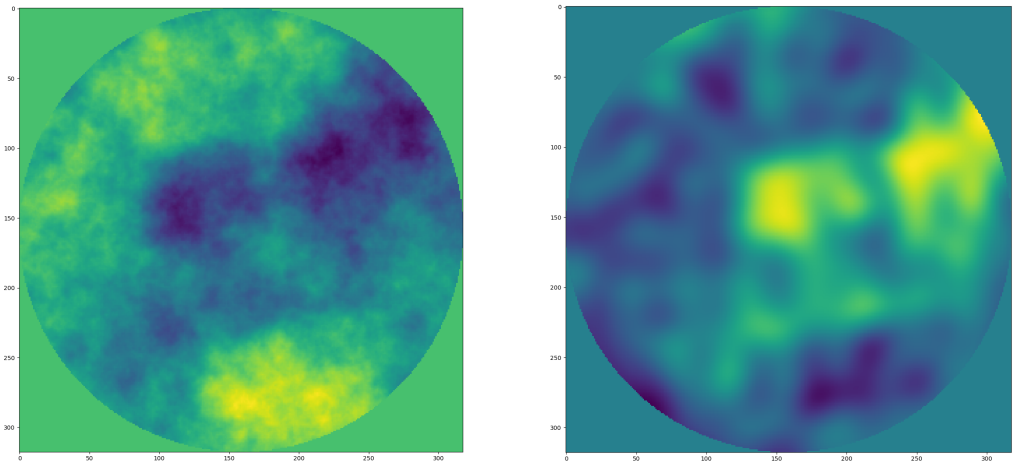

Figure 5.8: *The two phase maps freeze an instant of the loop evolution. On the left the phase map of the input turbulence commanded to the SLM. On the right the complementary correction applied by the SLM. Both the pictures are shown in term of pixels.*

Note that, to make the calibration and calculate the interaction matrix, we used the signals relation defined in the previous chapter, and reminded in equation 5.3.

$$\begin{aligned} S_x &= \frac{B-C}{A+B+C} - \frac{B_{ref}-C_{ref}}{A_{ref}+B_{ref}+C_{ref}}, \\ S_y &= \frac{A}{A+B+C} - \frac{A_{ref}}{A_{ref}+B_{ref}+C_{ref}}. \end{aligned} \tag{5.3}$$

According to the turbulence parameters, in the following we report the results for the configuration of the T15 phase mask for the 1:7 source aspect ratio for three cases plus the P-WFS:

case 1 12.5% of the total flux (1/8th) in the transmitted pupil, using the signals calculated following eq. 5.3

case 2 12.5% of the total flux (1/8th) in the transmitted pupil, using the fluxes measured from the pupils as signals

case 3 25% of the total flux (2/8th) in the transmitted pupil, using the signals calculated following eq. 5.3

case 4 P-WFS using the fluxes measured from the pupils

Figure (5.9) shows the standard deviation of the wavefront error map during the iterations for open and closed loop for the cases 1, 3, and 4. As the plot in Figure 5.9

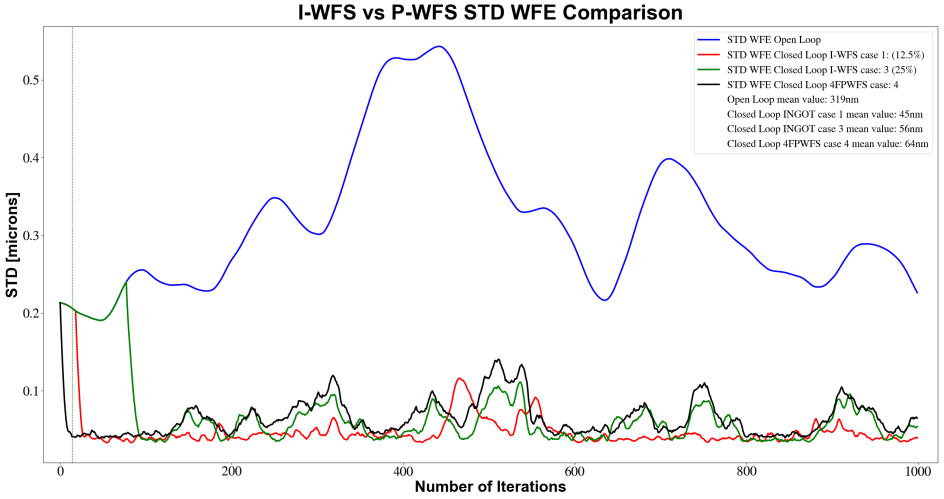

Figure 5.9: *standard deviation wavefront Errors Open-Closed loop comparison between I-WFS cases (1-3) and P-WFS.*

shows, both I-WFS and P-WFS well perform in the closed-loop scenario. Apparently the two I-WFS curves superimpose on the open-loop line more than the P-WFS does. This effect is due to some delay in the activation of the loop. If we look at the residuals mean values of the three cases, we can easily note that the I-WFS shows a smaller amplitude of residual aberrations (i.e., a lower mean value), even if the difference with respect to the 4 faces pyramid is negligible.

Moreover, we report a comparison between "case 1" and "case 2", as shown in Figure 5.10. For both of them, the flux in the transmitted pupil is equal to the 12.5% of the total. Here, we can notice from the plot that "case 2" shows a residual mean value lower than "case 1". This very preliminary result could suggest to us to consider, as alternative to the eq. 5.3, the possibility to use as signals the normalized fluxes of the three pupils.

5.3.1 Simulation Tool description and results comparison

In parallel, we developed an end to end numerical simulation tool in which we modelled the I-WFS similarly to the P-WFS [68], as a combination of Foucault knife-edge sensors. We simplified the computation through a far-field configuration involving only a sequence of Fourier transforms. We have represented the I-WFS faces as a phase-mask that splits (tilting) the light. The image o the I-WFS focal plane is

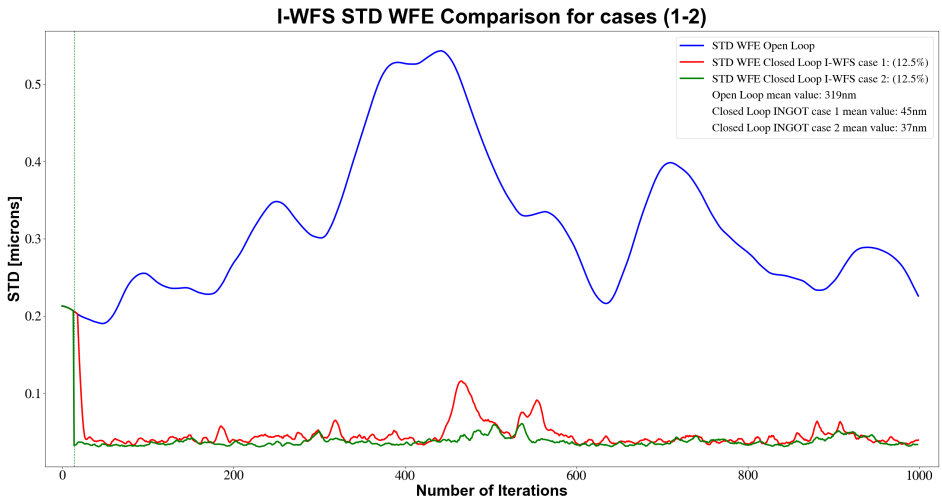

Figure 5.10: *Standard Deviation Wavefront Errors Open-Closed loop comparison between cases (1-2).*

simulated through the Fourier transform of the complex array in output from the previous step. The P-WFS is typically modulated; however here we do not consider modulation because of the computational workload and especially because a similar algorithm is already exploited to generate the extension of the LGS source. The two effects, modulation and extension of the reference source, are almost equivalent: the extended source can be modelled as an elaborated form of modulation. We approximated the elongated spot to be two-dimensional, as it was also simulated on the LOOPS bench, and divided it into point-like sources, to cover the angular extension observed from the ground.

We adapted the already available structure of the MAO code [69, 70] to build the algorithm for the closed-loop system. The module is approximated into its main components: input turbulence, wavefront sensor, deformable mirror, and control loop. For the input turbulence, we used two options: the turbulence is injected using the deformable mirror, or the phase is generated by an external input (e.g. moving phase screen or spatial light modulator). In the numerical simulation, the phase is ultimately a moving random phase screen or a combination of mirror modes with a dynamics following Kolmogorov[71, 72] or Von Karman[73] power spectrum. The deformable mirror can be computed as a linear combination of the vectors composing a Zernike or actuators influence function modal base. The control loop is a pure integrator with user-defined frequency expressed in frame delay and bandwidth modulated by a gain value. The comparison of the laboratory results with the outcomes of the simulation analysis provides a better insight into the I-WFS behaviour in the closed-loop.

In Figure 5.11 we present the results in terms of wavefront error standard deviation as measured for each iteration of the loop. We provide at first the same configurations used in the laboratory setup, (section 5.3), "case 1", "case 2" and "case 3", and in Figure 5.12 similar configurations but using a different ratio of the light split between transmitted and reflected pupils. These simulations were not converging as expected, most probably because of the extra noise introduced by diffracted light on the refracted pupil.
In order to counterbalance this effect we decided to change the illumination ratio,

forcing more light on the transmitted pupil and reducing in this way the relative intensity of the diffracted light.
The cases shown in Figure 5.12 correspond to the following configurations:

case 1b 50% of the total flux in the transmitted pupil, using the signals calculated following eq. 5.3.

case 2b 50% of the total flux in the transmitted pupil, using the fluxes measured from the pupils used as signals.

case 5 a functional case using a point source, no modulation, 50% of the total flux in the transmitted pupil, using the fluxes measured from the pupils.

Table 5.3: *Input parameters used for the numerical simulations.*

Pupil Geometry	D	wavelength	FFT resolution	FoV
Full Circular	8m or 318px	$\lambda = 660nm$	$4\lambda/D$	5arcsec

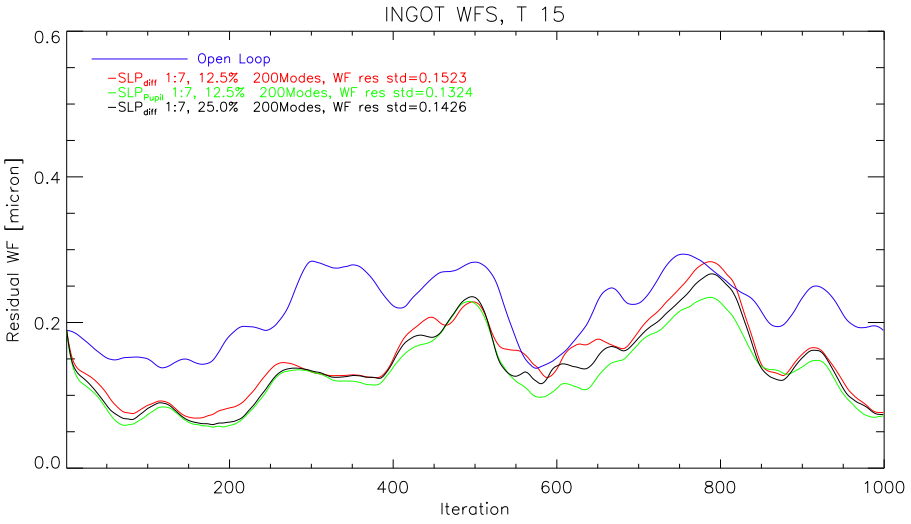

Figure 5.11: *The plots show the closed loop residual phase standard deviation of the configurations corresponding to "case 1", "case 2" and "case 3" (in blue the open loop). For a better readability: in red using the slope computation of eq. 5.3 and 1:8 pupil illumination ratio, in green using normalized pupils instead of slopes, and finally in black the eq. 5.3 slopes and ratio 1:4.*

The LOOPS bench and numerical simulations provide insight about the behavior of I-WFS in closed loop. A crucial point is the linearity of I-WFS response that we are addressing. Strictly related to this point is the optimal illumination of the transmitted pupil versus the reflected two: both simulation and experiment show the need to close the loop with a non-zero reference slope vector. However, large amplitudes of the slope vector may introduce non-linearity issues (as the case of the P-WFS).

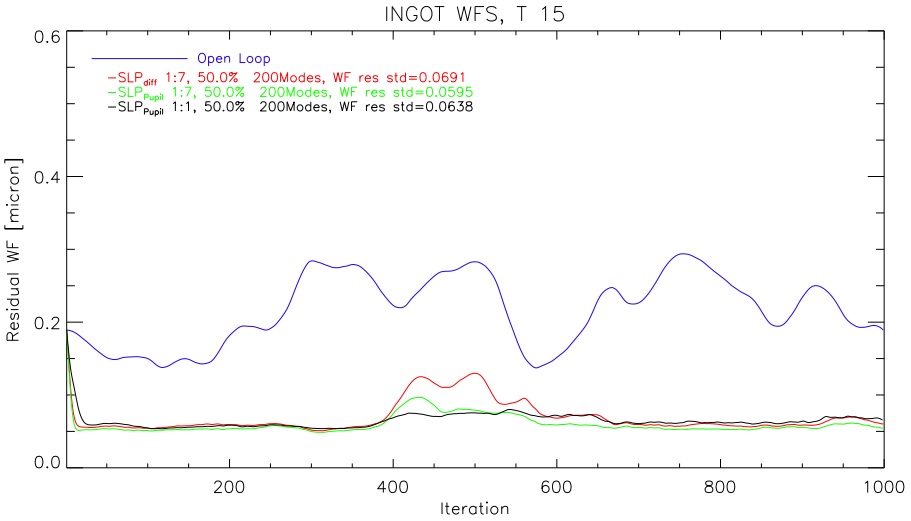

Figure 5.12: *Referring to the "case 1b", "case 2b" and "case 5". In short: in red the case with slope computation of eq. 5.3, in green using normalized pupils, in black the functional test using a point-like source.*

The laboratory tests indicate that the I-WFS performs slightly better than the P-WFS having an extended reference source. Or, being less optimistic, the performance is comparable.

The numerical simulation provided similar values for the standard deviation of the residual phase to the LOOPS experiment (both in the range of 40-60nm). In the simulations, we excluded the tip-tilt both from the input and the controlled modes: in the case of the laboratory we can assume that the contribution of the very low order modes is negligible, since the input aberration is a pure atmospheric disturbance that shows a slowly evolving bent of the wavefront, and also vibration-free. Theoretically, we expect, using the parameters of the turbulence statistics, the number of modes used for correction and the bandwidth of the system, a noise-free correction residual with standard deviation of 37nm for the LOOPS setup and 39nm for the simulation. Both values are in good agreement with the measured values (i.e., 45nm and 60nm), which include also other error sources related to the bench realization and the I-WFS noise propagation. For a cross-check, the values in open loop are respectively 650nm (assuming pure Kolmogorov turbulence) and 260nm in the tip-tilt-free case: the turbulence statistics in open loop fit well with a turbulence spectrum with a finite outer scale.

Chapter 6

The I-WFS at the INAF laboratory test bench

In order to investigate is the behavior of the I-WFS not only from a simulation point of view, at the Observatory of Padua - INAF, we realized a test-bench that aims to reproduce the ELT main geometrical characteristics. We used simulations and laboratory data to compare, learn, and define a robust, entirely automatized alignment procedure using the optical feedback provided by the I-WFS. In addition, we also performed tests to understand the I-WFS response when it comes to characterize known aberrations using a deformable lens positioned in the pupil plane.

6.1 The I-WFS test-bench optical design

The test-bench setup shown in Figure 6.1 is composed of off-the-shelf components. It is specifically designed to simulate the imaging of the LGS source onto the I-WFS prism and to produce an image of the three pupils on a dedicated camera with the proper sampling.

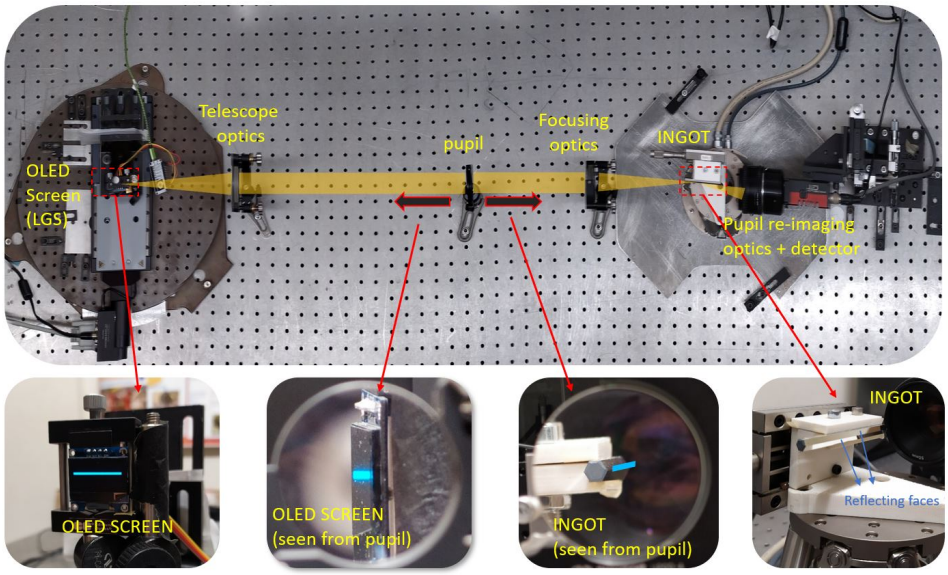

Figure 6.1: *Top view of the optical bench setup used to test the ingot alignment procedure.*

The design aims to be as much as possible similar to the ELT including:

- The ratio between the separation of the Laser Launcher Telescope from the optical axis and the entrance pupil diameter
- The physical size of the image on the I-WFS prism
- The telecentric image space (on the I-WFS prism)
- The aspect ratio of the LGS (spot elongation to FWHM ratio)

The Optical layout is a 1:1 re-imaging relay, composed of:

- An OLED screen programmable with an Arduino to reproduce the LGS. The screen, an SSD1306 monochrome OLED display, has a format of 128x64 pixels with 170 μm pixel size. The advantage of this a device is that it has almost no background noise emission of black pixels, which is commonly present in other display technologies.
- An achromatic doublet with focal length f=200 mm that collimates the light from the LGS source, and another one that refocuses the light onto the I-WFS prism.
- A diaphragm located between the lenses that acts as the aperture stop/pupil of the system with a clear aperture of 25 mm. It is placed such that the system is telecentric in the image space, i.e. the stop is at the focus of the camera doublet.
- A pupil re-imager optics, consisting of a f=50 mm wide-aperture photographic objective.
- The I-WFS based on an hexagonal light pipe, generally used for beam homogenisation, whose external faces have been aluminized to obtain a reflective roof with an apex angle of 120°. Notice that this angle is the same one required at the ELT to achieve the proper separation of the reflected pupils.
- The camera, a Prosilica GT3300 from Allied Vision. The detector is an 8 Megapixel CCD sensor with 5.5 μm pixel size. We use a 4x4 binning to sample the pupil diameter with $\approx$ 130 pxl.

The I-WFS prism is mounted on a H-811 Hexapod from Physik Instrumente. This device allows precision movements in all six degrees of freedom of the I-WFS.

6.2 I-WFS Ray-Tracing Simulator

In order to have a clear view of the I-WFS design parameters and get familiar with the signals distribution, we have built a setup simulator using the ray-tracing optical design software *Zemax OpicStudio*. The optical design of the bench shown in Figure 6.2.

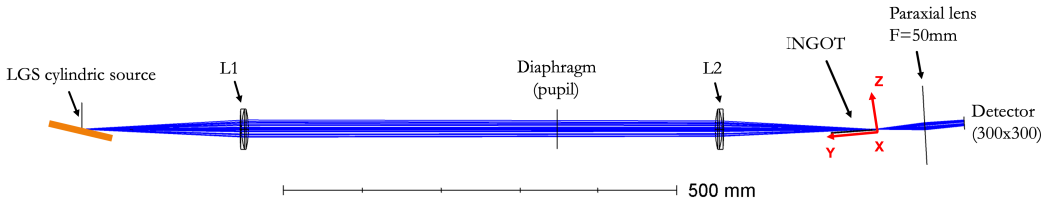

Figure 6.2: *Optical Design of the I-WFS test bench*

The Ingot prism position is defined by the reference coordinate system shown in Figure 6.3. The coordinate system is given by a rotation of $-94°$ on X-axis and a shift of $-14mm$ on Y-axis with respect to the light path reference system.

The origin of the coordinates system is placed at the beginning of the Ingot prism

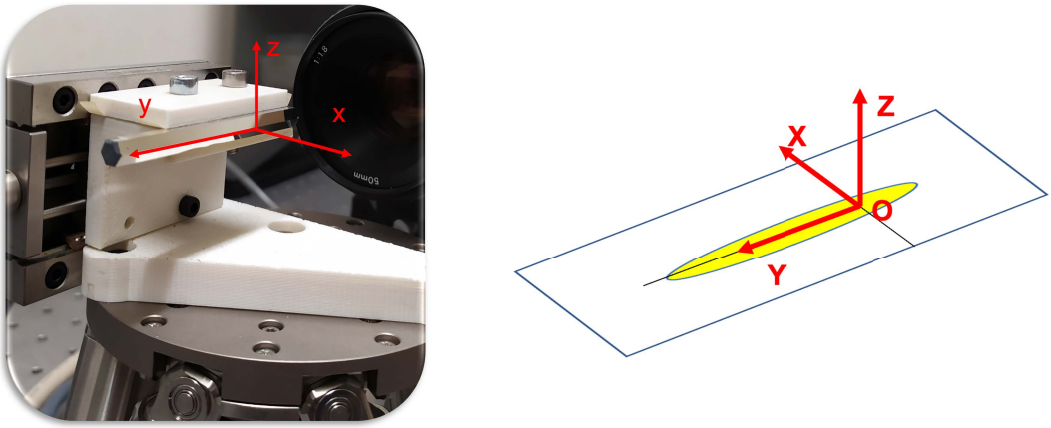

Figure 6.3: *Coordinate system of the Ingot prism*

facing the camera; the Y-axis coincides with the edge between the reflective faces of the Ingot with positive pointing towards the telescope. The Z-axis points in the vertical direction with respect to the bench. The X-axis is chosen to form a right-handed coordinate system. Finally the pivot point for rotations is set at the origin of the coordinates system.

In order to efficiently simulate the source and get a reasonable statistics in terms of rays/pixel in the image of the pupils, we developed a Zemax custom dynamic-link library source able to generate rays from a rectangular surface (or a cylindrical volume) and to aim them towards the entrance pupil of the system. The rays are traced through the system and recorded by a detector having ≈ 130 px over the pupil diameter. The use of a smaller sampling with respect to the real detector, not only reduces the simulation time, but also keeps a reasonably low statistical noise. The source used in the simulations that we will present below is a rectangular source, 0.85 mm wide and 21.76 mm long, that approximately matches the average angular elongation expected on-sky and is compatible with the OLED screen characteristics.

The pupil illumination pattern for the aligned condition, in which the three pupils are equally spaced, appears in the left panel of Figure 6.4, where the transmitted pupil is the one at the top while the reflected pupils are the ones at the bottom.

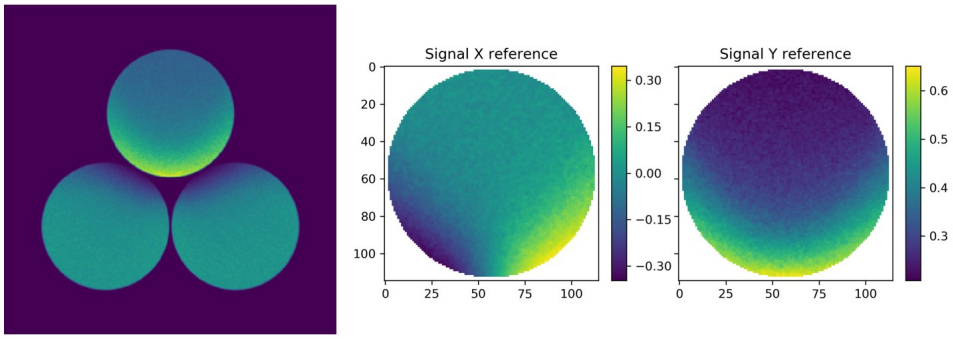

Figure 6.4: *Left: Pupil illumination for the aligned condition. Right: Signals S_x and S_y are calculated from the pupils using Equation (5.3).*

In the central part of the image, the uneven illumination at the pupils' edges is a specific feature of the ingot and is due to its geometry. One may note the effect of uneven illumination in the signals (see right panel of Figure 6.4), which are not flat as in the case of a modulated pyramid wavefront sensor. Diffraction effects are not accounted for in the simulations, since they are expected to be small due to the LGS's extended nature. Compared with the diffraction limited size of a 40-meter diameter telescope, in fact, the FWHM (short side) of the LGS is larger than $100\lambda/D$.

6.3 Pupil Analysis Procedure

We developed a fully automatic python procedure that, starting from the pupil frame, (left panel of Figure 6.4) is able to perform autonomously the following actions:

- Using a Canny-edge algorithm [74], the code is able to identify the 3 pupils position, in order to fit them and define the radii at the coordinates of the centers (in pixels), as shown in Figure 6.5

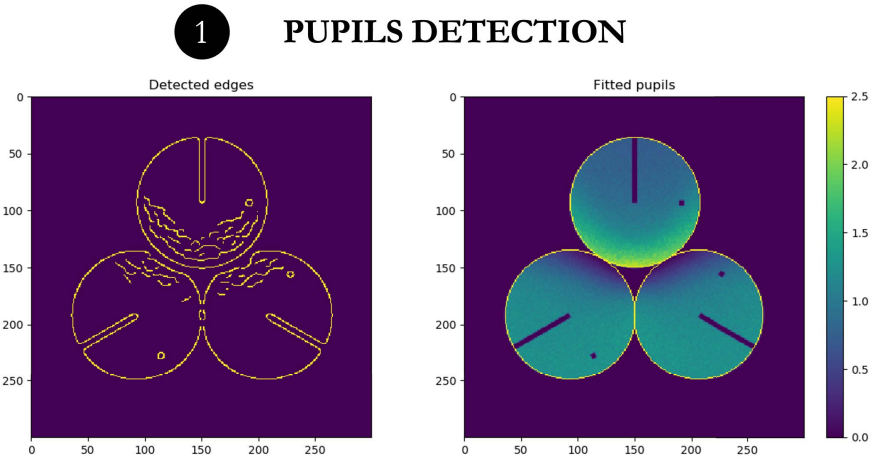

Figure 6.5: *Left: Detection of the three pupils using the Canny-edge algorithm. Right: Best fit of the circular external edge*

- Extract the three pupils from the image, perform a rotation and flip to compensate the effects induced by the reflection from the Ingot prism, as shown in Figure 6.6

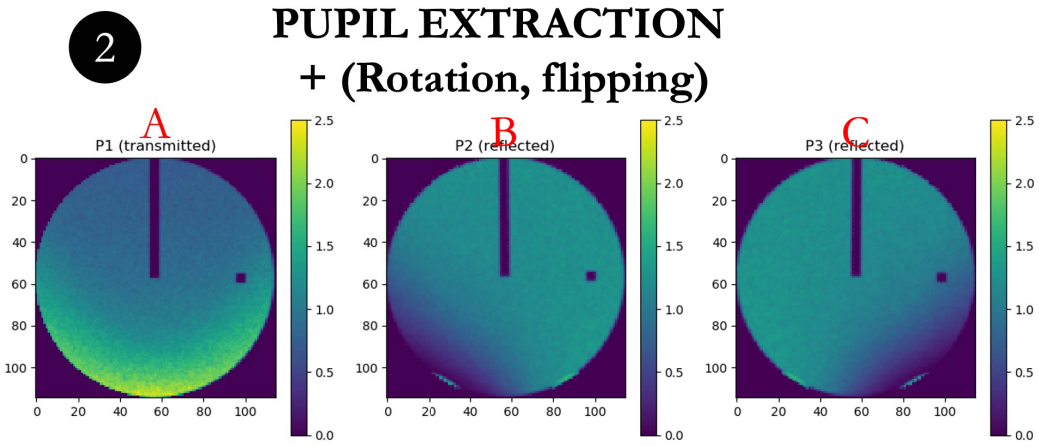

Figure 6.6: *Left: Extraction of the pupils. Rotation and Flipping for the two reflected pupils*

- Once the pupils are localized and co-aligned, they are used to calculate the signals as indicated in equation (5.3) and the result obtained appear in Figure 6.7

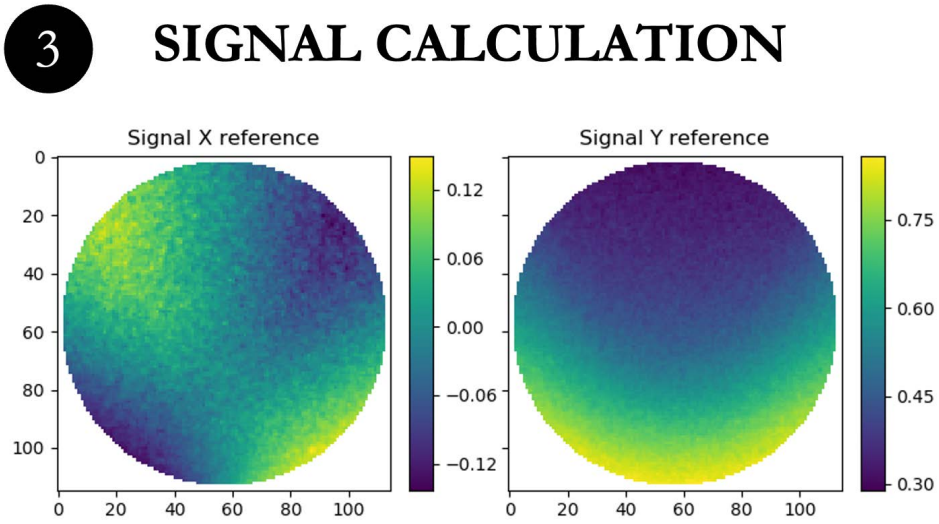

Figure 6.7: *Signals S_x and S_y*

Note that in Figures 6.5 and 6.6, we added a line and a small square in order to highlight the orientation and to show how pupils B-C are rotated and flipped due to the reflection from the Ingot prism.

At this point, we are now able to investigate the effects of misalignment of the ingot prism with respect to the LGS. We performed a sensitivity analysis by moving

the ingot along each degree of freedom, one at a time, and we identified the following observables as gauge of the alignment of the I-WFS:

- Distance between the pupils
- Integrated flux within each pupil
- The variation produced on the signals S_x and S_y

Note that, in the aligned condition, the edge of the Ingot prism is placed along the axis of symmetry of the LGS image, the three pupils are equidistant from each other, and both reflected pupils have the same integrated flux. The amount of light in the transmitted pupil is still a free parameter, that for convenience we set equal to the light on the reflected pupils, in order to have $1/3^{rd}$ of the total flux in each pupil, thereby maximizing the dynamic range available on the detector.

The results of the sensitivity analysis appear in the Table 6.1. We can notice that the rotations affect mainly the positions of the pupils, while the decenter affects only the flux, and thus also the signals. In the table, we distinguish between reflected and transmitted pupils and to give an idea of the magnitude of the change we use $(+\ +)$ for stronger variations and $(+)$ for weaker variations. Note that the decenter Y has a weaker effect with respect to the other degrees of freedom, because it corresponds to the direction of the elongation, which, as expected, reduces the sensitivity to movements in general. As a reminder, Figure 6.8, A represents the transmitted pupil, while B and C are the two reflected pupils, left and right respectively.

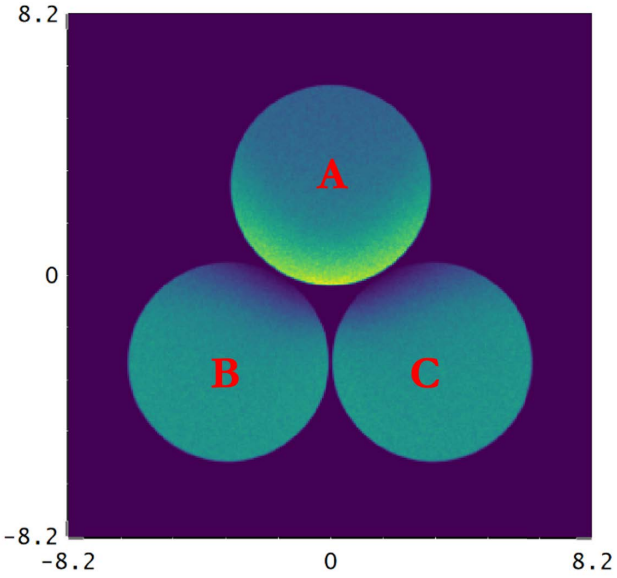

Figure 6.8: *Pupils*

Figures 6.9 and 6.10 report the signals produced by each degree of freedom from the Zemax simulations and the laboratory verification, respectively. Note that, even if we are only able to compare qualitatively the results, (the simulated amplitudes are different from the lab measurements), it is more than clear that the simulations

Degree of Freedom	A Flux	B & C Flux	Separation A-B or A-C	Separation B-C
Decenter X	+	++		
Decenter Y	+	+		
Decenter Z	++	++		
Tilt around X			++	++
Tilt around Y			++	
Tilt around Z		++	++	+

Table 6.1: *Degrees of freedom and the corresponding observables*

and lab verification have a reasonable agreement. These results are of fundamental importance for the alignment procedure.

Note that tilting around the Y-axis has a minor effect on the signal. This is due to the fact, that the 3D image of an LGS has, to a good approximation, a cylindrical symmetry, and therefore a rotation around the Y-axis does not affect the alignment, as the decenter along Y is very low sensible due to the LGS elongation.

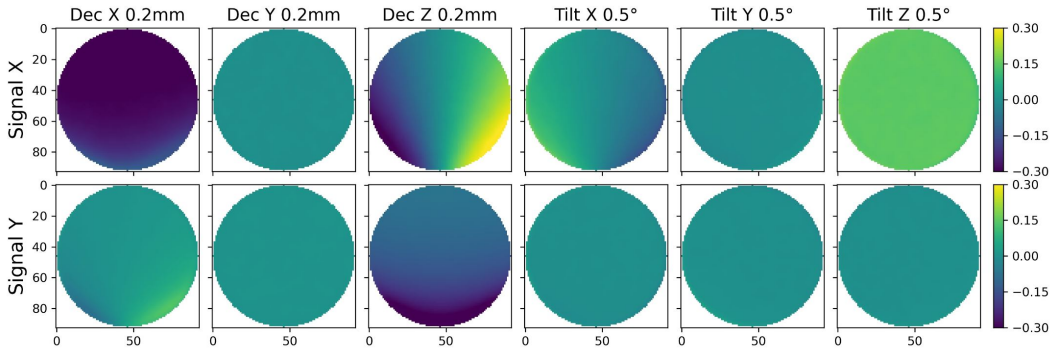

Figure 6.9: *Variation of signal produced by each degree of freedom. Results from simulations.*

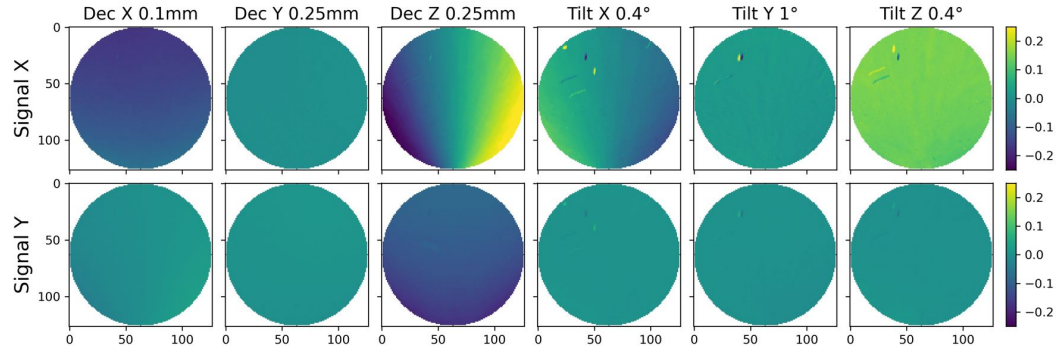

Figure 6.10: *Variation of signal produced by each degree of freedom. Results from lab measurements.*

The analysis performed above is the key to build a powerful alignment procedure of the I-WFS with respect to the LGS source. We developed a procedure that is composed of two levels: The first is related only to the position of the pupils and the distribution of light (in the sense of integrated flux within each pupil). The aim

here is to align the I-WFS to the optical axis of the telescope and the fore-optics. The second level takes into account the movements of the LGS on sky, which, from a practical point of view, represent a movement of its image on the I-WFS, producing a variation of the flux and signals. Note that movement of the source on-sky does not produce a change in the position of the pupils, because the latter depends solely on the relative alignment between the ingot and telescope. Thus, from an operational point of view, the first alignment is related to the alignment of the ingot WFS to the telescope (first alignment and any other re-alignment necessary to compensate flexures or other movements of the optics), while the second alignment is related to the compensation of LGS position (focus variation or jitters of the LGS). The procedure and tests presented below are ideal because they do not consider any mid-high order aberration. A check of the convergence of the procedure in presence of other aberrations is left for the future.

6.4 The Alignment to the Telescope Procedure

Based on to the results of the sensitivity analysis described in the previous section, we developed a procedure for the first alignment of the Ingot prism to the optical axis. The procedure consist of the following steps:

1. Adjust tilt Y and tilt Z of the ingot prism to achieve the same separation between transmitted and reflected pupils, having at the same time the reflected pupils aligned horizontally on the detector.
2. Adjust tilt X to have a separation of a few pixels between the pupils.
3. Move decenter X to equalize the flux in the reflected pupils.
4. Move decenter Z to achieve a flat S_x in the top half part of the pupil (in the bottom part of the pupil, the signal is not flat as shown in Figure 6.4).
5. Move decenter Y to have the same flux in all the 3 pupils.

These steps, have been used to perform a rough preliminary alignment of the Ingot prism with respect to the optical axis. After successfully identifying this starting position, we developed a fully automatic alignment procedure that aims to speed up the tests and to perform a statistical analysis of the convergence. This has been done by remotely controlling the Hexapod and the camera, through a Python script that was specifically written to automatize the calculation of pupils positions, light distribution and signals, in order to allow reconstruction and compensation processes.

To perform the procedure, we have considered the 6 observables that we have identified in the previous section. They are linearly independent, and are listed below:

- The difference between the flux in the (B-C) pupils, normalized to the total flux of the pupils, as shown in Figure 6.11

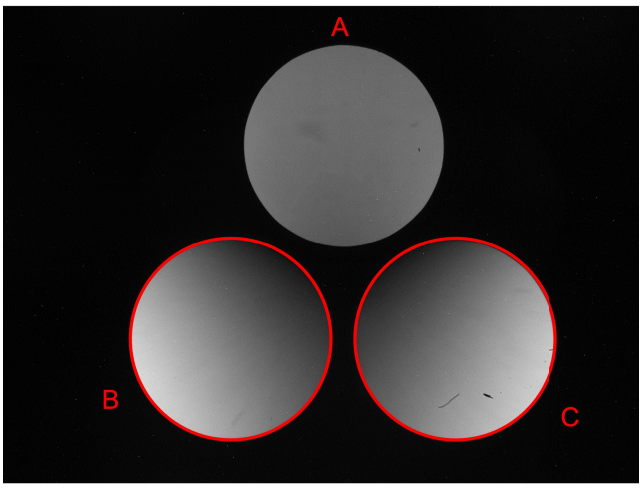

Figure 6.11

- The flux of the A-(B+C) pupils, normalized to the total flux of the pupils, as shown in Figure 6.12

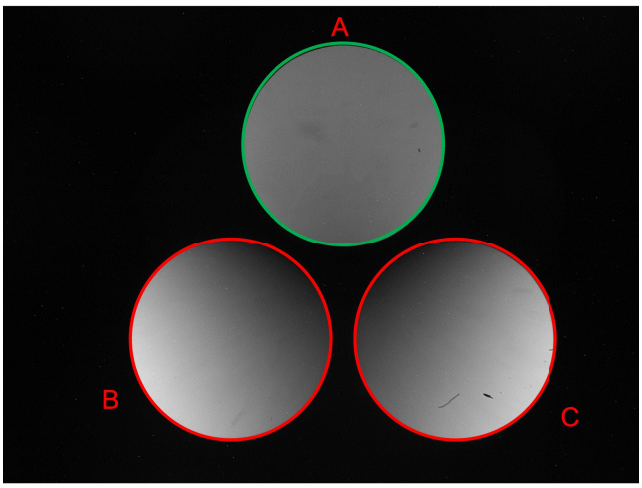

Figure 6.12

- The distance between the centers of the A & B pupils, as shown in Figure 6.13

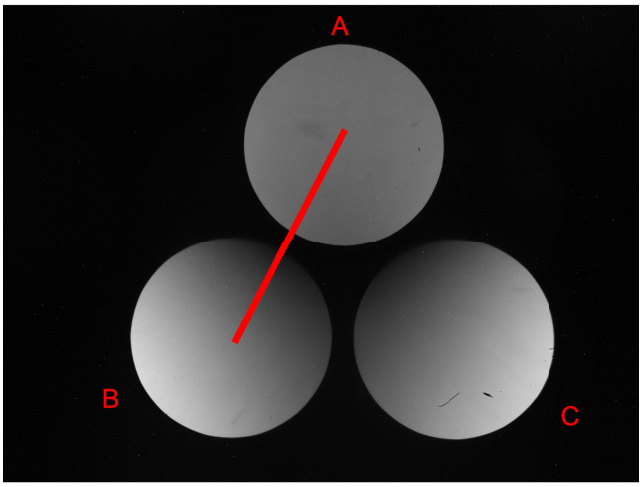

Figure 6.13

- The distance between the centers of the A & C pupils, as shown in Figure 6.14

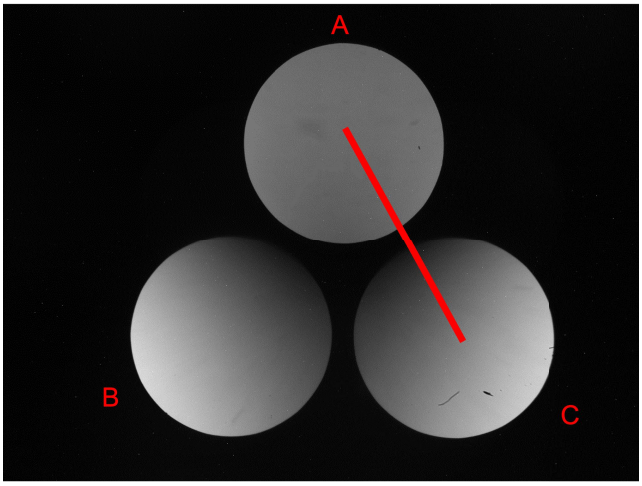

Figure 6.14

- The position of the centers of the B & C pupils with respect to the Y-axis, as shown in Figure 6.15

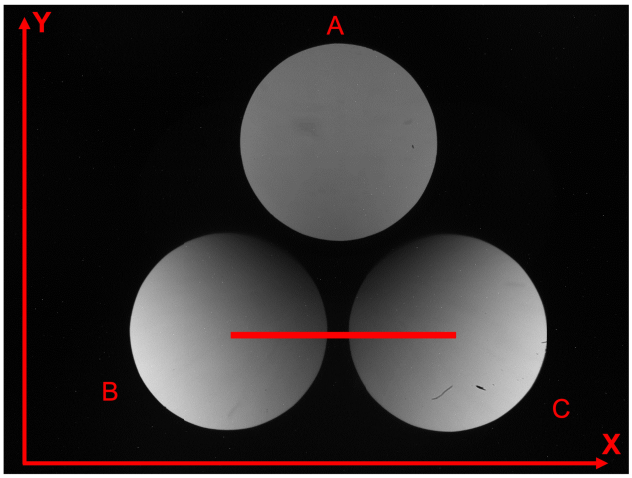

Figure 6.15

- The difference of the average of S_x in two regions that correspond to the top-left (1) and top-right (2), as shown in Figure 6.16. Note that the size is choosen to not reach the half of the pupil.

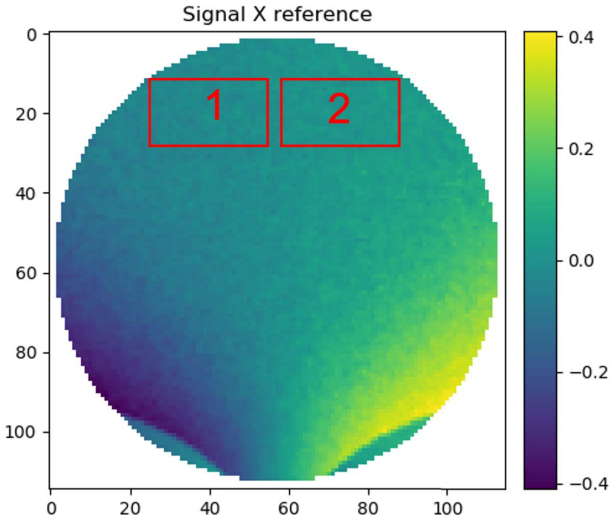

Figure 6.16

Observables	Target Values
Flux (B-C)/Flux (A+B+C)	0
Flux (B+C-A)/Flux (A+B+C)	2/3
Distance A-B	277 pxl
Distance A-C	277 pxl
Position B-C	0
Avg Sx[1]-Avg Sx[2]	0

Table 6.2: *Observables used to build the alignment procedure, together with the target values that our system should ideally reach*

In order to let our system know that the alignment position is reached, we have defined a target value for each observable listed above. Table 6.2 lists the observables and target values.

The alignment procedure is based on a linear approximation approach similar to that commonly used in AO closed-loop theory. We calculated an Interaction and Control matrix (IM & CM), as is usually done for DMs. In our context, IM and CM don't take into account the Zernike modes of the DM, but rather the variation of the 6 observables due to misalignments of the Ingot prism with respect to the optical axis of the system. The calculation of the IM and CM is also automatized through a dedicated python routine, which use the first rough alignment as a starting point for the calibration of the IM, as shown in Figure 6.17. Before entering into the details

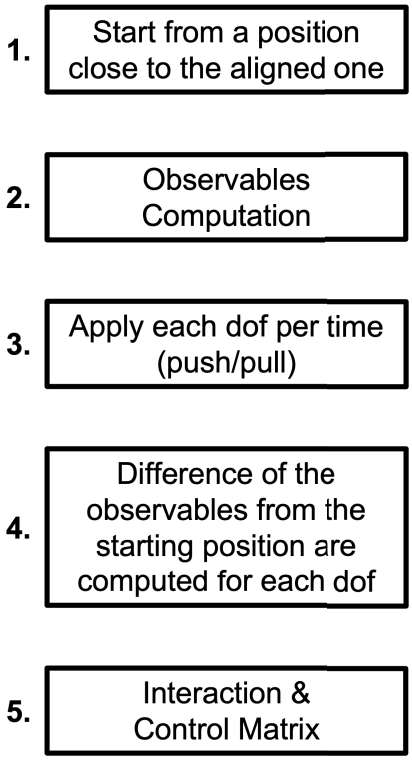

Figure 6.17: *Calibration Process flow*

of the calibration procedure, it is important to remember that the hexapod stage on which the Ingot prism is positioned is able to move in the 6 degrees of freedom, defining, in fact, an array of 6 coordinates.

Let's now make a detailed description of the calibration procedure mentioned above:

- 1. Start from an hexapod (i.e. Ingot prism) position that should be close to the position that we have identified as the aligned one. This makes the procedure faster from a computational point of view.
- 2. Perform the computation of the 6 observables defined in table 6.2.
- 3. Define a set of 6 coordinates to be used as misalignments to displace the hexapod stage as is done with DM. We apply each degree of freedom (dof) at the time, as push and pull manner, performing each time the observables computation. After this process, we expect to have for each dof applied 2 sets of 6 observables: One for the push (positive dof) and one for the pull (negative dof).
- 4. Calculate the difference for each dof between the observables computed in step 3, with respect to that computed in step 2
- 5. Build the Interaction Matrix starting from the results of point 4. Obtaining 2 IM: one coming from the push, and one from the pull. These two IMs will be combined into a single one that corresponds to the mean of them. Thereafter, it will be pseudo-inverted in order to produce the Control Matrix, as shown in Figure 6.19.

In order to have a more clear understanding of how the IM is structured, we report an example in Figure 6.18, where rows contain the 6 dof, while the columns hold the 6 obervables. In Figure 6.19, are shown the IMs produced for the push/pull

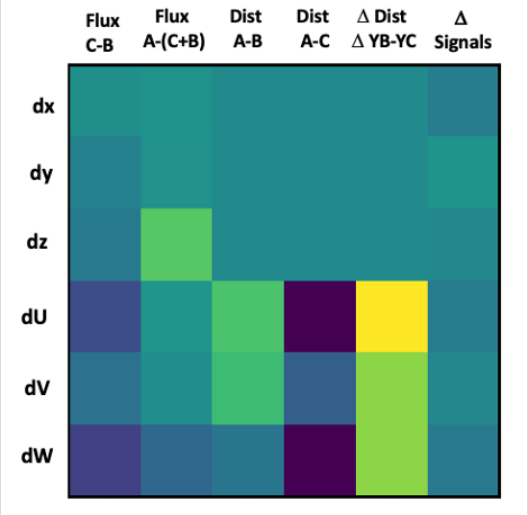

Figure 6.18: *Interaction Matrix description*

and one that is combination of them. Note that, to avoid propagation of noise, we fixed to zero the terms in the red box of the so called *IM SYM*. This is due to the fact that these values are not affected by the decenters but only by tilts. Once the calibration is performed, we use the CM (i.e. RM) to reconstruct the misalignments of the system with respect to the target position, that we want to reach as the goal of the alignment process. In order to validate the calibration, we perfomed the steps listed below:

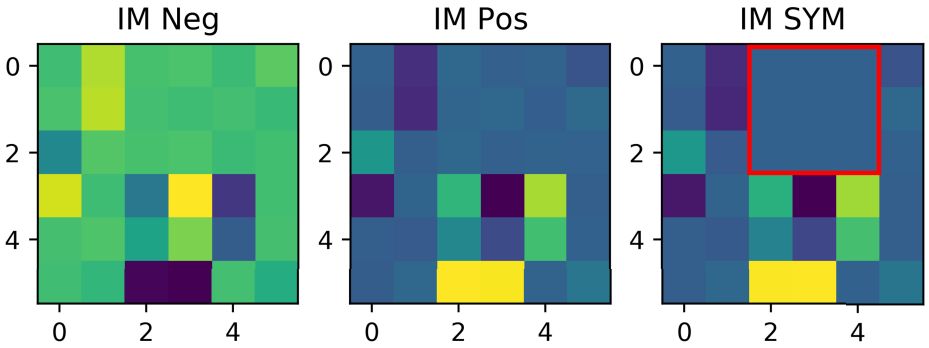

Figure 6.19: *Interaction Matrices. Left: IM computed on pull. Center:Im computed for push. Right:IM computed as combination of push and pull. The values into the red box have been fixed to zero because they are not effected by the decenter along the three axis. Note that on X axis are shown the observables, while on Y axis are shown the degrees of freedom of the system.*

- Move the Hexapod to a random misaligned position.
- Compute the difference between the observables calculated in this position and the observables target values shown in table 6.2
- Multiply this difference by the RM, obtaining the corrections
- Multiply these corrections by the amplitude of each dof that we used in the step 3 of the calibration process

6.4.1 Calibration Stability test

A second test was devoted to evaluate the stability of the calibration. In practice we wanted to understand if the system needed to be re-calibrated after each new misalignment or if a single IM, calculated at the beginning of the test, could be effectively used for a whole set of misalignments. We defined a set of 60 random misaligned positions for the 6 dof, running the alignment procedure for 2 cases:

- Perform the calibration each time before the alignment procedure.
- Perform the alignments procedure using the same calibration (i.e. CM)

Figure 6.20, shows for each observable the deviation with respect to the target values. The red dashed lines are for case 1, while the green dashed lines are for case 2. The blue dotted lines represent the expected value for the corresponding observable. We conclude from the plots that performing the calibration each time before the alignment procedure is not needed. The same is true for Figure 6.21, where are shown the plots concerning the 6 degrees of freedom shown in Figure 6.21. Note that these tests have been performed with the number of iterations for the alignment procedure fixed at 5.

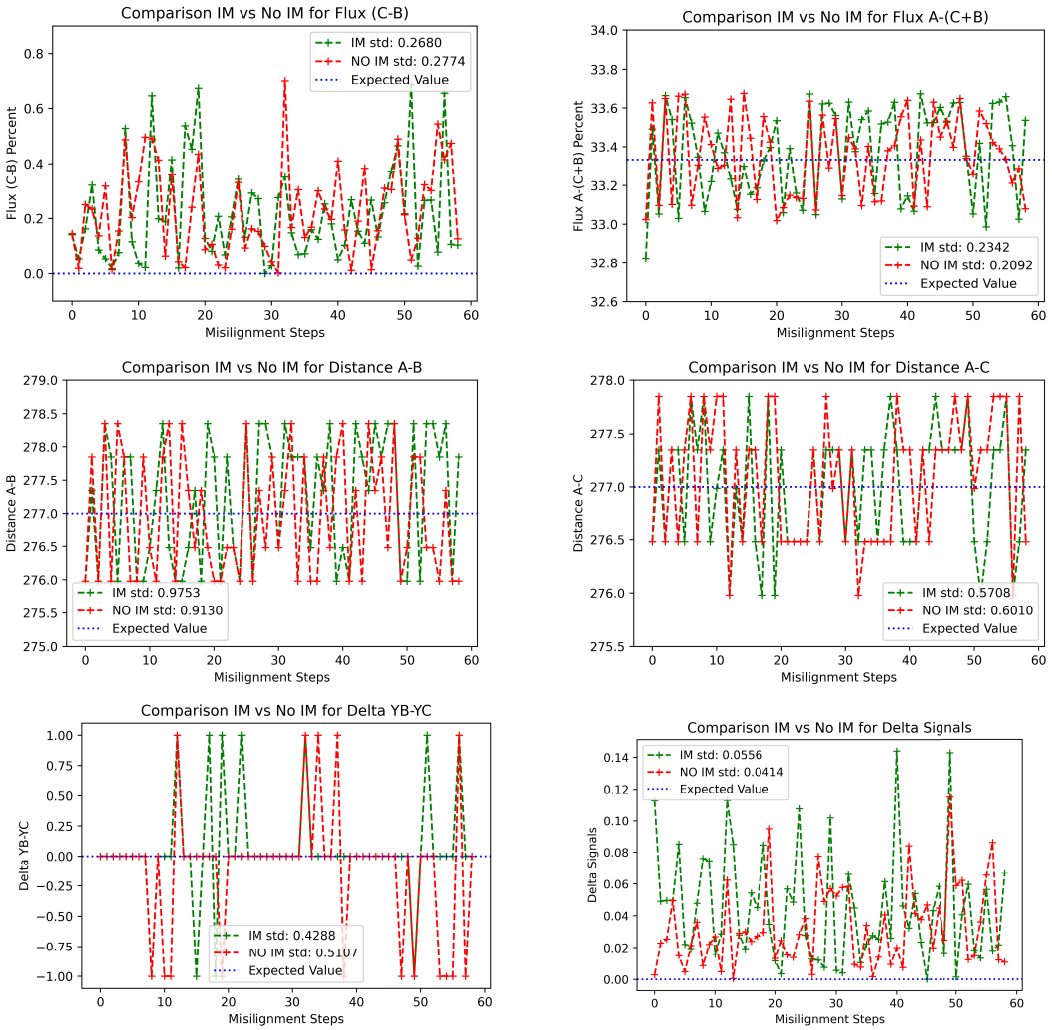

Figure 6.20: *Comparison of the alignments procedure for 60 random misalignment positions, having used the same calibration (red lines) and a new calibration for each (green lines). The plots represents the 6 observables defined*

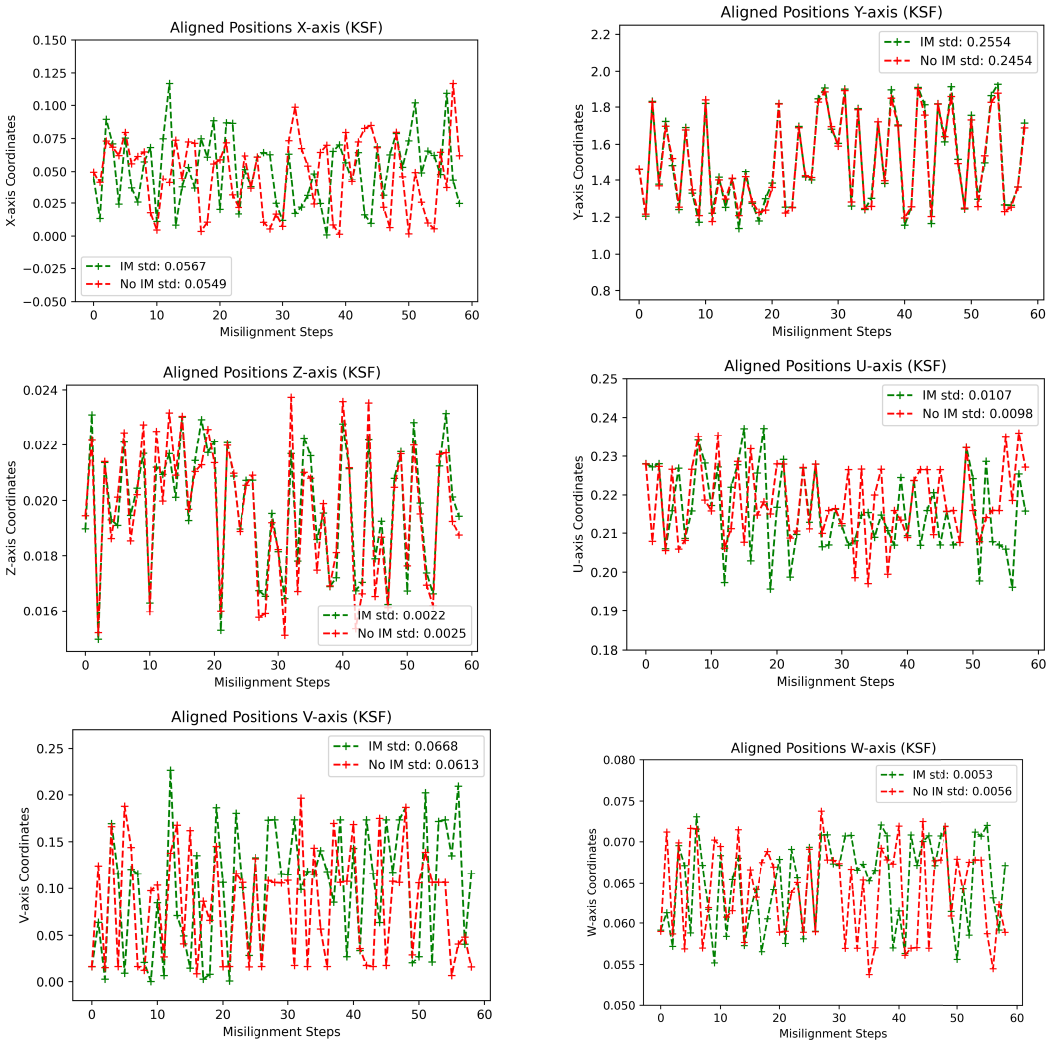

Figure 6.21: *Comparison of the alignments procedure for 60 random misalignment positions, having used the same calibration (red lines) and a new calibration for each (green lines). The plots represents the 6 degrees of freedom aligned positions*

6.4.2 Alignment Convergence Test

In order to validate the alignment procedure discussed in the previous section, we defined a set of 20 random misalignment positions to use as test, to investigate which is the proper number of iteration that the procedure should perform. The steps in this test are:

- Create a set of 20 random misaligned position for the 6 dof
- Move the Hexapod to each of these positions one at the time
- From each of these 20 position, we iterate the alignment procedure 12 times

Figure 6.22 reports the results of the test where the plots show for each of the 6 observables, the standard deviation (STD) of the observable reached at each iteration. Note that we decide to hide the first iteration, due to the fact that the STD was too high and less relevant. In addition, in each plot we add a dotted line that represent the expected value for the considered observable. While for the observables related to the flux variation, we can note an evident trend of the STD that is decreasing with increasing number of iterations. The observables related to the reciprocal position of the pupils have discretized values. Based on to the plots analysis, we have identified a minimum of 6 iterations in order to consider the system aligned "within the noise".

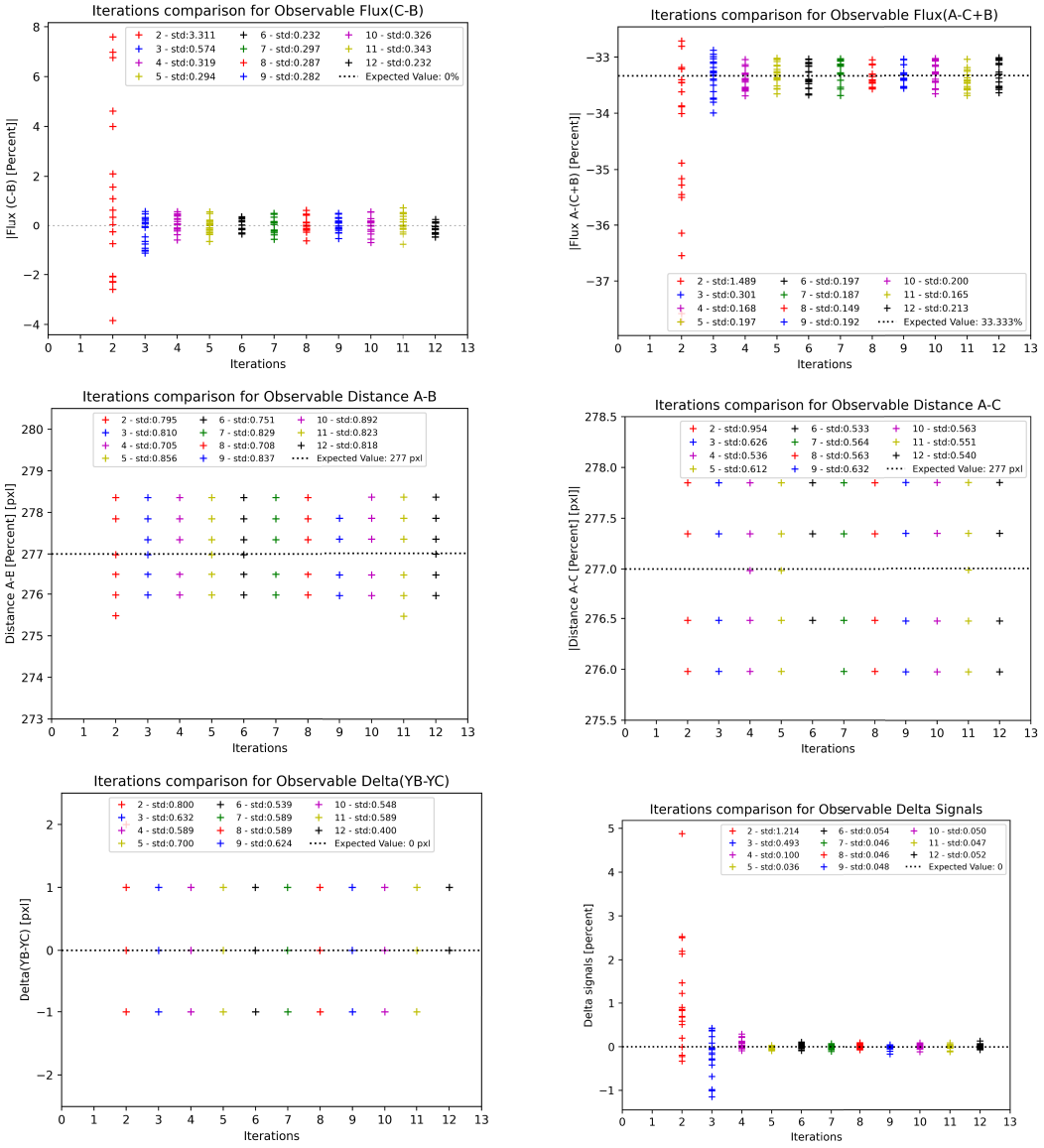

Figure 6.22: *Iteration test results for the 6 observables. The dotted lines represent the expected values for each observable.*

6.5 The Alignment to the Source Procedure

Once that the Ingot prism is properly aligned to the system, it is time to focus on the movements of the LGS in the sky. This corresponds to movement of the LGS image on the Ingot prism. This produce a variation of the flux and signals, but, once again, it will not change the position of the pupils. Thus, the distance between them cannot be used to keep the LGS image aligned to the Ingot prism during operations. Below, we describe a procedure based solely on the measurements of signals (only the low order modes) to keep the alignment between Ingot and source. In the lab, the misalignment between Ingot and source is produced by moving the Ingot via the hexapod and not by moving the source with respect to the telescope simulator. This is because, according to the current design of the bench, the source position cannot be controlled precisely through an hexapod. Doing this adds a misalignment between

Ingot and telescope, with the consequence that the pupils will move. However, we don't use the position of the pupils as an observable for this alignment step and, to a good approximation, the effect produced on the signals by the movement of the hexapod is equivalent to that produced by a movement of the source, because of the symmetry between object and image space.

6.5.1 Interaction Matrix of Misalignments

As before, the strategy adopted to reconstruct misalignments between the Ingot and the LGS image is based on a linear approximation (interaction matrix calculation). For each degree of freedom, we calculate the variation of the signal produced. We use a modal reconstruction approach by fitting the signals S_x and S_y with low order Zernike polynomials to mitigate the effects of noise and higher-order aberrations that are not related to misalignment. The fitted Zernike polynomials' coefficients are then used to build the reconstruction matrix needed to calculate the actual misalignment between the ingot and LGS image. The reconstructed misalignments are then corrected in a closed-loop fashion.

The procedure described above has been tested directly on the optical bench. After performing the first alignment of the ingot to the LGS image, we moved the Hexapod along each degree of freedom (except tilt around Y because the geometry is invariant for rotations around Y) recording the signals necessary to calculate the interaction matrix. Then, we calculated the reconstruction matrix by taking the pseudo-inverse of the interaction matrix. We thus obtained what we call a "laboratory reconstruction matrix". We applied the same procedure on simulated images as well, obtaining a "synthetic reconstruction matrix". The rationale of building a synthetic reconstruction matrix is that of testing the consistency between the model and the real setup. Moreover, if we can rely on a synthetic reconstruction matrix, the alignment procedure would not necessarily require a dedicated calibration source inside the instrument.

6.5.2 Closed-loop Test

The reconstruction matrices have been tested by adding a random combination of misalignments to the ingot using the Hexapod and reconstructing it from the recorded signals. We performed multiple iterations in a closed-loop fashion and the system converges back to the aligned condition. Figure 6.23 shows the residual misalignment error as a function of the iteration number for one of the tested cases. The left panel plot represents the laboratory reconstruction matrix, while that on the right represents the synthetic reconstruction matrix, starting from the same misaligned condition. In both cases, after approximately 6 iterations, the Ingot converges back to the aligned condition, but with slightly larger residuals in the case of the synthetic IM. This is somehow expected because the simulations do not exactly match the real setup. Despite this, the residuals are $< 10\%$ with respect to the input misalignment, and the loop is stable after 6 iterations.

6.6 A deformable lens as an aberrator

In order to obtain actual I-WFS response to distortions (signals), we decided to insert known aberrations in the optical path to compare them to the simulated ones. This allowed us (1) to disentangle errors due to the setup itself, (2) to explore

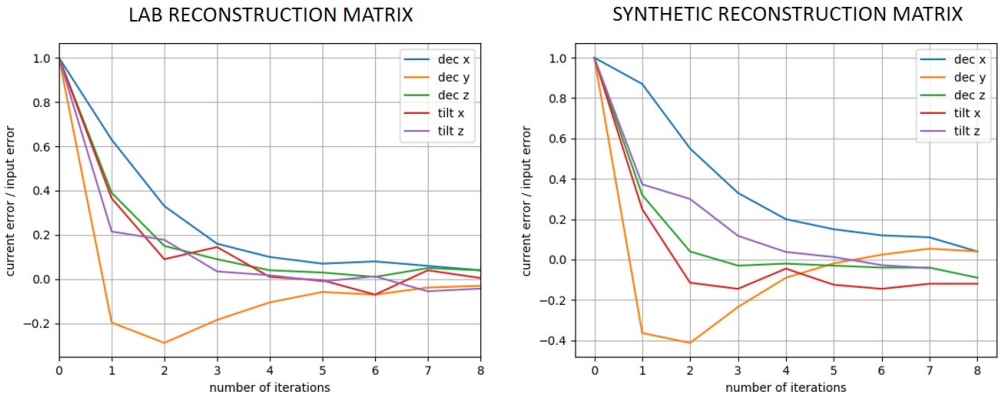

Figure 6.23: *Residual alignment error normalized by the input error as a function of the iteration number for the laboratory IM (left) and the synthetic IM (right).*

aspects which were not taken into account in the simulations, and (3) to speed up the understanding of the pros and cons of the new sensor in view of determining a path for the fine-tuning.

The device chosen to introduce the aberrations is a Multi-Actuator Lens (MAL), presenting two notable advantages with respect to other solutions: (1) the MAL does not require to modify the existent optical path and (2) its installation is extremely straightforward, common off-the-shelf lab parts can be used to hold it, its electronics is very compact, and the lens is operated through a standard laptop.

6.6.0.1 Multi-actuator lens

The Multi-Actuator Lens, developed at the CNR laboratories in Padova, is a piezoelectric-type wavefront corrector composed of two thin glass membranes, spaced apart by a chamber filled with transparent oil. Its transmission (in the absence of anti-reflection coatings) is about 90% in the range $400-1100\ nm$. Each glass membrane is bonded to a piezoelectric ring divided into 9 sectors on each side, representing the actuators. By applying a driving voltage (maximum range $\pm 125\ V$) to each sector, it is possible to bend the glass membrane locally. Linearly combining the actuators, it is possible to generate aberrations up to the 4th radial order of Zernike polynomials, with a maximum amplitude (mode dependent) of up to a dozen sodium wavelengths. In the astronomical field, MAL has proven its potential both during on-sky observations for small telescopes [75] and in a laboratory experiment to compensate low order Non Common Path Aberrations (NCPA), to exploit the full capabilities of a pyramid wavefront sensor [76]. Further details on the MAL (transmission spectrum, response time curve, chromaticity, etc.) can be found in [77], [78], [79].

6.6.0.2 Experimental setup

For this experiment, we placed a MAL with a 25 mm clear aperture and 18 actuators (9 on each side of the lens) at the pupil of the setup shown in Figure 6.2 (see Figure 6.24). All tests involving the MAL were performed with an Apple iPad screen (9.7" back-illuminated LED, 2048x1536 pixels, 264 ppi) as an LGS source, because the OLED screen was not available at that momnet. Note that the source's size was different from the one used on the OLED screen this time the characteristics were 44.5 mm in length and 1 mm in width. The MAL had been previously characterized

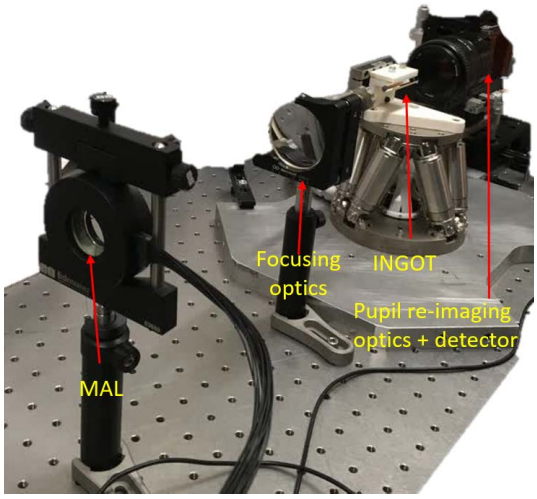

Figure 6.24: *MAL inserted at the pupil location in the I-WFS test-bench, in order to introduce known aberrations.*

and some tests were performed to determine how accurately the aberrations could be reproduced, finding a repeatability within 0.1λ RMS.

After aligning the I-WFS to the source, we collected data for two tests: (1) I-WFS signal response to input aberration and (2) I-WFS signal correlation with the amplitude of the input aberration. For the first test, for each Zernike mode, we applied the highest possible achievable amplitude (see Table 6.3), which, as stated earlier, is mode dependent. After applying each aberration, we saved 10 frames (an example, trefoil, is shown in the right panel of Figure 6.25). We also collected 10 frames with the MAL flat, acting as an optical window, for static signal subtraction (see left panel of Figure 6.25). For the second test, we applied Trefoil x aberration to the MAL, with different aberrations amplitudes between each time recording the signals from the Ingot.

Aberration type	**Maximum Aberration amplitude (waves rms)**
Tip/Tilt	4.3/4.4
Defocus	3
Astigmatism (x/y)	2.3/2.4
Coma (x/y)	0.65/0.6
Trefoil (x/y)	1.3/2
Spherical	0.55
Secondary astigmatism (x/y)	0.33/0.35
Tetrafoil (x/y)	0.65/0.55

Table 6.3: *MAL maximum applicable aberration per Zernike mode (in waves RMS, λ = 633 nm)*

6.6.0.3 Results and Analysis

We estimated the signals from the three pupils as described in Section 6.2. When analyzing them and comparing to the simulations, a few fine-tuning of parameters, such as rotating the aberration map to match the setup orientation, were required.

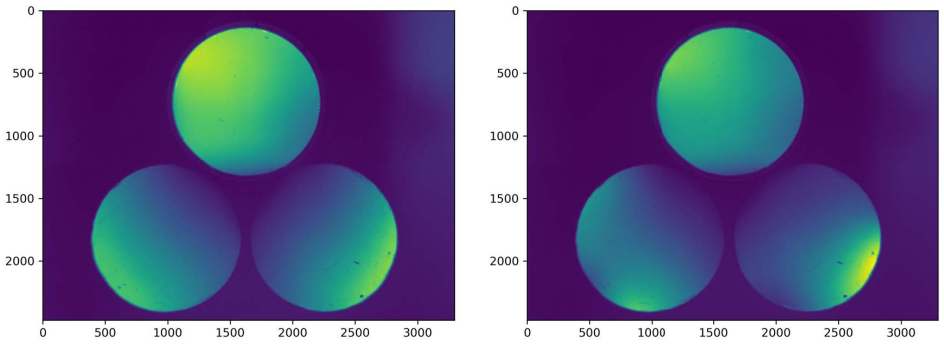

Figure 6.25: *Left: I-WFS pupil when the MAL is flat, Right: I-WFS pupil when trefoil is applied on the MAL.*

Figure 6.26 shows a few examples (defocus, astigmatism, trefoil) of the signals simulated (top row) and the ones obtained on the lab setup introduced by the MAL (bottom row). The signals extracted from real images appear qualitatively similar

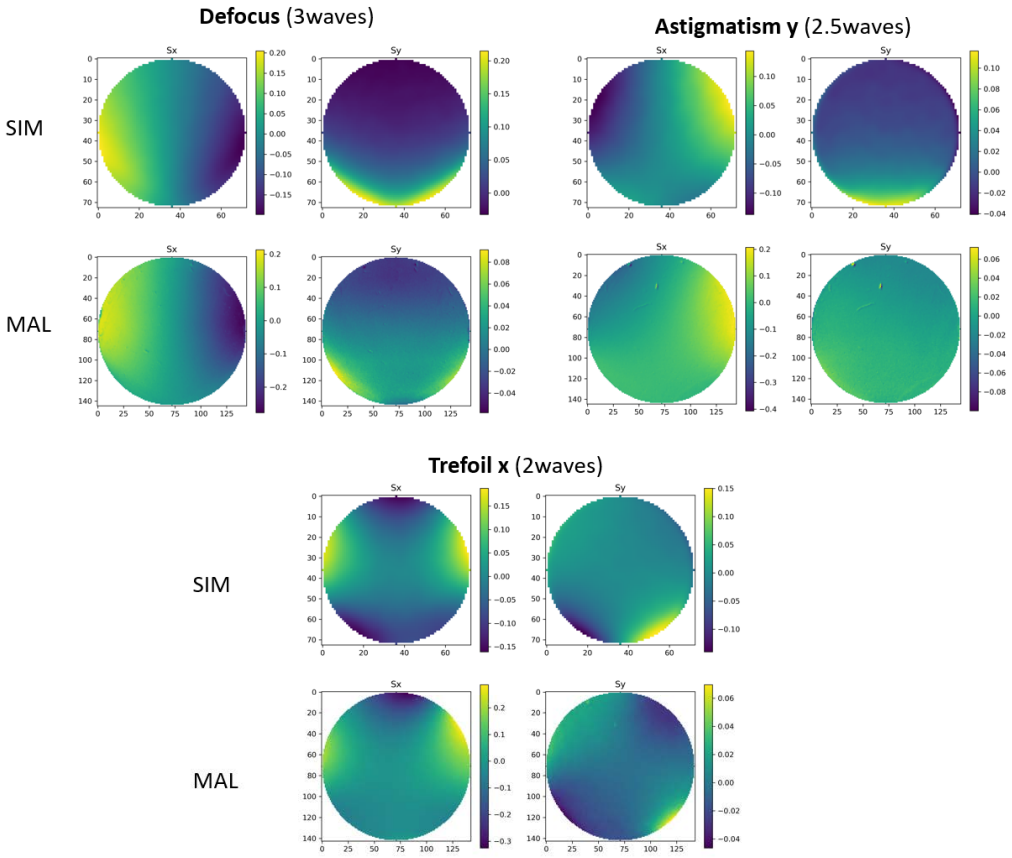

Figure 6.26: *Simulated (top row) vs lab (bottom row) signals for three aberrations: defocus, astigmatism and trefoil. The amplitude of the aberrations are 3, 2.5 and 2 waves rms, respectively (the maximum achievable by this MAL, as per Table 6.3). Please note that colour bars are different.*

to the simulated ones. However, the intensity differs between simulated and real data. The real data shows higher signal X and lower signal Y in comparison to

the simulated one. The main problem was identified in the source itself, particularly the background generated by black pixels, which were producing a lot of flux in the transmitted pupil, thus reducing the system's dynamical range. Moreover, the illumination of the pupil was not uniform due to the angular emissivity profile of the screen, which can be seen as a gradient in the sum of the three pupils, see Figure 6.27.

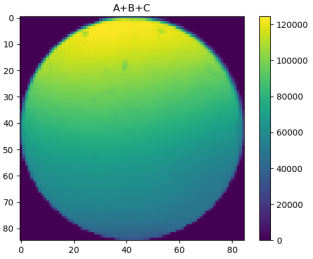

Figure 6.27: *Pupil obtained from the sum of the three pupils in the case where no aberrations where introduced in the setup. A clear gradient along the Y axis is visible.*

Given the above considerations, in order to reduce the impact of the source-related and being able to determine the correlation of I-WFS responses to variation of aberration amplitude, we considered the response of a few sub-apertures located in areas most strongly affected by Trefoil aberration, as depicted in Figure 6.28. There is a clear linear relation between the applied input aberration and the retrieved signal for the two sub-aperture cases. However, note that the signal Y is always lower than X signal.

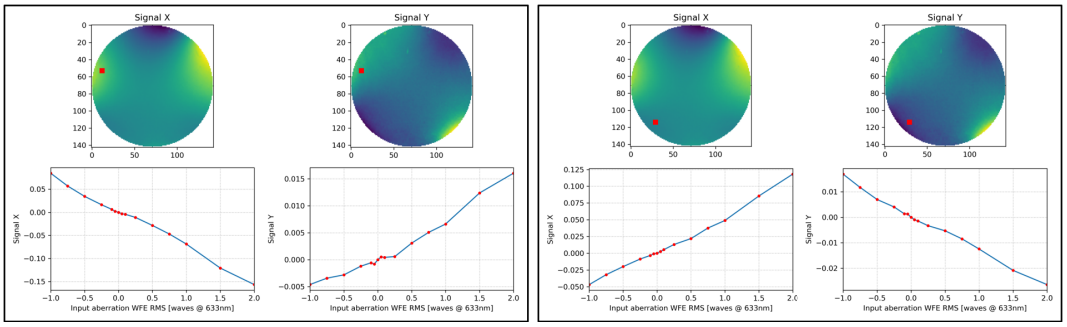

Figure 6.28: *Trefoil signals computed for two sub-apertures (left and right panels). Top panel shows the trefoil signals and the identified sub-aperture for the analysis. Lower panel plots the I-WFS signals for each applied aberration amplitude (red dots).*

For this reason, we have decided for future testing to opt for a different source with a lower background noise, namely the OLED source, used for the other experiments described in this work.

6.7 Upgrades and Future

In order to mitigate stray light effects, we added a black cover over the test bench, as shown in Figure 6.29. In addition, as shown in Figure 6.30, we have equipped the bench with a Deformable Lens (DL) conjugated to the pupil plane. This device has a clear aperture of 25.5 mm that is in line with the requirements of the bench to maintain the setup telecentric. Similar to the MAL (see section 6.6.0.2, the DL

Figure 6.29: *The I-WFS test bench with a black cover used to mitigate the effects of stray light.*

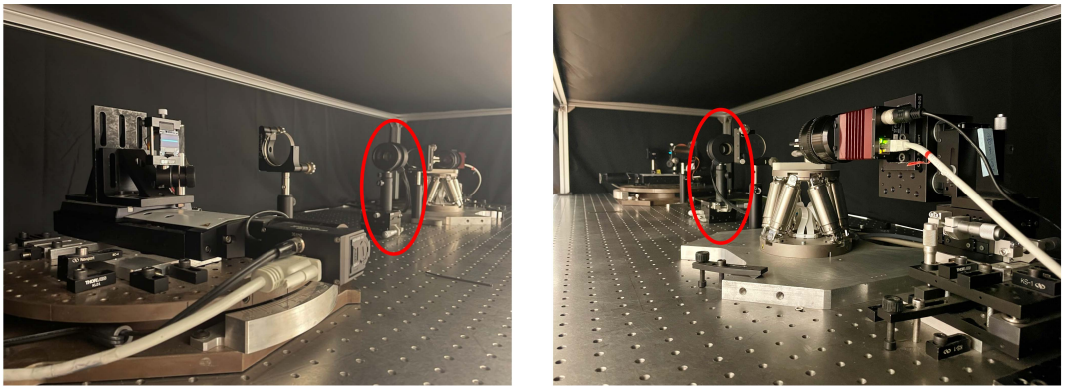

Figure 6.30: *View of the I-WFS test bench, equipped with a Deformable Lens conjugated to the pupil plane*

is able to apply the first 18 zernikes modes, one by one or as a combination of them. In the next months, we want to characterize the I-WFS response to low-order aberrations in terms of sensitivity and linearity, using the results as a comparison for the simulations validation. Notice that in according to the current designed, the bench is now equipped with the OLED screen, (to reproduce the LGS), that was not available for the tests performed with the MAL.

Conclusions

As we have seen all along the thesis, Adaptive Optics present a novel technique to address complex problems providing huge improvements with respect to the results obtained with classical optics, providing at least in principle diffraction-limited imaging. This result is obtained by measuring the wavefront aberration imposed by the Earth's atmosphere using a suitably bright reference star and compensating for these aberrations through a deformable mirror. The reference object must be located inside of the so-called isoplanatic angle, but unlikely this requirement decreases dramatically the the fraction of the sky coverage. The possible solution to this problem is to create an artificial reference in the sky, the so-called Sodium Laser Guide Star (LGS). This facility gives to the telescope the capability to enlarge the sky coverage, creating an artificial reference star, to compensate for the absence of a sufficiently bright star for wavefront sensing. However, LGSs are not point-like sources, but rather elongated objects in three-dimensional space. This is due to the intrinsic nature of the sodium layer, which is located at about 90 km altitude in the atmosphere and extended for approximately 20 km. The Ingot Wavefront Sensor (I-WFS) has been proposed as a novel pupil plane wavefront sensor, to cope with the intrinsic elongation effects of the Sodium Laser Guide Stars. This elongation in the case of extremely large telescopes, such as the European Extremely Large Telescope, it translates in a not negligible issue when a typical LGS wavefront sensor is used. In this work, I focused on the optical design, the assembly, the integration and verification of the I-WFS. I reported the two version of the optical designed developed, focusing on the 3-faces version which is the one chosen for the laboratory tests. In this framework, I performed a test both in a already available laboratory test bench, hosted at the Laboratory of Marseille, where the I-WFS has been simulated using a spatial light modulator, that is able to reproduce a 2D version of the wavefront sensor. On the other hand, I designed and developed an optical test bench at the Osservatorio Astronomico di Padova, to test which is the behavior of the I-WFS. I described the two alignment procedures developed, and the report the preliminary results of the I-WFS sensitivity when a aberration pattern is applied. The project was also affected by the current pandemic situation, having to evolve through a more remote path that was initially foreseen. The result of that turn was the development of a fully automated process that allowed us to control the instrument from any position and at any time. Our final conclusion, based on the whole work done in the project, is that the research was fruitful and more ambitious plans are in view in the near future.

List of Figures

List of Tables

Bibliography

[1] F. A. Jenkins and H. E. White. *Fundamentals of optics*. 1957.

[2] A. Kolmogorov. "The Local Structure of Turbulence in Incompressible Viscous Fluid for Very Large Reynolds' Numbers". In: *Akademiia Nauk SSSR Doklady* 30 (1941), pp. 301–305.

[3] F. Roddier. "The effects of atmospheric turbulence in optical astronomy". In: *Progress in optics. Volume 19. Amsterdam, North-Holland Publishing Co., 1981, p. 281-376.* 19 (1981), pp. 281–376. DOI: 10.1016/S0079-6638(08)70204-X.

[4] D.∼L. Fried. "Statistics of a Geometric Representation of Wavefront Distortion". In: *Journal of the Optical Society of America (1917-1983)* 55 (Nov. 1965), pp. 1427–1431.

[5] Roberto Ragazzoni. "Pupil plane wavefront sensing with an oscillating prism". In: *Journal of Modern Optics* 43.2 (Feb. 1996), pp. 289–293. DOI: 10.1080/09500349608232742.

[6] Roberto Ragazzoni and J Farinato. "Sensitivity of a pyramidic wave front sensor in closed loop adaptive optics". In: *Astronomy and Astrophysics* 350 (1999), pp. L23–L26.

[7] Roberto Ragazzoni. "Pupil plane wavefront sensing with an oscillating prism". In: *Journal of modern optics* 43.2 (1996), pp. 289–293.

[8] E. Gendron and P. Lena. "Astronomical adaptive optics. I. Modal control optimization." In: *aap* 291.1 (Nov. 1994), pp. 337–347.

[9] R.∼J. Noll. "Zernike polynomials and atmospheric turbulence". In: *Journal of the Optical Society of America (1917-1983)* 66 (1976), pp. 207–211.

[10] J. Y. Wang and J. K. Markey. "Modal compensation of atmospheric turbulence phase distortion". In: *Journal of the Optical Society of America (1917-1983)* 68 (Jan. 1978), pp. 78–87.

[11] F. Roddier. "Wavefront sensing and the irradiance transport equation". In: *Appl. Opt.* 29 (Apr. 1990), pp. 1402–1403. DOI: 10.1364/AO.29.001402.

[12] J. M. Beckers. "Adaptive optics for astronomy - Principles, performance, and applications". In: *Astron. & Astrophys.* ().

[13] R. Foy and A. Labeyrie. "Feasibility of adaptive telescope with laser probe". In: *"Astron. & Astrophys."* 152 (Nov. 1985), pp. L29–L31.

[14] Pfrommer, T. and Hickson, P. "High resolution mesospheric sodium properties for adaptive optics applications". In: *A&A* 565 (2014), A102. DOI: 10.1051/0004-6361/201423460. URL: https://doi.org/10.1051/0004-6361/201423460.

[15] G. Rousset et al. "NAOS, the first AO system of the VLT: on-sky performance". In: *Adaptive Optical System Technologies II*. Ed. by P. L. Wizinowich and D. Bonaccini. Vol. 4839. 2003, pp. 140–149. DOI: 10.1117/12.459332.

[16] F. Eisenhauer. "The galactic center: The ideal laboratory for studying supermassive black holes". In: *Relativity in Fundamental Astronomy: Dynamics, Reference Frames, and Data Analysis*. Ed. by S. A. Klioner, P. K. Seidelmann, and M. H. Soffel. Vol. 261. IAU Symposium. 2010, pp. 269–270. DOI: 10.1017/S1743921309990494.

[17] S. Gillessen et al. "The Orbit of the Star S2 Around SGR A* from Very Large Telescope and Keck Data". In: 707 (2009), pp. L114–L117. DOI: 10.1088/0004-637X/707/2/L114. eprint: 0910.3069.

[18] R. Genzel, F. Eisenhauer, and S. Gillessen. "The Galactic Center massive black hole and nuclear star cluster". In: *Reviews of Modern Physics* 82 (2010), pp. 3121–3195. DOI: 10.1103/RevModPhys.82.3121. eprint: 1006.0064.

[19] R. Genzel et al. "A study of the gas-star formation relation over cosmic time". In: *Monthly Notices of the Royal Astronomical Society* 407.4 (2010), pp. 2091–2108. ISSN: 0035-8711. DOI: 10.1111/j.1365-2966.2010.16969.x. URL: http://dx.doi.org/10.1111/j.1365-2966.2010.16969.x.

[20] L. Ferrarese and H. Ford. "Supermassive Black Holes in Galactic Nuclei: Past, Present and Future Research". In: *ssr* 116 (2005), pp. 523–624. DOI: 10.1007/s11214-005-3947-6. eprint: astro-ph/0411247.

[21] K. Gebhardt et al. "A Relationship between Nuclear Black Hole Mass and Galaxy Velocity Dispersion". In: *apjl* 539 (2000), pp. L13–L16. DOI: 10.1086/312840. eprint: astro-ph/0006289.

[22] N. Häring and H.-W. Rix. "On the Black Hole Mass-Bulge Mass Relation". In: *apjl* 604 (2004), pp. L89–L92. DOI: 10.1086/383567. eprint: astro-ph/0402376.

[23] R. I. Davies et al. "The Star-forming Torus and Stellar Dynamical Black Hole Mass in the Seyfert 1 Nucleus of NGC 3227". In: *apj* 646.2 (Aug. 2006), pp. 754–773. DOI: 10.1086/504963. arXiv: astro-ph/0604125 [astro-ph].

[24] K. D. Denney et al. "Reverberation Mapping Measurements of Black Hole Masses in Six Local Seyfert Galaxies". In: *apj* 721 (2010), pp. 715–737. DOI: 10.1088/0004-637X/721/1/715. arXiv: 1006.4160.

[25] K. Gültekin et al. "The M-σ and M-L Relations in Galactic Bulges, and Determinations of Their Intrinsic Scatter". In: *apj* 698 (2009), pp. 198–221. DOI: 10.1088/0004-637X/698/1/198. arXiv: 0903.4897 [astro-ph.GA].

[26] John Kormendy, Rolf Bender, and ME Cornell. "Supermassive black holes do not correlate with galaxy disks or pseudobulges". In: *Nature* 469.7330 (2011), pp. 374 –376. URL: https://doi.org/10.1038/nature09694.

[27] Chris Orban and David H Weinberg. "Self-similar bumps and wiggles: Isolating the evolution of the BAO peak with power-law initial conditions". In: *Physical Review D* 84.6 (2011), pp. 063501–06350126. DOI: 101103/PhysRevD84063501.

[28] David B. Fisher and Niv Drory. "Demographics of Bulge Types within 11 Mpc and Implications for Galaxy Evolution". In: *apjl* 733.2, L47 (June 2011), p. L47. DOI: 10.1088/2041-8205/733/2/L47. arXiv: 1104.0020 [astro-ph.CO].

[29] Tim Weinzirl et al. "Bulge n and B/T in High-Mass Galaxies: Constraints on the Origin of Bulges in Hierarchical Models". In: *apj* 696.1 (May 2009), pp. 411–447. DOI: 10.1088/0004-637X/696/1/411. arXiv: 0807.0040 [astro-ph].

[30] Nina Nowak et al. "Do black hole masses scale with classical bulge luminosities only? The case of the two composite pseudo-bulge galaxies NGC 3368 and NGC 3489". In: *Monthly Notices of the Royal Astronomical Society* 403.2 (2010), pp. 646–672. URL: https://doi.org/10.1111/j.1365-2966.2009.16167.x.

[31] Karl Gebhardt et al. "The Black Hole Mass in M87 from Gemini/NIFS Adaptive Optics Observations". In: *apj* 729.2, 119 (Mar. 2011), p. 119. DOI: 10.1088/0004-637X/729/2/119. arXiv: 1101.1954 [astro-ph.CO].

[32] R. I. Davies et al. "Stellar and Molecular Gas Kinematics Of NGC 1097: Inflow Driven by a Nuclear Spiral". In: *apj* 702.1 (Sept. 2009), pp. 114–128. DOI: 10.1088/0004-637X/702/1/114. arXiv: 0903.0313 [astro-ph.CO].

[33] Kambiz Fathi et al. "Streaming Motions toward the Supermassive Black Hole in NGC 1097". In: *The Astrophysical Journal* 641.1 (2006), pp. L25–L28. DOI: 10.1086/503832. URL: https://doi.org/10.1086/503832.

[34] Rogemar A. Riffel et al. "Mapping of molecular gas inflow towards the Seyfert nucleus of NGC4051 using Gemini NIFS". In: *mnras* 385.3 (2008), pp. 1129–1142. ISSN: 1365-2966. DOI: 10.1111/j.1365-2966.2008.12936.x. URL: http://dx.doi.org/10.1111/j.1365-2966.2008.12936.x.

[35] Allan Schnorr M$\surd$*llerEtal.*. "Gas streaming motions towards the nucleus of M81". In: *mnras* 413.1 (Apr. 2011), pp. 149–161. ISSN: 0035-8711. DOI: 10.1111/j.1365-2966.2010.18116.x. eprint: https://academic.oup.com/mnras/article-pdf/413/1/149/18582034/mnras0413-0149.pdf. URL: https://doi.org/10.1111/j.1365-2966.2010.18116.x.

[36] R. Cid Fernandes et al. "The star formation history of Seyfert 2 nuclei". In: *mnras* 355.1 (Nov. 2004), pp. 273–296. ISSN: 0035 – 8711. DOI: 10.1111/j.1365-2966.2004.08321.x. eprint: https://academic.oup.com/mnras/article-pdf/355/1/273/11179832/355-1-273.pdf. URL: https://doi.org/10.1111/j.1365-2966.2004.08321.x.

[37] R. Riffel et al. "Probing the near-infrared stellar population of Seyfert galaxies". In: *mnras* 400.1 (Nov. 2009), pp. 273–290. DOI: 10.1111/j.1365-2966.2009.15448.x. arXiv: 0907.4144 [astro-ph.CO].

[38] R. I. Davies et al. "A Close Look at Star Formation around Active Galactic Nuclei". In: *apj* 671.2 (Dec. 2007), pp. 1388–1412. DOI: 10.1086/523032. arXiv: 0704.1374 [astro-ph].

[39] Vivienne Wild, Timothy Heckman, and Stéphane Charlot. "Timing the starburst - AGN connection". In: *mnras* 405.2 (June 2010), pp. 933–947. ISSN: 0035-8711. DOI: 10.1111/j.1365-2966.2010.16536.x. eprint: https://academic.oup.com/mnras/article-pdf/405/2/933/3999644/mnras0405-0933.pdf. URL: https://doi.org/10.1111/j.1365-2966.2010.16536.x.

[40] M. Schartmann et al. "Gas dynamics of the central few parsec region of NGC 1068 fuelled by the evolving nuclear star cluster". In: *mnras* 403.4 (Apr. 2010), pp. 1801–1811. DOI: 10.1111/j.1365-2966.2010.16250.x. arXiv: 0912.4677 [astro-ph.CO].

[41] David Raban et al. "Resolving the obscuring torus in NGC 1068 with the power of infrared interferometry: revealing the inner funnel of dust". In: *mnras* 394.3 (Apr. 2009), pp. 1325–1337. DOI: 10.1111/j.1365-2966.2009.14439.x. arXiv: 0901.1306 [astro-ph.GA].

[42] K. R. W. Tristram et al. "Resolving the complex structure of the dust torus in the active nucleus of the Circinus galaxy". In: *aap* 474.3 (Nov. 2007), pp. 837–850. DOI: 10.1051/0004-6361:20078369. arXiv: 0709.0209 [astro-ph].

[43] E. K. S. Hicks et al. "The Role of Molecular Gas in Obscuring Seyfert Active Galactic Nuclei". In: *apj* 696.1 (May 2009), pp. 448–470. DOI: 10.1088/0004-637X/696/1/448. arXiv: 0902.0978 [astro-ph.GA].

[44] Michael D. Crenshaw. "Mass outflows in Narrow-Line Seyfert 1 Galaxies". In: *PoS* NLS1 (2011), p. 027. DOI: 10.22323/1.126.0027.

[45] O. Guyon, D. B. Sanders, and Alan Stockton. "Near-Infrared Adaptive Optics Imaging of QSO Host Galaxies". In: *apjs* 166.1 (Sept. 2006), pp. 89–127. DOI: 10.1086/505030. arXiv: astro-ph/0605079 [astro-ph].

[46] Scott M. Croom et al. "Gemini Imaging of QSO Host Galaxies at z $\sim$ 2". In: *apj* 606.1 (May 2004), pp. 126–138. DOI: 10.1086/382747. arXiv: astro-ph/0401442 [astro-ph]. URL: http://dx.doi.org/10.1086/382747.

[47] R Falomo et al. "VLT adaptive optics imaging of QSO host galaxies and their close environment at z $\sim$ 2.5: Results from a pilot program". In: *Astronomy & Astrophysics* 434.2 (2005), pp. 469–473. URL: https://doi.org/10.1051/0004-6361:20041894.

[48] Donald P. Schneider et al. "The Sloan Digital Sky Survey Quasar Catalog. IV. Fifth Data Release". In: *aj* 134.1 (July 2007), pp. 102–117. DOI: 10.1086/518474. arXiv: 0704.0806 [astro-ph].

[49] Claire E. Max, Gabriela Canalizo, and Willem H. de Vries. "Locating the Two Black Holes in NGC 6240". In: *Science* 316.5833 (June 2007), p. 1877. DOI: 10.1126/science.1136205.

[50] H. Engel et al. "NGC 6240: merger-induced star formation and gas dynamics". In: *aap* 524, A56 (Dec. 2010), A56. DOI: 10.1051/0004-6361/201015338. arXiv: 1009.1539 [astro-ph.CO].

[51] Daniela Calzetti et al. "The Dust Content and Opacity of Actively Star-forming Galaxies". In: *apj* 533.2 (Apr. 2000), pp. 682–695. DOI: 10.1086/308692. arXiv: astro-ph/9911459 [astro-ph].

[52] Anne M. Medling et al. "Mass of the Southern Black Hole in NGC 6240 from Laser Guide Star Adaptive Optics". In: *apj* 743.1, 32 (Dec. 2011), p. 32. DOI: 10.1088/0004-637X/743/1/32. arXiv: 1108.5180 [astro-ph.CO].

[53] N. M. Förster Schreiber et al. "The SINS Survey: SINFONI Integral Field Spectroscopy of z $\sim$ 2 Star-forming Galaxies". In: *apj* 706.2 (Dec. 2009), pp. 1364–1428. DOI: 10.1088/0004-637X/706/2/1364. arXiv: 0903.1872 [astro-ph.CO].

[54] David R. Law et al. "The Kiloparsec-scale Kinematics of High-redshift Star-forming Galaxies". In: *apj* 697.2 (June 2009), pp. 2057–2082. DOI: 10.1088/0004-637X/697/2/2057. arXiv: 0901.2930 [astro-ph.GA].

[55] Shelley A. Wright et al. "Dynamics of Galactic Disks and Mergers at z $\sim$ 1.6: Spatially Resolved Spectroscopy with Keck Laser Guide Star Adaptive Optics". In: *apj* 699.1 (July 2009), pp. 421–440. DOI: 10.1088/0004-637X/699/1/421. arXiv: 0810.5599 [astro-ph].

[56] E. Wisnioski. "Clumpy Star-formation at z=1.5 in the WiggleZ Dark Energy Survey". In: *Galaxy Formation*. July 2011, P43.

[57] F. Mannucci et al. "LSD: Lyman-break galaxies Stellar populations and Dynamics - I. Mass, metallicity and gas at z ~3.1". In: *mnras* 398.4 (Oct. 2009), pp. 1915–1931. DOI: 10.1111/j.1365-2966.2009.15185.x. arXiv: 0902.2398 [astro-ph.CO].

[58] G. Cresci et al. "The SINS Survey: Modeling the Dynamics of z $\sim$ 2 Galaxies and the High-z Tully-Fisher Relation". In: *apj* 697.1 (May 2009), pp. 115–132. DOI: 10.1088/0004-637X/697/1/115. arXiv: 0902.4701 [astro-ph.CO].

[59] Emiliano Diolaiti et al. "Dual-channel multiple natural guide star wavefront sensor for the E-ELT multiconjugate adaptive optics module". In: *Adaptive Optics Systems III*. Ed. by Brent L. Ellerbroek, Enrico Marchetti, and Jean-Pierre V$\surd$©*ran*. Vol. 8447. International Society for Optics and Photonics. SPIE, 2012, pp. 595 –602. DOI: 10.1117/12.927091. URL: https://doi.org/10.1117/12.927091.

[60] Sylvain Oberti et al. "LGS tomography and spot truncation: tips and tricks". In: *6th International Conference on Adaptive Optics for Extremely Large Telescopes, AO4ELT 2019*. Québec, Canada, June 2019. URL: https://hal.archives-ouvertes.fr/hal-02614170.

[61] M. Lombini et al. "Optical design of the post focal relay of MAORY". In: *Optical Design and Engineering VII*. Ed. by Laurent Mazuray, Rolf Wartmann, and Andrew P. Wood. Vol. 10690. International Society for Optics and Photonics. SPIE, 2018, pp. 228 –238. DOI: 10.1117/12.2312010. URL: https://doi.org/10.1117/12.2312010.

[62] Valentina Viotto et al. "Dealing with the cigar: preliminary performance estimation of an INGOT WFS". In: *Adaptive Optics Systems VI*. Ed. by Laird M. Close, Laura Schreiber, and Dirk Schmidt. Vol. 10703. July 2018, p. 107030V. DOI: 10.1117/12.2313219.

[63] P. Janin-Potiron, B. Neichel, and T. Fusco. "Development of the adaptive optics testbed LOOPS for Fourier-based wavefront sensors demonstration and analysis". In: *SF2A-2018: Proceedings of the Annual meeting of the French Society of Astronomy and Astrophysics*. Ed. by P. Di Matteo et al. Dec. 2018, p. Di.

[64] Pierre Janin-Potiron et al. "Adaptive optics with programmable Fourier-based wavefront sensors: a spatial light modulator approach to the LAM/ONERA on-sky pyramid sensor testbed". In: *Journal of Astronomical Telescopes, Instruments, and Systems* 5.3 (2019), pp. 1 –10. DOI: 10.1117/1.JATIS.5.3.039001. URL: https://doi.org/10.1117/1.JATIS.5.3.039001.

[65] Simone Di Filippo et al. "INGOT Wavefront Sensor: from the optical design to a preliminary laboratory test". English. In: *AO4ELT6*. 2019.

[66] Carmelo Arcidiacono et al. "Ingot wavefront sensor: from the Fourier End2End numerical simulation to the LOOPS test bench". In: *Adaptive Optics Systems VII*. Ed. by Laura Schreiber, Dirk Schmidt, and Elise Vernet. Vol. 11448. International Society for Optics and Photonics. SPIE, 2020, pp. 1249 –1260. DOI: 10.1117/12.2562355. URL: https://doi.org/10.1117/12.2562355.

[67] R. Conan and C. Correia. "Object-oriented Matlab adaptive optics toolbox". In: *Adaptive Optics Systems IV*. Vol. 9148. Aug. 2014, p. 91486C. DOI: 10.1117/12.2054470. URL: https://www.spiedigitallibrary.org/conference-proceedings-of-spie/9148/91486C/Object-oriented-Matlab-adaptive-optics-toolbox/10.1117/12.2054470.short (visited on 11/30/2020).

[68] Christophe Vérinaud. "On the nature of the measurements provided by a pyramid wave-front sensor". In: *Optics Communications* 233.1,Äì3 (2004), pp. 27 –38. ISSN: 0030-4018. DOI: 10.1016/j.optcom.2004.01.038. URL: http://www.sciencedirect.com/science/article/pii/S0030401804000628.

[69] C. Arcidiacono et al. "End to end numerical simulations of the MAORY multiconjugate adaptive optics system". In: *Adaptive Optics Systems IV*. Ed. by Enrico Marchetti, Laird M. Close, and Jean-Pierre Vran. Vol. 9148. Aug. 2014, 91486F. DOI: 10.1117/12.2055608. arXiv: 1408.0698 [astro-ph.IM].

[70] C. Arcidiacono et al. "Numerical simulations of MAORY MCAO module for the ELT". In: *Adaptive Optics Systems VI*. Ed. by Laird M. Close, Laura Schreiber, and Dirk Schmidt. Vol. 10703. July 2018, p. 107034I. DOI: 10.1117/12.2311702.

[71] A. Kolmogorov. "The Local Structure of Turbulence in Incompressible Viscous Fluid for Very Large Reynolds' Numbers". In: *Akademiia Nauk SSSR Doklady* 30 (1941), pp. 301–305.

[72] A. N. Kolmogorov. "Dissipation of Energy in Locally Isotropic Turbulence". In: *Akademiia Nauk SSSR Doklady* 32 (1941), p. 16.

[73] D. M. Winker. "Effect of a finite outer scale on the Zernike decomposition of atmospheric optical turbulence". In: *J. Opt. Soc. Am. A* 8.10 (1991), pp. 1568–1573. DOI: 10.1364/JOSAA.8.001568. URL: http://josaa.osa.org/abstract.cfm?URI=josaa-8-10-1568.

[74] Stefan Van der Walt et al. "the scikit-image contributors. 2014. scikit-image: image processing in Python". In: vol. 2. PeerJ Inc., 2014, e453. URL: https://doi.org/10.7717/peerj.453.

[75] Martino Quintavalla et al. "XSAO: an extremely small adaptive optics module for small-aperture telescopes with multiactuator adaptive lens". In: *Journal of Astronomical Telescopes, Instruments, and Systems* 6, 029004 (Apr. 2020), p. 029004. DOI: 10.1117/1.JATIS.6.2.029004.

[76] M. Quintavalla et al. "Correction of non-common path aberrations in pyramid wavefront sensors to recover the optimal magnitude gain using a deformable lens". In: *Appl. Opt.* 59.17 (2020), pp. 5151–5157. DOI: 10.1364/AO.393499. URL: http://ao.osa.org/abstract.cfm?URI=ao-59-17-5151.

[77] Seyed Ayoob Moosavi et al. "Improvement of coupling efficiency in free-space optical communication with a multi-actuator adaptive lens". In: *Opt. Lett.* 44.3 (2019), pp. 606–609. DOI: 10.1364/OL.44.000606. URL: http://ol.osa.org/abstract.cfm?URI=ol-44-3-606.

[78] Matteo Negro et al. "Fast stabilization of a high-energy ultrafast OPA with adaptive lenses". In: *Scientific Reports* 8, 14317 (Sept. 2018), p. 14317. DOI: 10.1038/s41598-018-32182-y.

[79] Stefano Bonora et al. "Wavefront correction and high-resolution in vivo OCT imaging with an objective integrated multi-actuator adaptive lens". In: *Opt. Express* 23.17 (2015), pp. 21931–21941. DOI: 10.1364/OE.23.021931. URL: http://www.opticsexpress.org/abstract.cfm?URI=oe-23-17-21931.